University of Alberta

Library Release Form

Name of Author: Zhigang Han

Title of Thesis: Correlations between seismic and magnetic susceptibility anisotropy in serpentinized peridotite

Degree: Master of Science in Geophysics

Year this Degree Granted: 2004

Zhigang Han
602 Avadh Bhatia Physics Building
University of Alberta
Edmonton, Alberta
Canada, T6G 2J1
zhan@phys.ualberta.ca

Date: _____

University of Alberta

CORRELATIONS BETWEEN SEISMIC AND MAGNETIC SUSCEPTIBILITY ANISOTROPY IN SERPENTINIZED PERIDOTITE

by

Zhigang Han

A thesis submitted to the Faculty of Graduate Studies and Research in partial fulfillment of the requirements for the degree of **Master of Science in Geophysics**.

Department of Physics

Edmonton, Alberta
Fall 2004

University of Alberta

Faculty of Graduate Studies and Research

The undersigned certify that they have read, and recommend to the Faculty of Graduate Studies and Research for acceptance, a thesis entitled **Correlations between seismic and magnetic susceptibility anisotropy in serpentinized peridotite** submitted by Zhigang Han in partial fulfillment of the requirements for the degree of **Master of Science in Geophysics**.

_____

Dr. D. Schmitt (Co-supervisor)

_____

Dr. V. Kravachinsky (Supervisor)

_____

Dr. R. Luth (Earth and Atmospheric Sciences)

_____

Dr. A. Meldrum (Chair and examiner)

Date: _____

To my parents, my wife Ruth, and my daughter Martha.

Abstract

Rock fabrics deduced from either the anisotropy of magnetic susceptibility or of seismic anisotropy have been widely discussed; on this basis one might expect there to be some correlation between their characteristics. However, whether a general relationship exists between magnetic susceptibility and seismic anisotropy and what its significance might be remains unknown and there remains room for future studies. Pindos and Vourinos ophiolite with its high magnetic susceptibility is a good candidate for comparison between the anisotropy of magnetic susceptibility (AMS) studies and seismic anisotropy. Laboratory measurements on these materials include compressional and shear-wave velocities at confining pressures to 300 MPa, density, velocity anisotropy, and shear-wave splitting, which all generally decrease with increasing degree of serpentinization . Inversely, the Vp/Vs ratio and the Poisson's ratio display a continuous increment with the serpentinization degree. Magnetic fabrics, sensitive indicators of low-intensity strain, were further obtained from AMS measurements on the same samples. The directions of acoustic and magnetic anisotropy compare favorably. A possible reason for this correlation is that the magnetic fabrics are thought to be representative of the secondary magnetite produced during serpentinization and also from the primary paramagnetic minerals assemblage. The bulk magnetic fabric of a few secondary magnetite originated from serpentinization along fractures that crosscut olivine grains might mimic the principal rock texture to some extent. The experimental seismic velocities offer the average calculations of anisotropies, elasticity, and symmetries for the whole mineral assembly of

rocks. Comparing the AMS and seismic anisotropy indicates that generally both directions and intensities of the magnetic susceptibility anisotropy and the seismic anisotropy coincide. These results motivate the development of additional method to use the fabric, as deduced from simple and fast AMS measurements, as a proxy for finding the directions of elastic anisotropy in traditional ultrasonic laboratory methods.

Acknowledgements

First of all, I should express my sincere gratitude to my supervisors, Dr. Douglas R. Schmitt and Dr. Vadim A. Kravchinsky, for their guidance, intelligent advice, and support. Both their mentorship and friendship make my last two years in University of Alberta exciting and enjoyable.

I wish to thank all my committee members for their revision and suggestion for my thesis, which significantly enhanced the quality of the present dissertation. I also want to thank the staff of the physics department for their help, special thanks to Lynn Chandler and Sarah Derr for their hard work for the graduate students in our department.

I also like to extend my appreciations to my friends and follow students in the University of Alberta for their kindness, support, and encourage. Needless to say, I will express my gratitude to M. Welz, J. Havestock, J. Mackinnon, O. Catuneanu, D. Rokosh and D. Caird for their technical assistances. I should specially mention L. Tober. He is very patient and ready to help all the time. He always knows how to solve the unexpected questions in the experiment with his experience and knowledge.

I am grateful to my wife Ruth, who has undertaken many of the family chores during the past few years. She has dedicated her love to our success now and in the future.

Finally, I should sincerely appreciate my parents and brother for all their spiritual encouragement and love, even far away, which always give me courage and confidence during my study in Canada.

Contents

List of Tables

List of Figures

List of symbols

This list includes most symbols for the physical quantities discussed in the text. Suffixes of vector and tensor quantities take the values 1, 2, 3.

P Pressure

T Temperature

σ_{ij} Component of the second order stress tensor

c_{ijkl} Component of the forth-rank elasticity tensor

ε_{ij} Component of the second order strain tensor

$\lambda \ and \ \mu$ Lamé parameter

ρ Mass density

u_i The ith component of the displacement

U_i Amplitude

ν Phase velocity

δ_{ik} Kronecker delta

Γ_{ik} Component of the Kelvin-Christoffel matrix

V_{xx} P-wave velocity along X-axis; Similarly, V_{yy} and V_{zz}

$V_{xy} \ and \ V_{xz}$ Two shear wave velocities propagating along the direction of X-axis and be polarized in the directions of Y- and Z-axis, respectively. Similarly, V_{yx} and V_{yz}; V_{zx} and V_{zy}

V_p P-wave velocity

V_s S-wave velocity

A Velocity anisotropy

$\triangle V_s$ Shear wave splitting

M Induced magnetization

K Magnetic susceptibility

H Inducing magnetic field

χ Mass susceptibility

K_{ij} Component of the second-order magnetic susceptibility tensor

$K_1 \ or \ K_{max}$ Maximum susceptibility axis

$K_2 \ or \ K_{int}$ Intermediate susceptibility axis

$K_3 \ or \ K_{min}$ Minimum susceptibility axis

$P_J \ and \ T$ Jelinek corrected anisotropy degree and shape parameters

$K_m = (K_1 + K_2 + K_3)/3$ The mean magnetic susceptibility

β Serpentine ratio as estimated from density

Chapter 1

Introduction

1.1 Background

The seismic and magnetic properties of rocks are really what their corresponding geophysical surveys remotely sense. Both of these properties, in general, depend on the direction from which they are investigated; that is, there physical properties are generally anisotropic. More specially, the seismic P-wave and S-wave velocities in the earth will change with the angle at which the propagate. Additional complication are caused by birefringent effects. Similarly, induced magnetic field strength will depend on the orientation of the rock with respect to the magnetic field, this will be represented by variations in the magnetic susceptibility with direction.

There are many different factors influencing seismic (or elastic) anisotropy. Similarly, magnetic fabrics are also dependent on the orientation in which the sample is measured in the magnetic field; this means that the magnetic susceptibility is variable with the direction of investigation. The strength of the magnetization induced by a weak field of constant strength depends on the orientation of the sample within the field. This characteristic of rocks is well known in rock fabric measurements.

To interpret seismic data in terms of lithology, laboratory measurements on representative rocks are often employed. To describe the magnetism of the Earth and the magnetic fabric of rocks, knowledge of the magnetic behavior of rocks and their constituent minerals is necessary. In the same manner as seismic anisotropy may be used to analyze and model rock fabrics, the simpler AMS (anisotropy of magnetic susceptibility) measurement allows insight on the microstructure of materials to be gained on the basis of

their magnetic fabric. The anisotropy of low field magnetic susceptibility has also being a useful tool that has been successfully used in rock fabric studies. One might reasonably expect both properties to have been influenced by the rock's history, and, hence, there to be some degree of correlation between the two. Consequently it may be possible to use simple AMS measurements as proxies for elastic wave anisotropy.

Much of our present knowledge on the deep continental crust and the upper mantle was obtained by seismic methods. In the past [see the compilation by *Holbrook et al.* (1992)], most studies of deep crustal composition have assumed the deeper crust to be elastically isotropic. The assumption of isotropy is scale sensitive and valid only in materials with uniformly and randomly oriented minerals, microcracks, and pores. Use of this assumption, simplifies construction of earth models from seismic observation. However, in reality most rocks are elastically anisotropic, this anisotropy is caused by a number of different factors. Generally, seismic anisotropy is due to an ordered arrangement of elements of the rock that are small compared to the wavelengths employed. Conversely, a randomly oriented assembly of crystals is equivalent to an isotropic medium. *Helbig* (1994) listed a few causes for ordering of other elements:

- Magma flow that preferentially orients elongated mineral crystal precipitates;
- Settling in the horizonal plane of ellipsoidal mineral grains with the long axis in a flow regime or of flat clay platelet in still water;
- Compaction under increasing vertical stress during diagenesis that results in further rotation of grain axes into the horizontal plane;
- Formation of families of metamorphic straining that produces oriented cracks and joints;
- Large-scale recrystallization foliation and lineation;
- Preferential opening or closing of compliant cracks and pores by a non-hydrostatic stress state.

As this list suggest, seismic anisotropy could result from combination of the preferential orientation of mineral grains, the presence of orientated cracks of various sizes, or

the occurrence of thin layering. These characteristics are of great interest by themselves as they reveal to use some additional information on the earth's structure. As our observational capabilities improve, seismic anisotropy cannot be neglected in seismic studies of the earth's crust.

It is well known that most rocks in the crust and upper mantle are to some degree anisotropic; Consequently, the questions that naturally arise are related to how to evaluate the potential contribution of anisotropy of these rocks, what is the cause of the anisotropy, and how this anisotropy is related to the rock fabric and the mineral orientation distributions. The seismic anisotropy of metamorphic rocks depended on a variety of factors that includes mineralogical composition, metamorphic grade, the degree of texture development, and the extent of brittle deformation. Much laboratory and theoretical work has already been carried out in recent years towards a better understanding of these problems. Laboratory studies of mantle rock anisotropy have focused on (1) the magnitude and symmetry of velocity anisotropy, (2) the relative orientation between seismic properties and the structural framework, and (3) the $insitu$ structural orientation with constraints from experimental petrology and seismic observations (*Long and Christensen*, 2000).

In the present study emphasis is placed on the intrinsic[1]seismic anisotropy caused by a pronounced fabric of highly anisotropic minerals. Research trends show that both seismic anisotropy and the causative intrinsic petrofabrics are worth trying to quantify in both the laboratory and by numerical methods. Alternatively, the development of magnetic anisotropy is characterized by its various applications and laboratory technique improvement. In this thesis, the P- and S-wave anisotropy of a suite of typical ophiolite samples of the same origin and extending over a wide range of degree of serpentinization have been measured in laboratory. The determination of seismic velocity is first discussed; then, a comparative study of the magnetic anisotropy caused by the rock fabrics and mineral composition is carried out; and finally, the seismic anisotropy, elastic properties, and symmetry based on velocity measurements will be evaluated and compared

[1]The anisotropy caused by the structure of the medium *Helbig* (1994). That is, the anisotropy of the nonporous mineral aggregate in which the anisotropy is due primarily to the elastic properties, cement, and degree of preferential orientation of the constituent minerial grain. This is also often referred to as " lattice preferred orientation" or LPO.

with magnetic fabric by AMS measurements.

1.2 Why elastic anisotropy measurements are important

Over the past decade, technological advances have brought us new capacity to acquire and process large amounts of high-resolution seismic records in both seismic exploration and earthquake teleseismic observation. The physical properties of rocks are to some extent anisotropic as demonstrated by many seismic studies, borehole logs, and laboratory measurements. In fact, anisotropy is likely a fundamental character of rocks. Despite the recognition of this fact, our understanding of the anisotropic properties of many rocks is still limited. However, it is important to understand the intrinsic properties of the rocks through which the seismic waves pass because consideration of anisotropy in seismic analysis and processing will improve the modelling power of such studies.

It is worthwhile to briefly mention for the concept what is meant for by seismic anisotropy. This is, velocities depend on angle. Shear wave splitting (SWS) means that two S-waves travel in the same direction with different polarizations and speeds (Figure 1.1). For olivine say: the maximum single-crystal V_p anisotropy is 21.9 %; the maximum S-wave splitting is about 0.9 Km/s (*Weiss et al.*, 1999).

Anisotropic wave propagation can be induced externally by stress fields or intrinsically by the preferred orientation of minerals, by oriented cracks, or by layering. In seismic studies, we are in particular interested in the causes of anisotropy that are due to the structure od the material itself; here, we refer to the anisotropy caused by the various crystallographic orientations of the non-porous rock as "intrinsic anisotropy". Among the many other interesting properties of natural rocks, anisotropy has become particularly important following the development of seismology exploration and seismic surveys. In fact, studies on the relationship between velocity anisotropy and pressure are considered to be an important component of rock physics studies, particularly for those rock types that primarily are thought to constitute the lithosphere. Anisotropy of P- and S-wave velocity and Shear wave splitting are important characteristics of crustal and mantle rocks.

It is essential that accurate interpretation of seismic velocity images of the lithosphere

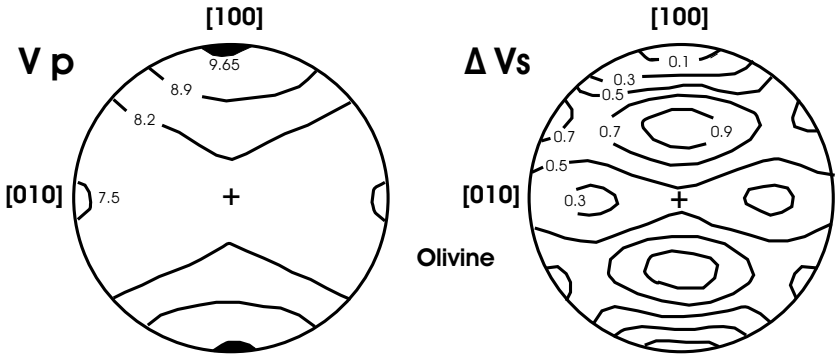

Figure 1.1: P-wave velocity anisotropy and shear wave splitting (km/s) of single crystal olivine. Modified from *Weiss et al.* (1999)

in terms of lithology require a through knowledge of the seismic properties of the different rock types. Since *Christensen* (1965, 1966a) measured the compressional and shear velocities of peridotites and dunites at hydrostatic pressures to 1 GPa (10 kb) and noted a correlation between the degree of serpentinization with decreasing P-wave velocity, laboratory measurement of seismic properties of rocks and minerals in high pressure and temperature have greatly improved. Marine seismic data has detected velocity anisotropy in shales and other sediments (*Banik*, 1984). Vertical seismic profile (i.e. well-bore seismology) data (*Kebaili and Schmitt*, 1996) and cross borehole surveys have been used to detect velocity anisotropy. Velocity anisotropy is also observed in laboratory scale experiments on rock cores. *Horen et al.* (1996) explored this relationships between the degree of serpentinization and P- and S-wave anisotropy again. In their study the magnitudes of the P- and S-wave velocities linearly correlate with the serpentine content as estimated from the mineral density. Much laboratory [*Birch* (1960, 1961), *Nur and Simmons* (1969), *Jones and Nur* (1982, 1984), *Barruol and Kern* (1996), *Horen et al.* (1996), *Kern* (1993); *Kern et al.* (1997)] and theoretical work [*Baker and Carter* (1972), *Siegesmud et al.* (1989), *Mainprice and Silver* (1993), *Ji and Salisbury* (1993a); *Ji et al.* (1993b, 1994)] on shale and metamorphic rocks has been devoted to the nature of P- and S-wave anisotropy in the Earth's crust and upper mantle.

In general, all minerals are anisotropic; textured rocks as aggregates of such minerals must also be anisotropic by this reasoning. In terms of seismic anisotropy, the texture of the grains within a given rock are said to have a preferred crystallographic

or lattice-preferred orientation. In crustal metamorphic rocks, anisotropy is similarly caused by preferred orientation of the constituent crystals. The correlation between seismic anisotropy and preferred mineral orientation is supported by the comparison of seismic reflection data with laboratory measurements on cores taken from the study areas of *Christensen and Salisbury* (1979). It is also important to further understand the relationship between the rock texture and the velocity anisotropy. More specially, the symmetry of the sample's texture will influence the severities and characters of the anisotropy observed. *Bachman* (1979) found in cores from the deep-sea drilling project. *Jones and Nur* (1982) reported laboratory P-wave anisotropy of mylonitic rocks. The seismic anisotropy was controlled by the degree of lattice-preferred orientation of phyllosilicates. *Cholach et al.* (2004) investigated two representative suites of metamorphic rocks from Flin Flon Belt, Saskatchewan. Analysis of the P-wave anisotropy of these samples indicates that studied metamorphic rocks have transversely isotropic or orthorhombic elastic symmetry. The observed seismic anisotropy is directly related to the visible texture.

Anisotropy is also produced by both oriented crack porosity and by deviatoric stress states. *Birch* (1960, 1961) made the measurement of velocities to 10 kb, and suggested that the non-linear increase in velocity at low confining pressure could be attributed to the closure of pores, cracks and micro-fractures. *Nur and Simmons* (1969) found that anisotropy could be created in rocks by subjecting them to non-hydrostatic state as might be found in the earth. Deviatoric stress fields are known to influence the elastic properties of rocks. This fact is important to the interpretation of crustal seismic data and laboratory measurements because stress will influence seismic velocity. This stress dependent anisotropy is primarily produced by orientated microcracks within the rock mass. For example, cracked rocks that are intrinsically isotropic at room temperature will exhibit velocity anisotropy that depends on the elastic properties of the matrix, the porosity, the aspect ratios of the cracks, and the bulk modulus of the pore fluid (*Nur*, 1971; *Anderson et al.*, 1974; *Crampin*, 1978, 1981) when subject to non-hydrostatic stresses. Laboratory measurements of ultrasonic wave velocities in most rock samples demonstrate that velocity increases with confining pressure. At low pressure, this effect is attributed to the progressive closure of microcracks with increasing pressure (*Vernik and Nur*, 1992; *Vernik*, 1993; *Johnston and Christensen*, 1995). The seismic anisotropy rises or decreases with con-

fining pressure at the low-pressure range (less than 300 MPa). The closure of microcracks can either reinforce or attenuate the anisotropy due to lattice-preferred orientation of rock forming minerals (*Ji and Salisbury*, 1993a; *Ji et al.*, 1993b). If the cracks are preferentially aligned, some forms of anisotropy symmetry are produced. Orientated cracks are also important in crustal seismic studies, and it has been suggested these are an indicator of the prevailing stress orientations in the shallow crust. The cracks are aligned in a vertical plane striking parallel to the maximum horizontal stress orientation (*Crampin*, 1978). Crampin showed that if the seismic wavelength is large relative to the typical crack spacing, the cracked medium is transversely isotropic with a horizontal axis of symmetry perpendicular to the plane of the cracks. As a result, it has been suggested that variability of the stress field near active faults can be monitored by changes in anisotropy.

Peridotite is an ultramafic rock made of Mg-rich olivine and lesser amounts of pyroxene, usually both Ca-Mg-rich clinopyroxene and Ca-poor, Mg-rich orthopyroxene. The ubiquitous serpentinization of peridotites on the sea floor is due to interaction with seawater at temperatures that can reach 500 ^{o}C. The provenance of exposed oceanic peridotite is believed to be the upper mantle; serpentinized peridotite found within uplifted fragments of ancient oceanic lithosphere (ophiolite) may represent a metamorphic or igneous protolith (*Gass et al.*, 1984). There have been numerous studies on peridotites due to their importance in the earth. Peridotite are thought to be the major petrologic type in the upper mantle. Surface observation of teleseismic shear wave splitting, in particular, are often interpreted as being produced by textured peridotites. Since the middle of last century, *Hess* (1964) first reported evidence of P-wave velocity anisotropy of the oceanic upper mantle. This azimuthal anisotropy is also observed in the upper mantle from Rayleigh and Love waves. *Hess* (1954) believed these rocks to be of mantle origin and to be related to basalt genesis. *Nicholas and Christensen* (1987) described the main source of the high anisotropy observed in the mantle of the earth. They showed that plastic deformation resulting from simple shear on minerals preferably align the crystals; therefore, mantle flow directly results in seismic anisotropy. *Kern* (1993) showed that macroscopic anisotropy of P- and S-wave velocities is strongly controlled by olivine in serpentinized peridodites and by the serpentine lattice preferred orientation in serpentinite in laboratory seismic measurements. In his work, the rock fabrics were determined with U-stage

measurement on an X-ray texture goniometer. For the interpretation of shear wave splitting, the direction of wave propagation in relation to the LPO of the major minerals and to the symmetry of their lattice fabric is of great importance.

Acoustic-wave anisotropy observed (*Christensen and Landquist*, 1982; *Kern*, 1993; *Horen et al.*, 1996) on peridotite from the upper mantle is consistent with the anisotropy of their dominant minerals (olivine and orthopyroxene) and their statistical orientation distribution. *Dewandel et al.* (2003) compared laboratory measurement and calculation of elastic properties. The results showed that P- and S-wave velocities in Oman serpentinized opiolite are mainly controlled by the mineral orientations. The penetrative serpentine network does not affect directly the geometry of seismic anisotropy, but contributes indirectly in the fact that this network controls the microcrack orientations. The extrapolation of their calculated model also suggests that increasing degree of serpentinization will increase the seismic anisotropy contrary to Horen et al's and measurements to be presented later.

The serpentinization of peridotite profoundly affects its seismic wave velocity, anisotropy, density, and electrical properties. While seismic velocity is roughly proportional to the degree of serpentinization (i.e. the relative volumetric abundance between serpentine, unaltered olivine, and pyroxene), other parameters such as the presence of fractures may also be important. Accurate estimations of the lithology of the oceanic crust are important to obtain constraints on magmatic production along mid-ocean ridges (*White et al.*, 1992), the mechanical properties of the oceanic lithosphere (*Escartín et al.*, 1997, 2001), or the distribution of alteration with depth.

One major difficulty in the interpretation of the nature of the lower crust in these seismic profiles is the similarity in the P-wave velocities between gabbros and partially serpentinized peridotites (*Horen et al.*, 1996). The earlier laboratory seismic measurements on ultramafic rocks are listed in table 1.1. Some differentiation may be possible on the basis of S-wave velocities (*Christensen and Salisbury*, 1979; *Christensen*, 1996). However, there are few seismic profiles that provide well-constrained in situ Vp and Vs data; and even in these cases the data do not allow for an unequivocal discrimination between gabbro and serpentinized peridotite (*Carlson*, 2001).

Table 1.1: Earlier laboratory seismic measurements in ultramafic and mafic rocks

	P wave			S wave			P / T	density	reference
	V_{max}	V_{min}	Anisotropy	V_{max}	V_{min}	Anisotropy	$(MPa/^oC)$	(g/cm^3)	
Rock	[Km/s]	[Km/s]	(%)	[Km/s]	[Km/s]	(%)			
Harzbugite (Bushveld)	7.91	7.7	2.7				200/room	3.37	Birch, 1960
Dunite (Webster N.C.)	7.68	7.49	2.9				200/room	3.24	Birch, 1960
Dunite (Wash.)	8.85	7.92	11.1				200/room	3.31	Birch, 1960
Serpentinite (Theford)	5.88	5.65	4				200/room	2.6	Birch, 1960
Serpentinite (Cal.)	6.12	6.05	1.1				200/room	2.71	Birch, 1960
Serpentinite (Cal.)	5.03	4.56	9.9	2.35	2.21	6.1	200/room	2.52	Christensen, 1966a,b
Peridotite 1 (Cal.)	6.24	5.77	7.8	3.04	2.86	6	200/room	2.75	Christensen, 1966a,b
Peridotite 6 (Cal.)	7.25	7.12	1.8	4.04	3.92	3	200/room	3.14	Christensen, 1966a,b
Peridotite 1 (Hawaii)	7.85	7.45	5.2	4.31	3.91	9.6	200/room	3.29	Christensen, 1966a,b
Dunite (Wash.)	8.96	8.22	8.7	4.83	4.38	9.7	200/room	3.33	Christensen, 1966a,b
Peridotite 475	8.67	8.12	6.3	4.75	4.68	1.3	600/20	3.32	Kern, 1993
(Italy)	8.37	7.84	6.3	4.55	4.51	1.8	600/600	3.27	Kern, 1993
Serpentinite 987	7.92	6.11	26.4	3.86	3.19	18.5	600/20	2.74	Kern, 1993
(unknown)	7.92	5.84	29.3	3.71	3.03	19.6	600/500	2.72	Kern, 1993
PS4	5.86 (ave.)		1	3.08 (ave.)		2	atm./room	2.71	Horen et al., 1996
PS1	6.79 (ave.)		2	3.58 (ave.)		4	atm./room	3.06	Horen et al., 1996
PF2	7.35 (ave.)		2	4.17 (ave.)		6	atm./room	3.2	Horen et al., 1996
PF1	7.76 (ave.)		6	4.35 (ave.)		5	atm./room	3.26	Horen et al., 1996
Ophiolite(Tibet)									
$Cube\,\pi$	6.6	6.3	4.7	3.5	3.3	5.9	600/room	3.29	Dewandel et al., 2003
$Cube\,\sigma$	6.6	6.2	6.2	3.5	3.1	12	600/room	3.29	Dewandel et al., 2003
(Oman ophiolite)									
90VS53b	7.08 (ave.)		2.7	4 (ave.)		3.25	200/room	3.24	Barruol, 1993
(Ivrea gabbro)									

1.3 Causes of magnetic anisotropy

The origin of magnetism lies in the orbital and spin motions of electrons and their mutual interactions with one another. Different types of magnetism characterize the responses of the different materials to magnetic fields. Generally speaking, all materials are to some degree magnetic, however, some materials are significantly more magnetic than others. The main distinction is that in some materials there is no collective interaction of atomic magnetic moments, whereas in other materials there is a very strong interaction between atomic moments. There are three kinds of magnetic minerals in rocks, that is, ferrimagnetic (usually in accessory phase), paramagnetic, and diamagnetic minerals. Most igneous and metamorphic minerals are paramagnetic; in very weakly magnetic rocks, dia-

magnetism can dominate the magnetic properties (*Owens and Rutter*, 1978; *Hrouda*, 1986). All mineral grains within a rock contribute to its total susceptibility, but their individual influence depends on their intrinsic susceptibility as well as on their concentration. On the basis of the relationship between mineral concentration and the susceptibility of rock, while paramagnetic minerals is as common constituents (10%) , *Tarling and Hrouda* (1993) suggested that:

- the susceptibility and magnetic anisotropy carrier of rock are primarily the ferrimagnetic fraction, if its susceptibility greater than 5×10^{-3} (SI);
- the susceptibility and magnetic anisotropy carrier of rock are primarily the paramagnetic fraction, if its susceptibility less than 5×10^{-4} (SI);
- the susceptibility and magnetic anisotropy carrier of rock are both the paramagnetic and the ferrimagnetic, if a mean susceptibility in the range of 5×10^{-4} to 5×10^{-3} (SI);

Magnetic susceptibility K is defined by $M = K \times H$, where M is the induced magnetization of the material and H is the inducing magnetic field. As both M and H are expressed in amperes per meter, the volumetric magnetic susceptibility K is dimensionless (SI) while mass susceptibility $\chi = K/\rho$ is in cubic meters per kilogram. Susceptibility varies in the general case according to the strength of the H field and temperature. It may also vary with the measurement direction resulting in a non-parallelism between H and M vectors. For a single particle the influence of the crystal structure and the shape of the grains on the direction of magnetization produce magnetic anisotropy; for multi-domain-sized particles, domain theory plays another important role. Magnetic anisotropy strongly affects the shape of hysteresis loops and controls the coercivity and remanence (*Tarling and Hrouda*, 1993).

As mentioned earlier, magnetic properties arise from the motion of electrically charged particles at the atomic scale. Thus, an electron has a magnetization that is associated with its axial spin and also one due to its orbital motion around a nucleus. That means all materials have magnetic properties at temperatures above absolute zero (0^o K). The idea that the anisotropy of the magnetic susceptibility (AMS) can be used as a gauge of petrofabric is similar to that for elastic anisotropy: rocks will have magnetic fabric due to the

preferential orientation of anisotropic magnetic minerals. In most rock forming minerals, the preferred orientation of their crystallographic axes and the grain shape determine the magnitude and direction of the AMS. The bulk susceptibility and its anisotropy represent a summation of the susceptibility of all the mineral species present in a sample.

The directional variability in magnetization is termed magnetic anisotropy. The magnetic anisotropy of rocks was first probably revealed by *Ising* (1942). Magnetic anisotropy can also be expressed in terms of the directional variability in the energy of magnetization to saturation (*Stacey*, 1960). In the study of rock fabrics, low field[2] magnetic susceptibility anisotropy may be described using an oriented ellipsoid (K_{max}, K_{int}, and K_{min} or K_1, K_2, and K_3). The magnetic anisotropy has been used for this field successfully over last decades (*Girdler*, 1961; *Jelinek*, 1978; *Hrouda*, 1982; *Rochette et al.*, 1992; *Borradaile and Henry*, 1997; *Borradaile*, 2001) (Figure 1.2). The study of the rock anisotropy is one of the more promising subjects in rock magnetism research because it is linked to the rock's intrinsic petrofabric. In general, magnetic fabrics are sensitive indicators of rock texture and strain. Magnetic fabric techniques use this characteristic to measure the petrofabric of rocks in order to provide additional information on the rock's origin and structural evolution. The anisotropy of magnetic anisotropy depends on the anisotropy of grain particles themselves and on their degree of alignment. Many authors have reviewed the principles and applications related to anisotropy of low field magnetic susceptibility (*Hrouda*, 1982; *Borradaile*, 1988; *Jackson*, 1991; *Tarling and Hrouda*, 1993; *Borradaile and Henry*, 1997).

1.4 Objective of the work

Determination of the lithological, magnetic and seismic properties of crustal and mantle rocks is essential for proper interpretation of the nature of observed seismic reflectors or of velocity studies, and of magnetic phenomena. Seismic velocity and anisotropy modeling based on single crystal values or the constituent minerals can be compared with laboratory measurements later, which offer another approach to assess the anisotropic properties of rocks; similarly, magnetic fabric from AMS measurement could be com-

[2]Usually, inducing magnetic field less than 1 mT.

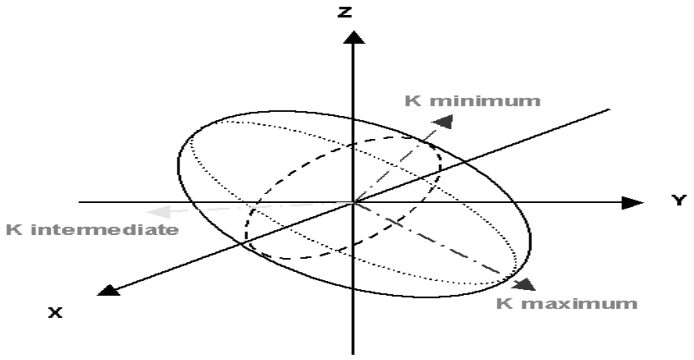

Figure 1.2: Schematic showing the magnetic susceptibility ellipsoid of rocks. (K min, K int, and K max correspond to the minimum, intermediate, and maximum principal axes of the ellipsoid)

pared with AMS computation by considering their crystal properties and volume fraction in future work.

Despite this ubiquitous characteristic of rock, few studies have examined the relationship between seismic and magnetic anisotropy. Various authors have investigated and focused their research on the relationship between mineralogical and magnetic fabrics. However, few studies deal with the related problem of the relationship between the anisotropy of magnetic susceptibility and seismic anisotropy, despite numerous observations that petrofabric is closely related to both micro-crack and lattice-preferred orientation (LPO) which are often the dominant sources of seismic anisotropy. It is reasonable to suggest that the LPO and assembly of minerals similarly will influence the magnetic fabrics and the AMS. The second motivation for this study is to assess to what degree elastic and magnetic anisotropies are related in serpentinized peridotites. A relationship between these two would allow the simple AMS measurement to be used as a proxy for rock fabrics in seismic anisotropy studies. In later work, we aim to determine other systematic magnetic fabric changes in various anisotropic media and construct a database

of experimental data for numerical modeling. The metamorphic rocks with complex texture and composition usually exhibit a particularly seismic and magnetic anisotropy. With a suite of rocks of the same origin, and extending over a wide range of degree of serpentinization, our investigation may yield interesting comparisons.

The approach used in this study to derive anisotropic rock properties comprises of two complementary methods applied to the same samples: (1) ultrasonic velocity laboratory measurements and, (2) anisotropy of magnetic susceptibility laboratory measurements. Both procedures and results will be described, compared and discussed for a group of serpertinized dunite and harzburgite samples from the Pindos and the Vourinos Ophiolite in Greece (Figure 1.3).

1.5 Geological background

Ophiolites are considered to be masses of oceanic crust and upper mantle rocks, where there is a distinctive sequence of magmatic, sedimentary, and metamorphic rocks formed in an oceanic environment (*Best*, 2003). In this study, we select a suite of samples from the Pindos and the Vourinos ophiolite (Greece), with densities ranging from 2.6 to 3.28 g/cm^3, corresponding to degrees of serpentinization of 2.3 % to 87.9 % (estimated by linear relation between density and serpentinization, *Christensen* (1966b)). These rocks represent, to our knowledge, one of the most complete suites of peridotites with systematic variations in the degree of serpentinization available. We have primarily selected dunite samples, whose main mineral phases are therefore olivine and its derivative product serpentine, with minor accessory minerals such as magnetite and other oxides. In the weakly altered dunites, serpentine tends to form primarily along fractures that crosscut olivine grains, and therefore displays a serpentine net distribution (see thin sections in Appendix). This may mimic the principal rock texture to some extent. With an increasing degree of serpentinization, the alteration is more homogeneously distributed following cracks that break up individual olivine grains.

The Pindos and Vourinos ophiolites are part of the Dinaric-Hellenic ophiolite belt outcropping along the Northeastern Mediterranean (Figure 1.3(a)). These ophiolites formed during the Middle Jurassic (*Smith*, 1993). They were emplaced shortly after their forma-

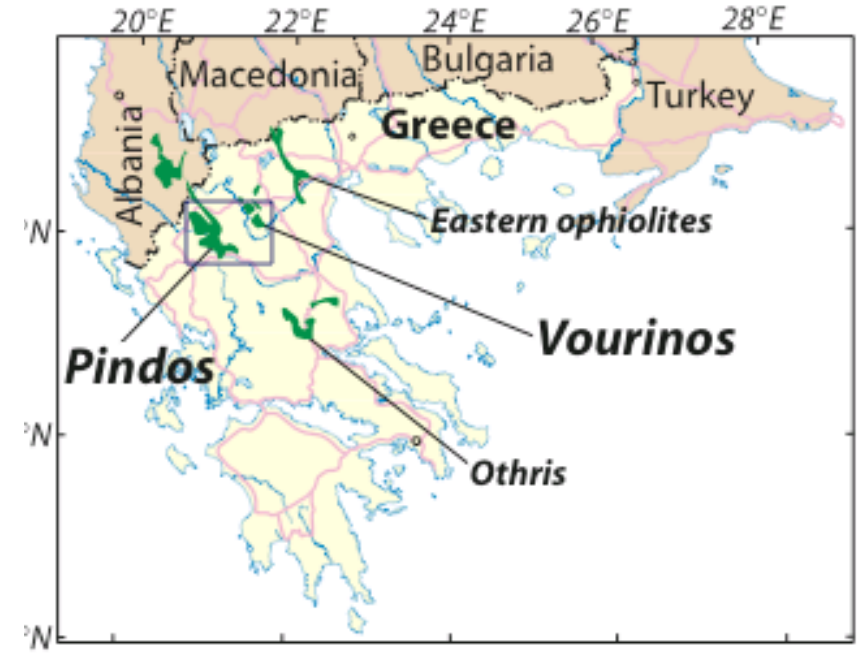

(a)

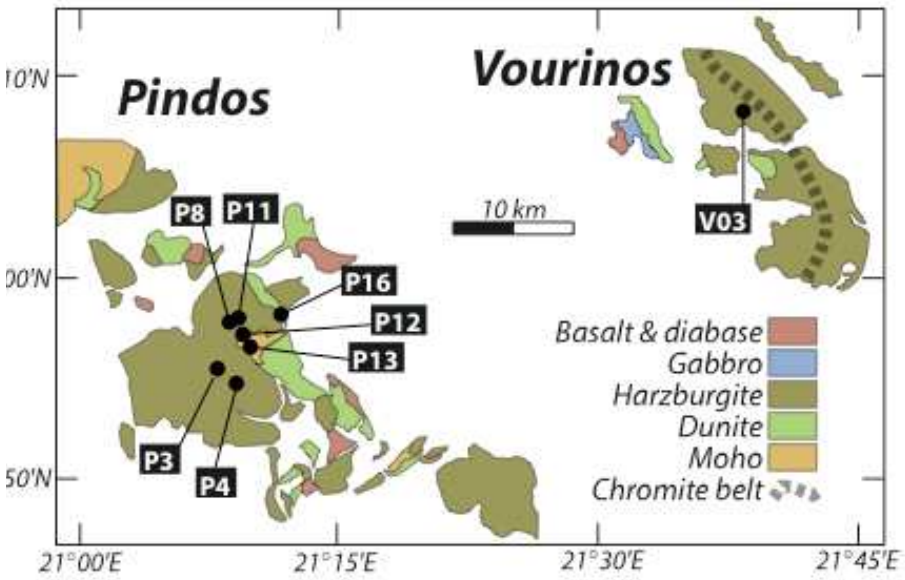

(b)

Figure 1.3: Top: Sample location map in Greece. Bottom: Lithological distribution map of Pindos and Vourinos ophiolites (after Rassios et al., 2000; by courtesy of J.Escartin).

Table 1.2: The sampling location of Pindos and Vourinos ophiolites

$Sample$	$Latitude(^oN)$	$Longitude(^oE)$	$Site$
P03	39.9243	21.1328	Valia Kaldia
P04	39.9123	21.1517	Bottom Valia Kaldia
P08	39.9633	21.146	Loumnitsa Valley
P11	39.9667	21.1532	Loumnitsa Valley
P12	39.9531	21.1573	Top of Dramala
P13	39.9427	21.1645	
P16	39.9696	21.194	
V03	40.1555	21.6655	Voidolokkos, N Varis ($\sim$4 km)

tion and dismembered both during their obduction and by later tectonism (*Rassios*, 2000). The Vourinos ophiolites are composed primarily of harzburgite and associated dunite [3], which are locally deformed. The Vourinos ophiolite shows the most complete stratigraphy ($\sim$12 km in thickness, with $\sim$5 km of crust), including peridotite, gabbro, and a well-developed dykes section. The Pindos ophiolite is less compete and more tectonized, with a basal layer of harzburgite mylonites ($\sim$200 m), and less deformed harzburgite and dunite bodies above it, and small outcrops of dyke and basalt (*Rassios et al.*, 1983). Rock blocks used in this study were selected from samples obtained during a fieldwork season in 2000 by Escartín and Mével. The sampling locations are in table 1.2. Dr. Escartín will use the samples in later deformation experiments.

Figure 1.3(a) shows selected ophiolites from the Hellenic Arc in Greece and Albania (green areas). Figure 1.3(b) is the map of the Pindos and Vourinos ophiolites (*Rassios*, 2000). The Vourinos ophiolite shows a continuous stratigraphy, while tectonicsm is more prominent in the Pindos ophiolite, where contacts are mostly tectonics (thrust faults). The Meso-Hellenic Trough developed in the Cenozoic has separated these ophiolites. Location of sampling sites are indicated by black dots and corresponding labels.

[3] harzburgite composed of orthopyroxene, 40-90% olivine and $<$10% clinopyroxene; dunite containing olivine and pyroxenes, $>$90% olivine.

Chapter 2

Elastic-wave velocity and anisotropy

2.1 Introduction

The intrinsic elastic rock properties are important information in seismic interpretation and modeling. They provide indication of the underlying symmetry; and here texture of the rock. As well, the elastic constants control the degree of anisotropy of the rocks which can be on the order of 10 % or more. Velocity anisotropy is essentially related to the elastic properties of materials. However, despite this importance there have been remarkably few measurements of rock velocity anisotropy or determinations of the elastic constants carried out on rocks. The important goal here of the laboratory experiments is anisotropy determination and estimation of the rock's complex elastic behavior. In principal the stiffness tensor can be determined directly by applying normal and shear stress to the sample and observing the strains produced. However, it is often simpler to determine those same properties indirectly by measuring the elastic wave velocities and densities of the material. Based on accurate laboratory measurements, it is possible to calculate the elastic constants.

Ideally, a seismic experiment would reveal to us both geologic structure and lithology. The latter can be in part provided from knowledge of the $in\ situ$ material properties. In order to obtain these physical properties from the seismic measurements, it is imperative to understand how the elastic properties of rocks can be affected by their mineralogy, content, structure, saturation, stress, and texture. It is equally important to know how seismic responses at $\sim$100 Hz can be correlated with laboratory measurements at 10^6 Hz, considering the large gap between the two in terms of frequency and scale.

There have been many previous attempts at determining the anisotropy of various materials; and the use of ultrasonic methods of measuring compressional and shear elastic wave velocities has been the preferred method employed. In early studies of anisotropy, many of the materials investigated were of simple structure (e.g. highly symmetric cubic or hexagonal) with a simple elasticity requiring only a few measurements. One of the earlier attempts at determining the anisotropy of a material was by *Markham* (1957) who determined the elastic constants of various metals of cubic and hexagonal crystal symmetry through the use of the pulse transmission method. Simply, in the pulse transmission method the travel time of a disturbance transmitted through a known thickness of the sample is measured in order to provide the velocity. In an early study on rock, *Kaarsberg* (1959) found that the velocities both parallel and perpendicular to the bedding increasing with density in shale. The use of elastic wave velocity to determine velocity anisotropy and elastic coefficients has been popular in the laboratory experiment for the last decades (*Pros and Babuska*, 1967; *Van Buskirk et al.*, 1986; *Cheadle et al.*, 1991; *Johnston and Christensen*, 1995; *Mah and Schmitt*, 2001, 2003; *Cholach et al.*, 2004). *Johnston and Christensen* (1995) used the pulse transmission technique to cores of shale being taken at various angles to the axis of symmetry. The phenomenon of shear wave splitting was observed and phase velocities were measured. Through the use of phase velocity measurements, the elastic constants of the rocks were determined. Similarly, *Vernik and Nur* (1992) and *Hornby* (1996) measured P-wave and S-wave velocities of cores cut parallel, perpendicular, and 45 degrees to the bedding surface and determined the elastic constants of rock at pressure. The relationships between elasticity and anisotropy allow for the determination of the elastic properties from the measured velocities and densities. The methods of experimental determination of the elastic coefficients of anisotropic materials were reviewed extensively by *Mah and Schmitt* (2001, 2003).

Many authors have provided theoretical reviews of elastic wave propagation in various mediums; some of the better-known references include *Auld* (1990) and *Musgrave* (1970). Here, we only give a general description that begins and builds from isotropy. In an isotropic medium the P-wave and S-wave particle motions are purely longitudinal and transverse, respectively, to the direction that the wave propagates. In this ideal case, the P- and the S-wave velocities are not dependent on direction. The S-wave polarization

(i.e. direction of particle motion) can be in any direction normal to the wave propagation direction; and consequently, no shear splitting is allowed.

In reality, the mineral crystals usually have a degree of symmetry. Common crystal symmetry system includes cubic, hexagonal, orthorhombic, monoclinic, and triclinic symmetry, which are all anisotropic medium. In optical mineralogy, the rock-forming materials of these systems are optically anisotropic. That is, the velocity of light is different in different directions in these materials. The different systems can be separated in terms of axes, planes, or a center of symmetry. In seismic study, once a material is anisotropic, however, the waves through these materials are referred to as "quasi-P" waves or "quasi-S" waves, because of additional complications with regards to the relationships between directions of the polarization and wave propagation. Two distinct shear waves will, generally, propagate in nearly all propagation directions. The polarizations of these two shear waves will cause differences in their time of arrival. This birefringent phenomenon is commonly known in the geophysical community as shear wave splitting (SWS).

For the rocks in the deeper crust and upper mantle, the high-pressure velocity anisotropy and shear-wave splitting are thought to be caused by the LPO of minerals (*Kern*, 1993). At lower pressure, the alignment of microcracks can also contribute to the anisotropy. At greater confining pressure these cracks close (*Birch*, 1960, 1961; *Christensen*, 1965, 1966a; *Ji and Salisbury*, 1993a; *Ji et al.*, 1993b), the bulk of these cracks often close at pressure below 100 MPa.

In this chapter, I will first give a simple review of elasticity theory and its linkages to velocities; and then, a detailed study is presented on the ultrasonic properties of the serpentine samples. I will show laboratory measurements on samples from the Pindos and the Vourinos opholites (Greece) to see how the serpentinization affects seismic velocity and anisotropy.

2.2 Brief review of elasticity theory

The fundamental relationships between elasticity and anisotropy have been comprehensively described by *Fedorov* (1968); *Musgrave* (1970); *Auld* (1990). The following is only a

Table 2.1: The cyclical recipe for transformation from full to Voigt notation

indice	ij, kl	11	22	33	23 or 32	31 or 13	12 or 21
indice	m, n	1	2	3	4	5	6

brief summary. The main purpose of this section is to highlight the difference between P- and S-wave velocities and the material's elastic properties. The quantitative measurement of such velocities and density consequently yield the elastic properties directly. The characteristics of elastic wave velocities including anisotropies revealed a large amount of intrinsic information of rocks, which imply that the anisotropies of wave velocities are closely related to rock composition, texture, and lattice-preferred orientation. The knowledge of the elastic properties are perhaps more useful than the velocities in that they directly reveal the material's symmetry and texture.

For an anisotropic medium, the generalized Hooke's law completely describes the stress-strain relationship, where the Einstein summation convention[1] will be used in (Eq.2.1):

$$\sigma_{ij} = c_{ijkl}\varepsilon_{kl} \tag{2.1}$$

Where σ_{ij} and ε_{kl} are the second order stress and strain tensors, respectively (*Musgrave*, 1970); c_{ijkl} is the forth rank elasticity tensor whose components are the elastic stiffnesses which we take here to be constants.

The elasticity tensor c_{ijkl} fully describes the elastic properties of anisotropic crystals or solids. Since the elasticity tensor c_{ijkl} has 4 indices, each of which goes from 1 to 3, the elasticity tensor has $3^4 = 81$ elements. The symmetries in the stress and strain tensors reduces the 81 elements of the components of stiffness c_{ijkl} to only 36 independent elements. Then, consideration of thermodynamics principles that the internal energy of a material can only increase during a compression further reduces c_{ijkl} from 36 to 21 independent elastic stiffnesses (*Musgrave*, 1970).

The symmetry of the tensor of elasticity allowed Voigt to introduce a simpler matrix notation (*Nye*, 1957) that is commonly used in the geophysical literature where the four indices $ijkl$ maybe replaced by two indices mn. The stiffness tensor for the sake of con-

[1]Einstein summation convention is a way of dealing with tensors in a compact and consistent way. The idea here is to use indices to describe a generic element and apply tensor algebra.

venience is written as a second-order symmetric Voigt matrix (*Nye*, 1957; *Musgrave*, 1970; *Thomsen*, 1986; *Winterstein*, 1990) in (Eq.2.2):

$$c_{ijkl} = C_{mn}(i, j, k, l = 1, 2, 3; m, n = 1, ..., 6) \tag{2.2}$$

According to the rule (*Vestrum*, 1994), the stiffness tensor c_{ijkl} can be transformed to C_{mn} in Eq.2.2:

$$m = \begin{cases} i, & \text{if i=j ;} \\ 9 - (i + j), & \text{if i}\neq\text{j .} \end{cases} \tag{2.3}$$

$$n = \begin{cases} k, & \text{if k=l ;} \\ 9 - (k + l), & \text{if k}\neq\text{l .} \end{cases} \tag{2.4}$$

Or, according to the cyclical recipe (table2.1):

This allows the generalized Hooke's Law to be simplified from Eq.2.1 to a simple matrix and vector equation:

$$\sigma_m = C_{mn}\varepsilon_n \tag{2.5}$$

Where σ_m and ε_n are 6×1 vectors containing the six independent components of the stress and the strain tensors, respectively. The stiffness tensor c_{ijkl} can be represented as a symmetric 6×6 matrix C_{mn} with 21 independent components.

For example, C_{1133} become C_{13} and C_{1323} or C_{1332} become C_{54}. Explicitly, this may be written:

$$\begin{pmatrix} \sigma_1 \\ \sigma_2 \\ \sigma_3 \\ \sigma_4 \\ \sigma_5 \\ \sigma_6 \end{pmatrix} = \begin{pmatrix} C_{11} & C_{12} & C_{13} & C_{14} & C_{15} & C_{16} \\ C_{21} & C_{22} & C_{23} & C_{24} & C_{25} & C_{26} \\ C_{31} & C_{32} & C_{33} & C_{34} & C_{35} & C_{36} \\ C_{41} & C_{42} & C_{43} & C_{44} & C_{45} & C_{46} \\ C_{51} & C_{52} & C_{53} & C_{54} & C_{55} & C_{56} \\ C_{61} & C_{62} & C_{63} & C_{64} & C_{65} & C_{66} \end{pmatrix} \begin{pmatrix} \varepsilon_1 \\ \varepsilon_2 \\ \varepsilon_3 \\ \varepsilon_4 \\ \varepsilon_5 \\ \varepsilon_6 \end{pmatrix} \tag{2.6}$$

Further, $\varepsilon_4 = 2\varepsilon_{23}, \varepsilon_5 = 2\varepsilon_{13}, \varepsilon_6 = 2\varepsilon_{12}$. Each C_{mn} is one of the components of a 6×6 symmetric matrix that can only have 21 independent stiffnesses. However, this is the

most general triclinic case in which there is no symmetry. It is useful to examine briefly how the elastic tensor C_{mn} appears with increasing symmetry.

Those components below the diagonal are same, because the matrix in Eg.2.6 is symmetric about the diagonal. The number of independent elastic constants depends on the elastic symmetry of the medium. The number of independent elastic constants required with the different symmetries is given in table 2.2.

We need two independent constants (λ and μ) for isotropic symmetry (Eq.2.7). Explicitly in an isotropic medium the coefficients will be $C_{11} = C_{22} = C_{33} = \lambda + 2\mu$, $C_{44} = C_{55} = C_{66} = \mu$, and $C_{12} = C_{21} = C_{13} = C_{31} = C_{23} = C_{32} = \lambda$:

$$[C] = \begin{pmatrix} \lambda+2\mu & \lambda & \lambda & 0 & 0 & 0 \\ \lambda & \lambda+2\mu & \lambda & 0 & 0 & 0 \\ \lambda & \lambda & \lambda+2\mu & 0 & 0 & 0 \\ 0 & 0 & 0 & \mu & 0 & 0 \\ 0 & 0 & 0 & 0 & \mu & 0 \\ 0 & 0 & 0 & 0 & 0 & \mu \end{pmatrix} \tag{2.7}$$

In a cubic medium the coefficients (Eq.2.8) will be $C_{11} = C_{22} = C_{33}$, $C_{44} = C_{55} = C_{66}$, and $C_{12} = C_{21} = C_{13} = C_{31} = C_{23} = C_{32}$. Although the cubic matrix looks very similar to the isotropic one, materials of cubic symmetry require 3 completely independent constants (*Musgrave*, 1970). It is worth noting that while a cubic solid, such as halite, will be optically isotropic; it is elastically anisotropic and halite crystal will have different

Table 2.2: Symmetries and the number of elastic constants required

$Elasticstiffness$	$Isotropic$	$Cubic$	$Hexagonal$	$Orthorhombic$	$Monoclinic$	$Triclinic$
C_{11}	$\lambda+2\mu$	C_{11}	C_{11}	C_{11}	C_{11}	C_{11}
C_{22}	$\lambda+2\mu$	$Same\,as\,C_{11}$	$Same\,as\,C_{11}$	C_{22}	C_{22}	C_{22}
C_{33}	$\lambda+2\mu$	$Same\,as\,C_{11}$	C_{33}	C_{33}	C_{33}	C_{33}
C_{44}	μ	C_{44}	C_{44}	C_{44}	C_{44}	C_{44}
C_{55}	μ	$Same\,as\,C_{44}$	$Same\,as\,C_{44}$	C_{55}	C_{55}	C_{55}
C_{66}	μ	$Same\,as\,C_{44}$	C_{66}	C_{66}	C_{66}	C_{66}
C_{12}	λ	C_{12}	$C_{11}-2C_{66}$	C_{12}	C_{12}	C_{12}
C_{13}	λ	$Same\,as\,C_{12}$	C_{13}	C_{13}	C_{13}	C_{13}
C_{23}	λ	$Same\,as\,C_{12}$	$Same\,as\,C_{13}$	C_{23}	C_{23}	C_{23}
C_{14}	0	0	0	0	0	C_{14}
C_{15}	0	0	0	0	C_{15}	C_{15}
C_{16}	0	0	0	0	0	C_{16}
C_{24}	0	0	0	0	0	C_{24}
C_{25}	0	0	0	0	C_{25}	C_{25}
C_{26}	0	0	0	0	0	C_{26}
C_{34}	0	0	0	0	0	C_{34}
C_{35}	0	0	0	0	C_{35}	C_{35}
C_{36}	0	0	0	0	0	C_{36}
C_{45}	0	0	0	0	0	C_{45}
C_{46}	0	0	0	0	C_{46}	C_{46}
C_{56}	0	0	0	0	0	C_{56}

velocities in different directions.

$$[C]=\begin{pmatrix} a & b & b & 0 & 0 & 0 \\ b & a & b & 0 & 0 & 0 \\ b & b & a & 0 & 0 & 0 \\ 0 & 0 & 0 & c & 0 & 0 \\ 0 & 0 & 0 & 0 & c & 0 \\ 0 & 0 & 0 & 0 & 0 & c \end{pmatrix} \tag{2.8}$$

In the hexagonal (TI) medium (Eq.2.9, $x=(a-b)/2$) the independent elastic coefficients will be $C_{11}=C_{22}$, C_{33}, $C_{44}=C_{55}$, $C_{66}=(C_{11}-C_{12})/2$, $C_{13}=C_{31}=C_{23}=C_{32}$.

For this case, 5 independent constants are required (*Musgrave*, 1970).

$$[C] = \begin{pmatrix} a & b & c & 0 & 0 & 0 \\ b & a & c & 0 & 0 & 0 \\ c & c & d & 0 & 0 & 0 \\ 0 & 0 & 0 & e & 0 & 0 \\ 0 & 0 & 0 & 0 & e & 0 \\ 0 & 0 & 0 & 0 & 0 & x \end{pmatrix} \tag{2.9}$$

In the orthorhombic medium (Eq.2.10) all nine elastic coefficients are independent. The 3 mutually orthogonal planes of symmetry and 9 independent non-zero elastic constants characterize orthorhombic symmetry (*Musgrave*, 1970). This form is general for all the space groups with orthorhombic symmetry.

$$[C] = \begin{pmatrix} a & b & c & 0 & 0 & 0 \\ b & d & e & 0 & 0 & 0 \\ c & e & f & 0 & 0 & 0 \\ 0 & 0 & 0 & g & 0 & 0 \\ 0 & 0 & 0 & 0 & h & 0 \\ 0 & 0 & 0 & 0 & 0 & i \end{pmatrix} \tag{2.10}$$

The number of elastic constants required for some of other forms of symmetry are also listed in table 2.2. However, the cases of the greatest relevance to rocks when using such a texture and consideration will include isotropic, hexagonal (TI), and orthorhombic. Isotropy would be represented of a rock in which all the structural features were randomly oriented. A TI symmetry is often found in layered sedimentary rocks. Finally, orthorhombic symmetry can be generated by the mineralogic orientation in a foliated and lineated metamorphic rocks. One can envisage rock of even lower symmetry by introducing families of oriented microcrocks into a rock mess that is intrinsically orthorhombic.

Table 2.3: Elastic stiffnesses of minerals at room P / T

	$C_{ij}(GPa)$													
Mineral	C_{11}	C_{22}	C_{33}	C_{44}	C_{55}	C_{66}	C_{12}	C_{13}	C_{14}	C_{23}	C_{15}	C_{25}	C_{35}	C_{46}
Forsterite	328	200	235	66.7	81.3	80.9	69	69	0	73	0	0	0	0
Enstatite	225	178	214	77.6	75.9	81.6	72.4	54.1	0	52.7	0	0	0	0
Augite	182	151	218	69.7	51.1	55.8	73.4	72.4	0	33.9	19.9	16.6	24.6	4.3
Hornblende	116	160	192	57.4	31.8	36.8	44.9	61.4	0	65.5	4.3	-2.5	10	-6.2
Brucite	157	157	46.3	21.7	21.7	56.3	44.4	12	0.2	12	-	-	0	-
Lizardite	-	-	-	-	-	-	-	-	-	-	-	-	-	-
Clinochlore	-	-	-	-	-	-	-	-	-	-	-	-	-	-
Clinochrysotile	-	-	-	-	-	-	-	-	-	-	-	-	-	-
Magnetite	275	275	275	95.5	95.5	95.5	104	104	0	104	0	0	0	0

Again, in contrast to the previous cases, if no symmetry is present the material is treated as triclinic (Eq.2.11) which is characterized by 21 independent elastic constants (*Musgrave*, 1970):

$$[C] = \begin{pmatrix} a & b & c & d & e & f \\ b & g & h & i & j & k \\ c & h & l & m & n & o \\ d & i & m & p & q & r \\ e & j & n & q & s & t \\ f & k & o & r & t & u \end{pmatrix} \tag{2.11}$$

The single-crystal elastic stiffness, chemical formula and density of the minerals related to this study are listed in table 2.3 and 2.4 (*Bass*, 1995; *Nickel and Nichols*, 1991). We can compare our laboratory and calculated results with these published results. Unfortunately, there is no information available on the serpentine minerals to our knowledge.

2.3 Relationship between anisotropic velocities and elastic stiffness

We do not observe directly the elastic moduli, they must be indirectly determined either by static stress-strain test or by measuring the material velocities in different direction through the material. In this section, we provide an overview of the mathematical basis

Table 2.4: Density, symmetry, and chemical formula of minerals

Mineral	Symmetry	Formula	Density (Mg/m^3)
Forsterite	Ortho.	Mg_2SiO_4	3.221
Enstatite	Ortho.	$(Mg,Fe)SiO_3$	3.198
Augite	Mono.	$(Ca,Mg,Fe)_2(Si,Al)_2O_6$	3.32
Hornblende	Mono.	$Ca_2(Mg,Fe,Al)_5(Si,Al)_8O_{22}(OH)_2$	3.12
Brucite	Rhombo.	$Mg(OH)_2$	2.38
Lizardite	Hexa.	$Mg_3Si_2O_5(OH)_4$	2.5
Clinochlore	Tri.	$(Mg,Al)_6(Si,Al)_4O_{10}(OH)_8$	2.7
Clinochrysotile	Mono.	$Mg_3Si_2O_5(OH)_4$	2.55
Magnetite	Cubic	Fe_3O_4	5.206

for connecting observed velocities and densities to elastic moduli. The section ends with the simple relationships between the elastic moduli and velocities measured during the symmetry axes of an orthorhombic material as one example.

The equations of motion in terms of the components of the displacement u_i using Einstein's indexing notation may be written as (*Helbig*, 1994):

$$\rho\ddot{u}_i = \sigma_{ij,j} = c_{ijkl}\varepsilon_{kl,j} = c_{ijkl}u_{k,lj} \tag{2.12}$$

Where ρ is the mass density, u_i is the ith component of the displacement, and subscripts after the coma indicate differentiation with respect to the corresponding direction. The wave equation (2.12) establishes a relation between the second temporal derivative of a displacement function u and its second spatial derivatives. With the assumption of the plane wave, the wave equation in anisotropic medium can be written:

$$(c_{ijkl}\beta_l\beta_j - \delta_{ik}\rho\nu^2)\alpha_k = 0 \tag{2.13}$$

Here β_i is a unit vector in the direction of the wave normal, ν is the phase velocity of an elastic wave propagating in the direction of β_i, δ_{ik} is the Kronecker delta. Elastic wave velocities can be calculated from the well-known elastic constants by solving this so-called Christoffel Equation (e.g. *Musgrave*, 1970). Under the plane wave assumption, these phase velocities (i.e. one quasi-P and 2 quasi-S velocities) can be obtained by solving the characteristic equation (2.13) which is:

$$det(c_{ijkl}\beta_l\beta_j - \delta_{ik}\rho\nu^2) = 0 \tag{2.14}$$

Equation (2.14) is commonly given in the form of Christoffel's characteristic equation:

$$det(\Gamma_{ik} - \delta_{ik}\rho\nu^2) = 0 \tag{2.15}$$

The matrix Γ_{ik} is called the "Kelvin-Christoffel matrix" .

$$c_{ijkl}\beta_l\beta_j = \Gamma_{ik} \tag{2.16}$$

An eigenvalue solution of equation (2.15) for any slowness direction n yields three positive values of the squared phase velocity ν^2, which correspond to the speeds of the P-wave and two S-waves. The corresponding eigenvalues of this solution are the three polarization directions available. Determination of the elastic stiffness from the ultrasonic phase velocity measurement has been discussed and reviewed by previous authors (*Cheadle et al.*, 1991; *Mah*, 1999; *Mah and Schmitt*, 2003; *Cholach et al.*, 2004).

The phase velocities are associated with the propagation of a hypothetical plane wave. Generating plane waves in the real world is impossible, although at a suitable distance from a seismic source the plane wave approximation is acceptable. Quite often, velocities are only measured in direction parallel to the symmetry axes of a material. The independent off-diagonal elastic stiffness cannot be determined given only the values of velocities measured along the symmetry axes. However, within planes of symmetry and along principal axes, the wave behavior and the formula linking velocities to elastic constants are often simple. Some assessment of the sample symmetry can be made by examination of the diagonal stiffness determined in the measurements.

Consequently, the elastic constants can be derived from phase velocity measurements using the different formulas depending on different cases. Here only the formulas for orthorhombic symmetry are given as an example following *Cholach et al.* (2004). It is useful to refer to Figure 2.1. The P-waves along the X, Y and Z-axes are designated by XX, YY and ZZ by propagation and polarization, respectively. For example, XX signifies X propagation and X polarization direction. The two shear waves propagating in the Y direction have X and Z direction polarizations and denoted by YX and YZ, respectively. Those propagating in the Z direction will have polarization ZX and ZY, see Figure 2.1. As such only six of the nine existing elastic constants may be determined by measurements taken along the symmetry axes of orthohombic materials. Orthorhombic is likely to be

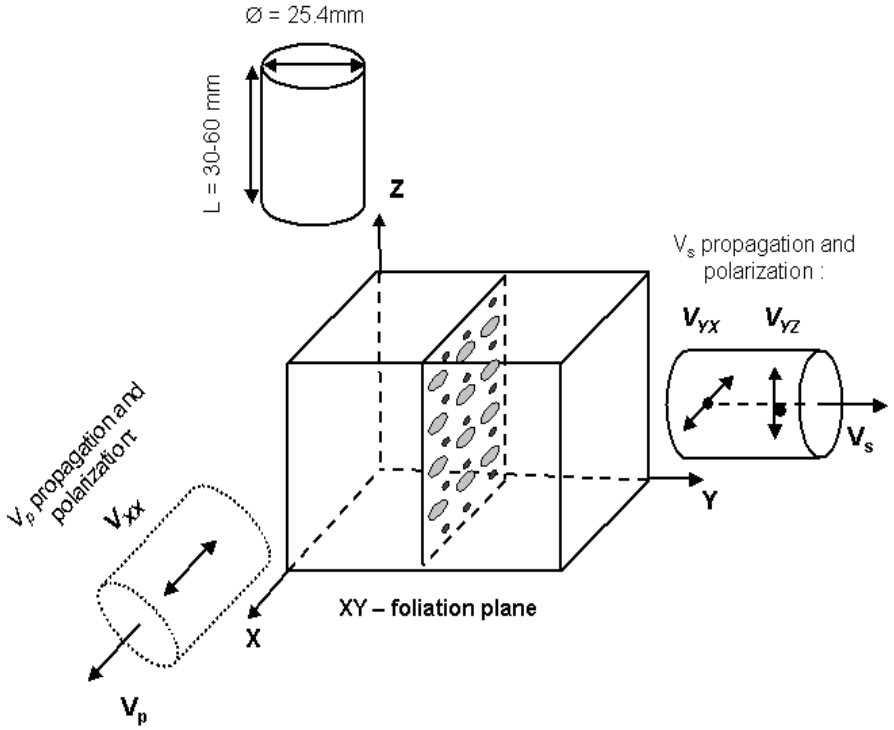

Figure 2.1: The method of mutually orthogonal plugs for measuring velocity and anisotropy (After Cholach and Schmitt, 2004). First subscript represents the direction of wave propagation while second subscript represents the direction of the wave's particle displacement or polarization direction

mostly complex symmetry intrinsically in a rock and the often two case of isotropy and tranversely isotropy could be deduced from this.

$$C_{11} = \rho V_{xx}^2, C_{22} = \rho V_{yy}^2, C_{33} = \rho V_{zz}^2, C_{44} = \rho V_{yz}^2, C_{55} = \rho V_{xz}^2, C_{66} = \rho V_{xy}^2, \tag{2.17}$$

2.4 Laboratory measurement of elastic-wave velocity and anisotropy

This study describes a set of ultrasonic laboratory techniques to measure and calculate the P- and S-wave velocity and anisotropy. The relationship between wave velocities and anisotropy and their directional dependence with confining pressure are given. In this particular study, the P- and S-wave velocities exhibit a weak anisotropy causing by

micro-crack network and the lattice preferred orientation (LPO) of the minerals in the sample.

2.4.1 Sample preparation

These samples were not selected for the study of the Pindos and Vourinos ophiolites per se, but were acquired to be used in high pressure and temperature rheologic studies by Dr. J. Escartín. As such, these samples are more olivine rich than conventional peridotites. The reason for this selection was to be able to carry out the rheological studies on a simple system (i.e. mostly olivine and serpentine family minerals). Further, the samples have small microcrack porosity as well be mentioned shortly. Samples are cut from outcrops of the Pindos and Vourinos Ophiolite (Greece). The sample plugs were drilled at the mutually orthogonal directions as illustrated in Figure 2.1, along one or two of the three axes of symmetry as the hand sample dimensions allowed. In this example study, the cores were drilled from the rock specimen in directions with respect to visible textural features.

Using the similar idea to *Johnston and Christensen* (1995), the relationship between the orientation of the sample and the foliation can be, roughly, identified by variations in the strength of the X-ray diffraction peaks observed from thin sections cut from the sample at different orientations. Here it is useful to look at the X-ray peaks for the orthorhombic forsterite [020] plane; the monoclinic clinochrysotile [002] and [004] planes; and the hexagonal brucite [001] plane. Figure C.2 (the most anisotropic) and Figure C.6 (the least anisotropic) are illustrative. The X-ray diffraction in the first cut parallel to foliation produces strong forsterite [020], clinochrysotile [002], [004], and brucite [001] peaks. In contrast, these peaks are weak in the second cut perpendicular to foliation. In olivine-rich peridotite, there is known to be a correlation of the olivine [010]-axis normal to the foliation plane (parallel to the Z-axis in Figure 2.1), and the [100]- and [001]-axis parallel to the foliation plane (*Nicolas and Poirier*, 1976; *Kern*, 1993; *Dewandel et al.*, 2003). This is not to say that the visible rock texture with high ratios are exactly in direction of the foliation, but they are relatively close. The intensity of X-ray peaks indirectly describes the relations among the orientation of the plugs, the visible rock texture, and the rock foliation. The mineralogic composition from X-ray diffraction and orientation of the

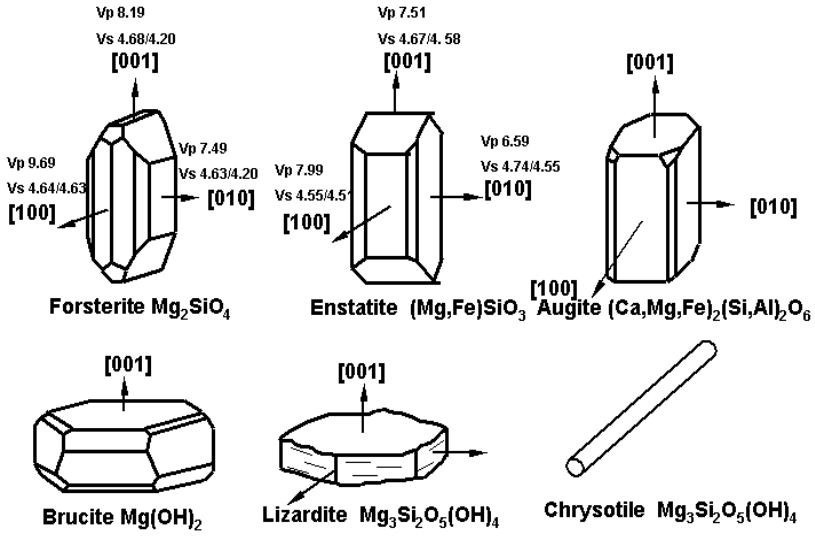

Figure 2.2: Crystal shape and symmetry of representative minerals modified from *Deer* (1992); velocity data from *Weiss et al.* (1999)

core plugs are shown in table 2.5 due to complications in determining the different types in serpentine group. The crystal shape and symmetry of major minerals in serpentinized peridotite are shown in Figure 2.2.

The diamond-cut cylindrical cores were 2.54 cm in diameter with lengths ranging from 3.0 to 6.0 cm. When each uncut specimen dimension allowed, one core was cut perpendicular to the foliation plane and at least another cut parallel to the foliation plane. The foliation used for planar fabrics depends on the grain size and the gross appearance. In cases where there is a visible lineation direction, two cores parallel and perpendicular to the lineation direction were cut within the foliation plane. If possible, additional cores were cut in the same direction to investigate the heterogeneity within a given specimen. The ends of these cores were flattened parallel using a surface grinder. Samples are prepared by grinding both faces flat to within 0.01mm and parallel to within 0.1mm. After cutting and flattening, the cores were dried in an oven for over 6 hours at a temperature of 80^0C at room pressure. Mass densities were obtained by the Archimedean displacement method and MultiPycnometer (No. MPV-60 C) on these dried samples. The porosities of

Table 2.5: The chemical composition and orientation of plugs

Sample	Density (g/cm^3)	Plugs oriented to foliation: Parallel	Perpendicular	Major minerals identified by X-ray diffraction
P03-1	3.19	P03-1, P03-1B'	P03-1B	Forsterite, Clinochrysotile, Enstatite
P04-2	2.87	P04-2	P04-2B	Forsterite, Clinochrysotile, Enstatite
P08-3	3.06	P08-3B	P08-3	
P11-1	3.28	P11-1	P11-1B	
P12-1	3.25	P12-1	P12-1B	
P13-1	2.6	P13-1	P13-1B	Clinochrysotile, Forsterite, Brucite
P13-2	2.6	P13-2	P13-2B	
P16-3	2.82	P16-3B	P16-3	Clinochrysotile, Forsterite, Augite, Magnesiohornblende
P 08-4	3.08	P08-4		
V 03-7	2.95	V03-7		
V 03-11	2.99	V03-11		

Table 2.6: The density and porosity of plugs

Sample	Density(MultiPycnometer) (g/cm^3)	Porosity $(\%)$	Density(Archimedean) (g/cm^3)
P03-1	3.24	1.5	3.19
P04-2	2.91	2	2.87
P08-3	3.09	0.3	3.06
P11-1	3.33	1.2	3.28
P12-1	3.29	1.7	3.25
P13-1	2.62	2.4	2.6
P13-2	2.63	0.6	2.6
P16-3	2.88	0.6	2.82
P 08-4	3.08	-	3.08
V 03-7	2.96	-	2.95
V 03-11	2.97	-	2.99

the samples were obtained by calculation from data by MultiPycnometer (No. MPV-60 C) and Micromeritics (GeoPyc 1360). All densities and porosity are shown in table 2.6. The porosity are typically less than 2 % at room temperature and pressure. This contention is also supported by the relatively small dependence of the sample velocities to pressure as will soon be shown. Further, no detectable permeability was found in these samples by Escartín.

Thin sections identified the macrostructure and composition of the samples. Further, SEM photos and X- ray diffraction were used to investigate the microstructure and composition of the rock and minerals. Photomicrography from the thin sections perpendicular and parallel to the foliation illustrating the microstructure are shown in Figure A.1 to A.11 in the Appendix A. The results from X-ray diffraction and a comparison of such response on thin section at mutually perpendicular orientations are shown Figure C.1 to

C.8 in Appendix. The major minerals in the samples include forsterite from the olivine group; serpentine group minerals; and enstatite and augite from the pyroxene group; a few other minerals including brucite, clinochlore, and magnesiohornblende were found only in P16-3, these help to explain its anomalously high magnetic susceptibility. We note that it is difficult to distinguish the serpentine group minerals from each other on the basis of X-ray analysis, and although the program used to analyze the X-ray results assigned the name clinochrysotile, we prefer to use serpentine group.

The piezoelectric ceramics (2.54 cm diameter, 1-MHz frequency, P-wave transducers or 18 $\times$ 18 mm size, 1-MHz frequency, S-wave transducers) were placed at both ends of the cores for the P- and S-wave measurements, respectively. To be clear, each sample needed to be prepared three times: once with the P-wave transducer and twice more with the two S-wave transducers at orthogonal orientations. An attempt to employ stacked piezoelectric ceramics in order that all the tests could simultaneously be conducted failed.

Five-minute epoxy is used to bond the transducer with the sample. The S-wave ceramics provide a mechanical pulse polarized parallel to the ends of the samples and care need to be taken to ensure that the polarization directions of both transverse mode ceramics were properly aligned to each other and appropriately oriented with respect to the rock's principal textural X, Y, and Z axes. The attached ceramic transducers and rock sample were then hermetically sealed to exclude the pressure vessel fluid from the rock and this assemblage placed in the pressure vessel. A state of hydrostatic confining stress is achieved by increasing vessel pressure; the pressure medium was a hydraulic oil. All experiments were conducted at ambient room temperature ($\sim 25^oC\, to \sim 27^oC$).

Because of the small size of the outcrop specimens, only P 03-1 was large enough to allow 3 cores to be cut. However, two of these were parallel in order to be used to check heterogeneity. In most of other rock samples, only two perpendicular cores could be drilled. The samples P 08-4, V 03-7, and V 03-11 were large enough for only one core each, and did not allow any estimate of the anisotropy to be made.

2.4.2 Experiment and Measurement

The laboratory velocity measurements were carried out using the ultrasonic pulse transmission technique (e.g. *Birch*, 1961; *Kern*, 1982). In our implementation a high voltage

(200V) rapid rise-time (∼8 ns) step-pulse from a generator (model 5800, PANAMETRICS) activates the mechanical vibrations in the source piezoelectric transducer. These mechanical vibrations travel through the rock sample and are received at the end by the receiver piezoelectric transducer that transforms the mechanical vibrations back into electrical signals. A digital oscilloscope used in the experiment receives two signals: the trigger signal from the pulse generator to synchronize the oscilloscope with the initiation of the pulse, and a delayed signal that has travelled through the rock sample to the receiving transducer.

A conventional pulse transmission technique (*Molyneux and Schmitt*, 1999, 2000) was used to obtain P- and S-wave velocities using longitudinally and transversely polarized piezoelectric ceramics, respectively. The Rock Physics Laboratory has developed a Velocity Anisotropy Measurement System that can make high-resolution measurements of many velocity components over the complete volume of rock cores. There are a number of high speed digital oscilloscopes (GaGe, Model No. 400-586-203) that are used primarily in ultrasonic measurements of P-wave and S-wave speeds through materials under pressures as great as 300 MPa and at different temperatures. The transmitting piezoelectric ceramic was activated by the fast rise-time high voltage pulse, which generated the appropriate mechanical wave. Transmission through the serpentinites is generally strong and as such no amplification was employed. The signals received by the oscilloscope are recorded in the computer. Then, the Matlab programs are developed to pick the travel time. In practice, we choose the first peak or trough to pick the first arrival. This provides a good estimation of the travel time, but also a cause of error in the velocity by attenuation.

Seismic velocities are usually measured from three mutually perpendicular directions in each sample, although this does not constitute a complete set of data for determination of all the elastic constants as noted previously. For the rocks in which both a foliation and a lineation are developed, their directions are aligned to all X, Y and Z-axes of the tectonic framework with X - parallel to the stretching lineation, Y - perpendicular to the lineation and parallel to the foliation, and Z - normal to the foliation (Figure 2.1). If the sample is foliated but not obviously lineated, both X and Y directions are arbitrarily aligned in the foliation plane.

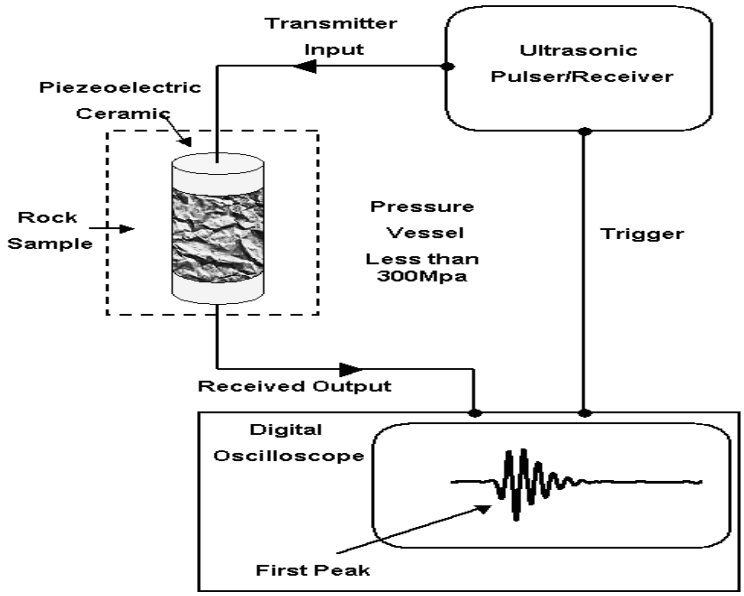

Figure 2.3: Schematic showing acoustic experiment setup

In this study, the P- and S-wave velocities of rock samples are measured using the pulse transmission technique (instrument setup shown in Figure 2.3). Transmitting and receiving transducers were mounted at the opposing ends of the cylindrical samples. P-wave and two S-wave measurements were made on all the cores in longitudinal mode. One or two sets of sample could be used for each run. Each sample requires 1 P-wave and at least two orthogonally oriented S-wave runs. In each run, waveforms were acquired over the range of confining pressure from 0 to 300 MPa with an interval of 5 MPa and back. Pressure is applied not so much to mimic $insitu$ conditions but to close as much of the micro-crack porosity in the rocks as possible in order that the velocities are representative of the intrinsic mineralogical texture of the sample.

The time difference between the two signals received by the oscilloscope is the time that it takes the signal to travel through the electrical leads as well as through the sample itself. The electrical delay can be eliminated according to laboratory measurement and calculation. The velocity of the sample is calculated from its length and travel time of the

signal after correcting for the delay time.

$$V = \frac{L}{t_T - t_D} \tag{2.18}$$

Where: V is P-wave or S-wave velocity; L is the length of the sample; t_T is the travel time of signal; t_D is the delay time

2.4.3 Error analysis

Using a method similar to that described by *Yin* (1992), the absolute errors in the measurement may be analyzed by the partial differentiation from the equation (2.18):

$$\triangle V = \frac{\partial V}{\partial L}\triangle L + \frac{\partial V}{\partial t_D}\triangle t_D + \frac{\partial V}{\partial t_T}\triangle t_T \tag{2.19}$$

And the absolute error can be evaluated as

$$\triangle V = \triangle L \left|\frac{1}{t_T - t_D}\right| + L \left|\frac{\triangle t_T}{(t_T - t_D)^2}\right| + L \left|\frac{\triangle t_D}{(t_T - t_D)^2}\right| \tag{2.20}$$

Where $\triangle t_T$ and $\triangle t_D$ are taken to be the oscilloscope's time resolution of 125 million samples per second (i.e., 8 ns per sample), and $\triangle L$ is the absolute error in sample length measurement. To estimate errors we considered a typical sample length of 30 mm measured with a precision 0.01 mm by the electronic digital caliper over the flattened faces, $\triangle L$ can be less than 0.1 mm. Since $t_T - t_D$ is in the range from 4.3 to 11 μs and is typically near 7 μs for P wave in these experiments, for typical P wave velocity the error calculated by the above equation to be $\pm$ 24 m/s. This corresponds to a relative error in the velocity estimation of approximately 0.4 % for a P-wave propagating at a velocity near 6000 m/s. Similarly, for the S-waves $t_T - t_D$ is in the range from 8 to 20 μs and typically near 14 μs, then, the maximum absolute error $\triangle V$ will be 10 m/s in the case of others are as same as before. This corresponds to a relative error in the velocity estimation of approximately 0.3 % for a S-wave propagating at a velocity near 3500 m/s.

2.5 Results and Discussion

In this study, P- and S-wave velocities have been measured on 20 cores in total (see table B.1 to B.11). P-wave and two S-wave measurements were made on all the cores. Each

sample requires one P-wave and at least two orthogonally oriented S-wave runs. In each run, waveforms were acquired over the range of confining pressure from 0 to 300 MPa and back with an interval of 5 MPa. A good deal of efforts goes into the core sample sealing because the hydraulic oil would destroy the sample if it ever penetrate the package. Despite our best efforts, this does on occasion happen. After each measurement each core sample package is carefully examined for leakage. If these unexpected situations occurred, the sample was cleaned and the whole process repeated again in order to achieve the precise results. The data of velocities for all samples are provided in Appendix.

The results from one S-wave run consisting of 79 traces (i.e. the image of amplitude with time at different pressures) highlights the well-known decrease in pulse transit times and the increment in amplitude with increasing confining pressure (Figure 2.4). Figure 2.5 is a graph of a S-wave pulse train taken from one of the waveforms imaged in Figure 2.4. The pulse first extremum (here a negative polarity) was used to determine the transit time and in Figure 2.5 this is the first trough. The S-wave waveforms acquired in a complete pressure cycle are shown in Figure 2.6. An example of the velocities and anisotropy measurements during both pressurization and depressurization is shown in Figure 2.7 for sample P 12-1.

2.5.1 Compressional wave results

Compressional wave results for 11 samples from Pindos and Vourinos Ophiolites (Greece) are presented with respect to confining pressures from 0 to 300 MPa. Because of the low porosity, the values and slopes of velocities measured as the pressure increases and decreases are similar in this study (Figure 2.7). But, generally velocities measured as the pressure is increased tend to be lower than those measured during depressurization. This phenomenon has been attributed to the closure of microcracks at high pressure that do not completely reopen during depressurization (*Birch*, 1960). All velocities reported were measured while increasing pressure in Table 2.7. The Vp vs. pressure curves for all samples display an initial non-linear increase in velocity at low pressures followed by a more gradual linear increase at high pressures. This characteristic curve has been attributed to closure of microcracks in the samples with increasing pressure to 100 MPa, above which the rocks can be considered as compacted aggregates (*Birch*, 1960; *Christensen*, 1965). In

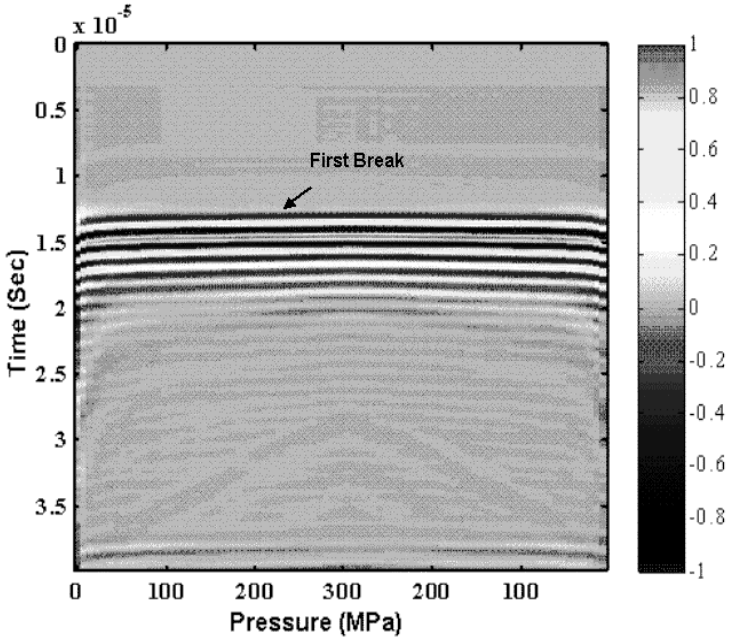

Figure 2.4: Waveform trace during one pressure cycle. Color bar corresponds to waveform amplitude (P 11-1)

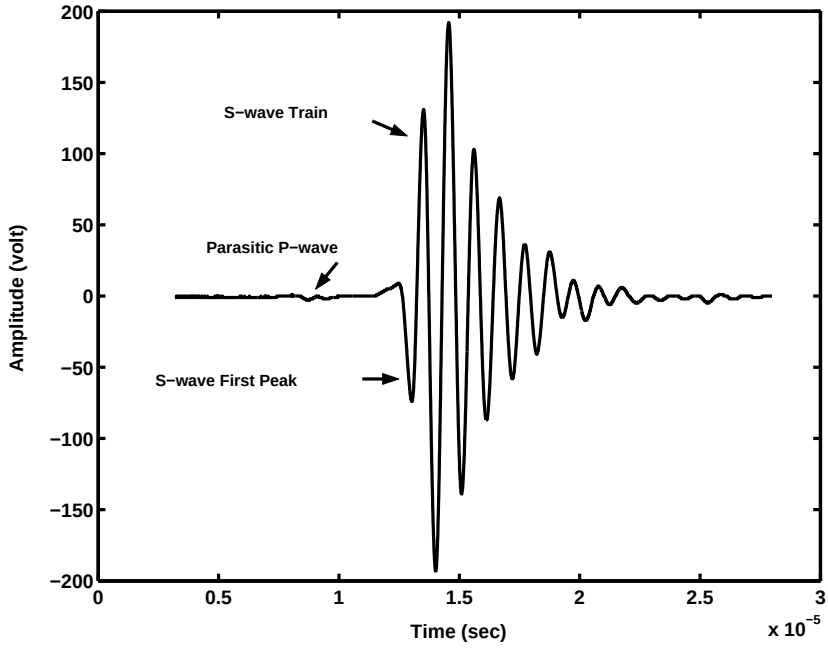

Figure 2.5: An example of typical shear wave trace from figure 2.4

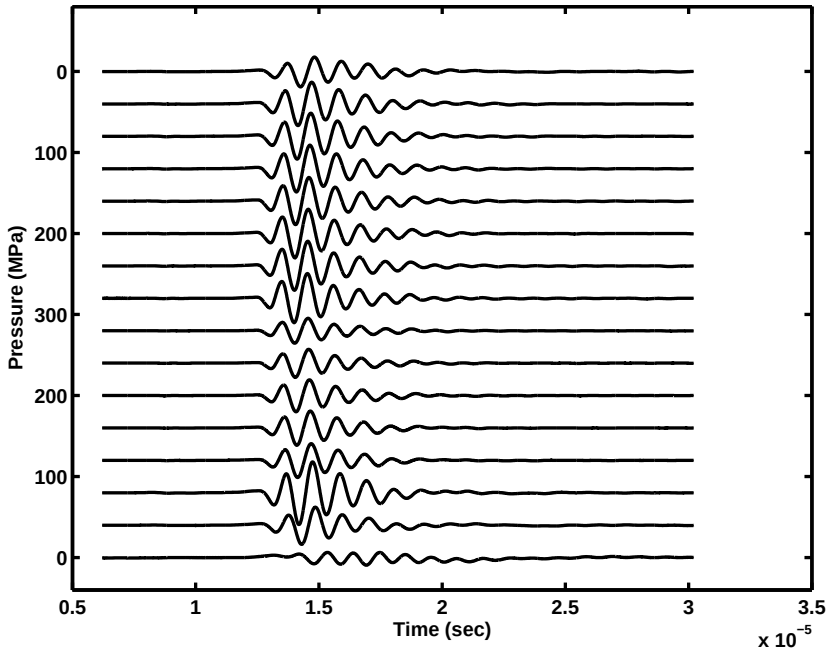

Figure 2.6: Acquired S-wave waveforms using pulse transmission method (sample P11-1, ZY plane).

general, however, it must be noted that the rocks currently under study initially display highly linear velocity versus pressure behavior that begins even at pressures below 50 MPa. This is usually not the case for igneous or metamorphic rocks that contain microcracks, and suggests that the microcrack porosity in these samples is small.

The degree of serpentinization of the samples has been estimated by mass density measurement, using the linear relationship between density and serpentinization established by *Christensen* (1966b, 1972). Basically, high mass density corresponds to low serpertinization because of low-density feature of serpentine minerals. A comparison between sample P 03-1, which has only a low serpentinization (density 3.19 g/cm^3; serpentine ratio 13.6 %), and sample P 13-2 in Figure 2.8, which is highly serpentinized (density 2.6 g/cm^3; serpentine ratio 87.9 %), suggests that degree to which velocity increases with pressure is initially related to the rock microstructure and mineralogy. Samples with low serpentiniztion exhibit more a pronounced rise in velocity, P-wave anisotropy, and $\frac{dV_p}{dP}$ slope than the highly serpentinized samples at pressures less than 50 MPa. The thin sections of P 03-1 and P 13-2 are shown in Figure A.1 and A.8 in Appendix, which give a

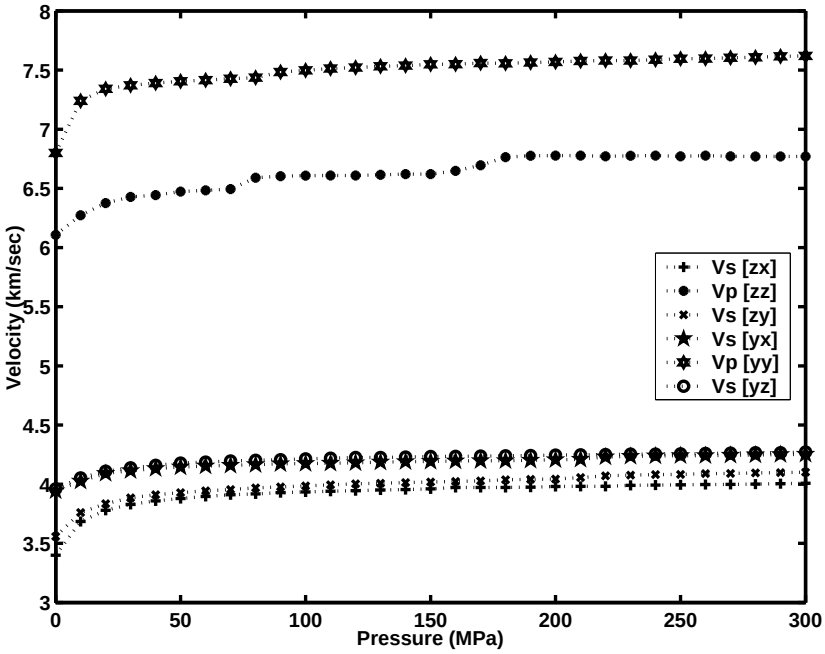

(a)

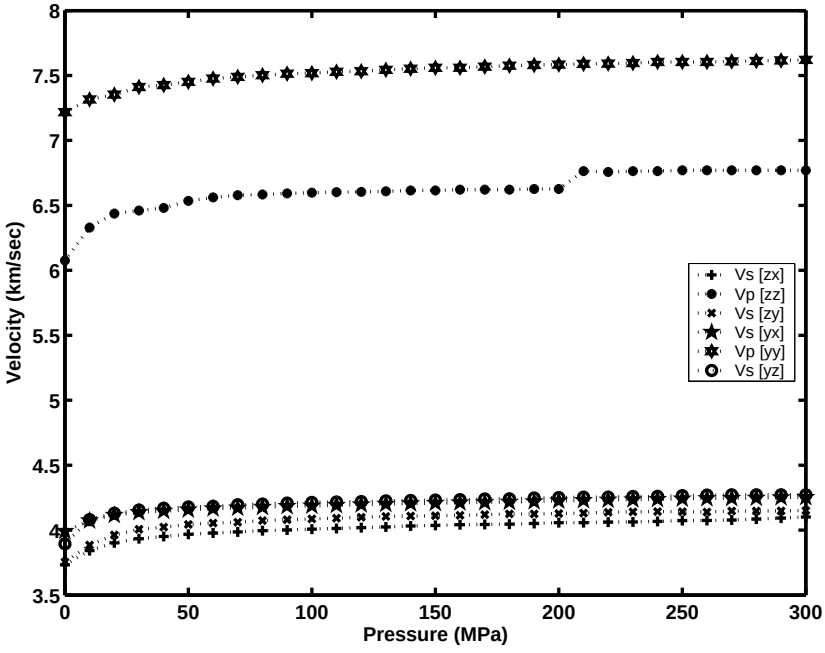

(b)

Figure 2.7: Measurements of velocities and anisotropy (P 12-1). Top: Velocities as pressure increases. Bottom: Velocities as pressure decreases

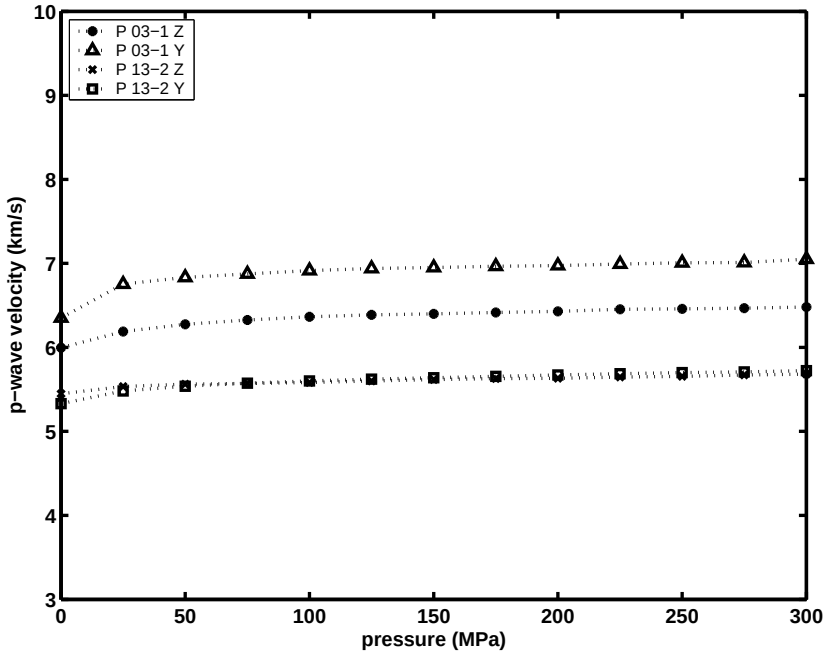

Figure 2.8: P-wave velocities vs. pressures in Z, and Y directions through sample P 13-2 and P 03-1

general image of rock texture as typical samples by high and low serpentinization degree at the microscopic ($\times$50) scale.

Above 50 MPa the velocity-pressure relationship can be described by the linear equation:

$$V_p = (V_p)_0 + P(dV_p/dP) \tag{2.21}$$

Where $(V_p)_0$ is the projected zero pressure velocity and $\frac{dV_p}{dP}$ is the high-pressure slope. $(V_p)_0$ and $\frac{dV_p}{dP}$ for each sample are given in Table 2.7, with average $\frac{dV_p}{dP}$ varying from 4 to $9 \times 10^{-4} km/s/MPa$.

The average P-wave velocity, which is equal to $[Vyy + Vzz]/2$ in this study (for these samples that allowed for multiple measurements), is shown as a function of pressure in Figure 2.9. With increasing pressure, all the P-wave velocities rapidly rise in the low-pressure range (less than 100 MPa) due to closure of most of the microcracks; then, at higher pressures the increment of velocity tends to be slower. In general, $V_p(zz) < V_p(yy)$; the sample P 08-3 and P16-3 show the reverse relationships between first and second sample P-wave velocity measurement by the reason of sampling orientation. A general

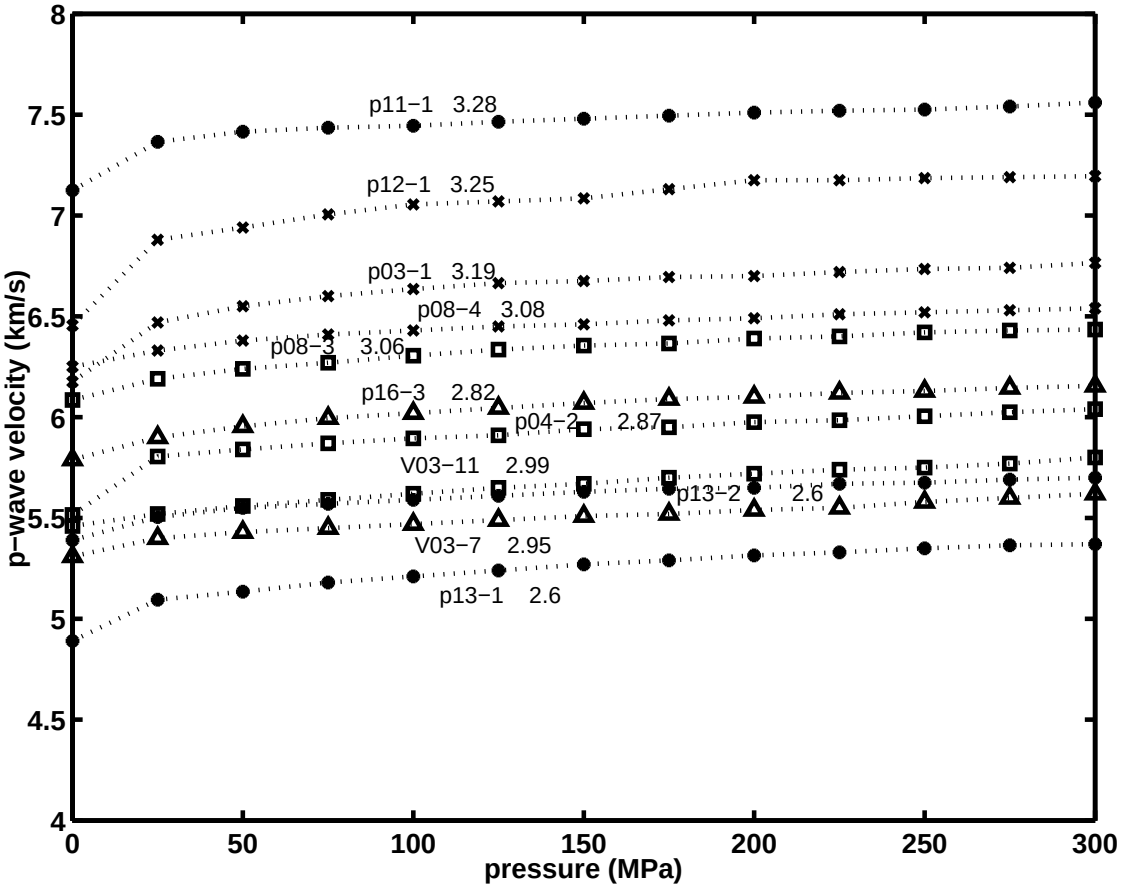

Figure 2.9: Mean P-wave velocities as a function of pressure at room temperature; average density following the sample name.

trend of decreasing velocity with decreasing density is apparent in Figure 2.10.

The densities were determined at room pressure because the effect of pressure on density is small for such low-porosity samples ($< 2\%$). Figure 2.9 also illustrates the variation of the mean P-wave velocity among the samples. Density is the major influence because of the relatively low level of anisotropy and the heterogeneity of the samples. Although the average P-wave velocity generally increases with density, the velocity anisotropy or the heterogeneity of some samples may still gives rise to considerable velocity scatter in the P-wave velocity-density relationship.

The coefficient of anisotropy was defined by *Birch* (1961) as:

$$A = 100\%(V_{max} - V_{min})/V_{mean} \tag{2.22}$$

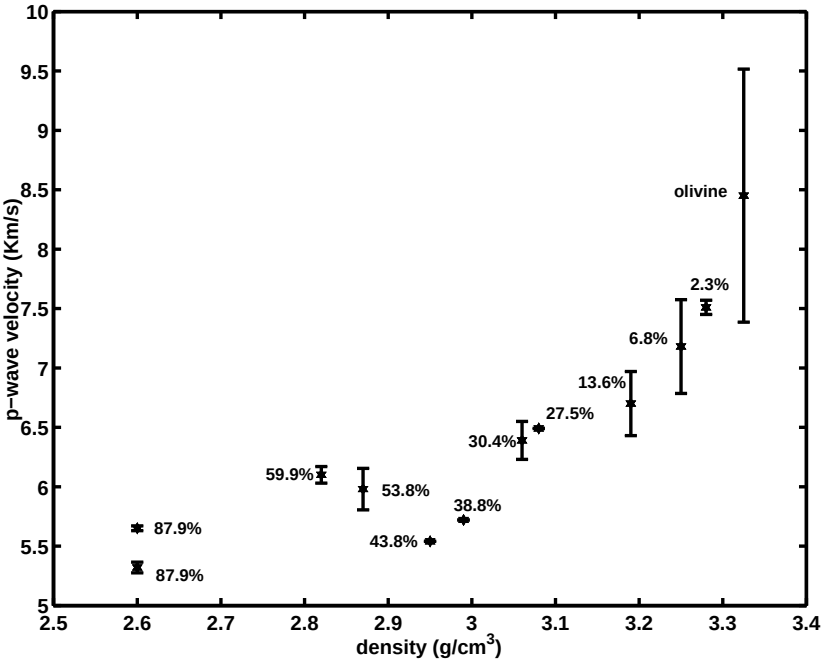

Figure 2.10: Mean Vp vs. density at 200 MPa and room temperature (Errorbar range from Vmin to Vmax; percentage is serpentinization degree)

In many samples, A varies with pressure and density. The general relationship between density and P-wave anisotropy can be shown in the Figure 2.11. The P-wave anisotropy increases roughly with increasing density, except for the sample P11-1 due to its randomly aligned grain texture (see its thin section Figure A.5 in Appendix). This suggests that the serpentinization decreases the anisotropy in the material studied here.

In general, two patterns have been observed in the relationships between pressure and P-wave anisotropy (Figure 2.12):

Pattern 1: the anisotropy for 2 samples (P 12-1 and P03-1, both low serpentinization) increases rapidly with increasing pressure in the low-pressure domain ($<$ 50 MPa), and then decreases in the high-pressure domain (Figure 2.12). This variation can be attributed to the rapid closure of oriented cracks at low pressure that oppose the LPO anisotropy (*Ji and Salisbury*, 1993a; *Ji et al.*, 1993b). Pattern 2: the anisotropy for 5 samples (P04-2, P08-3, P13-2, P11-1 and P16-3) decreases with increasing pressure in the low-pressure domain ($<$ 50 MPa), and then increases slightly in the high-pressure domain (Figure 2.12). These samples are mostly quasi-isotropic and highly serpentinized. The relationship between

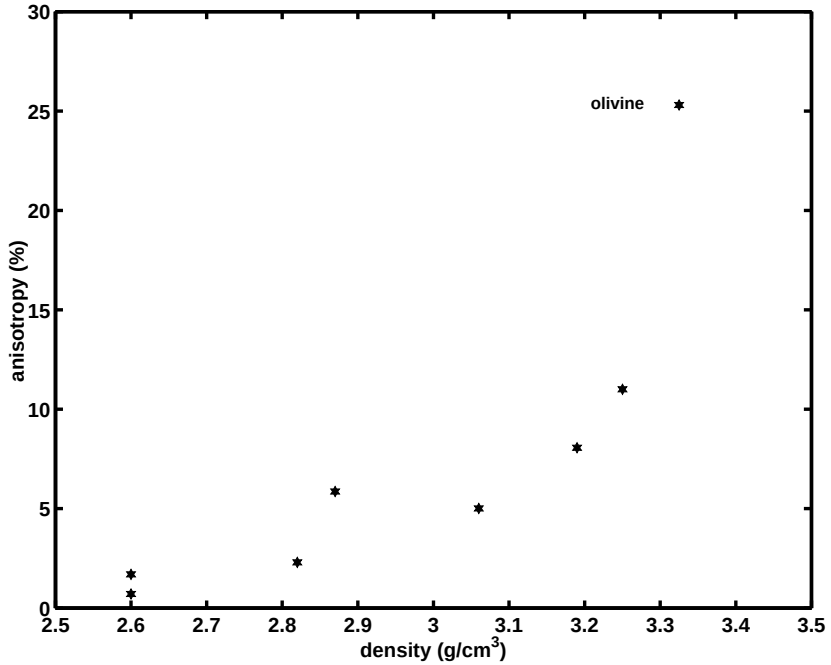

Figure 2.11: P-wave anisotropy vs. density at 200 MPa and room temperature

Vp anisotropy and confining pressure can be attributed to the closure of the oriented microcracks, which reinforce the anisotropy due to the lattice-preferred orientation (LPO) of rock-forming mineral. The slight increase of Vp anisotropy with increasing pressure probably results from differences in the pressure sensitivity of Vp in the X, Y and Z directions.

2.5.2 Shear wave results

Table 2.8 lists the measured shear-wave velocities for 11 samples from Pindos and Vourinos Ophiolites (Greece) as a function of pressure, propagation direction and polarization direction. The velocities were measured during pressurization. In general, velocities measured during pressurization tend to be lower than those observed during depressurization in our pressure range.

As with the P-wave velocities, many of the samples display a rapid, non-linear increase in Vs (< 50 MPa) and that evolves to a slower linear increase at higher pressure (Figure 2.13). This character has been attributed to closure of microcracks in the samples

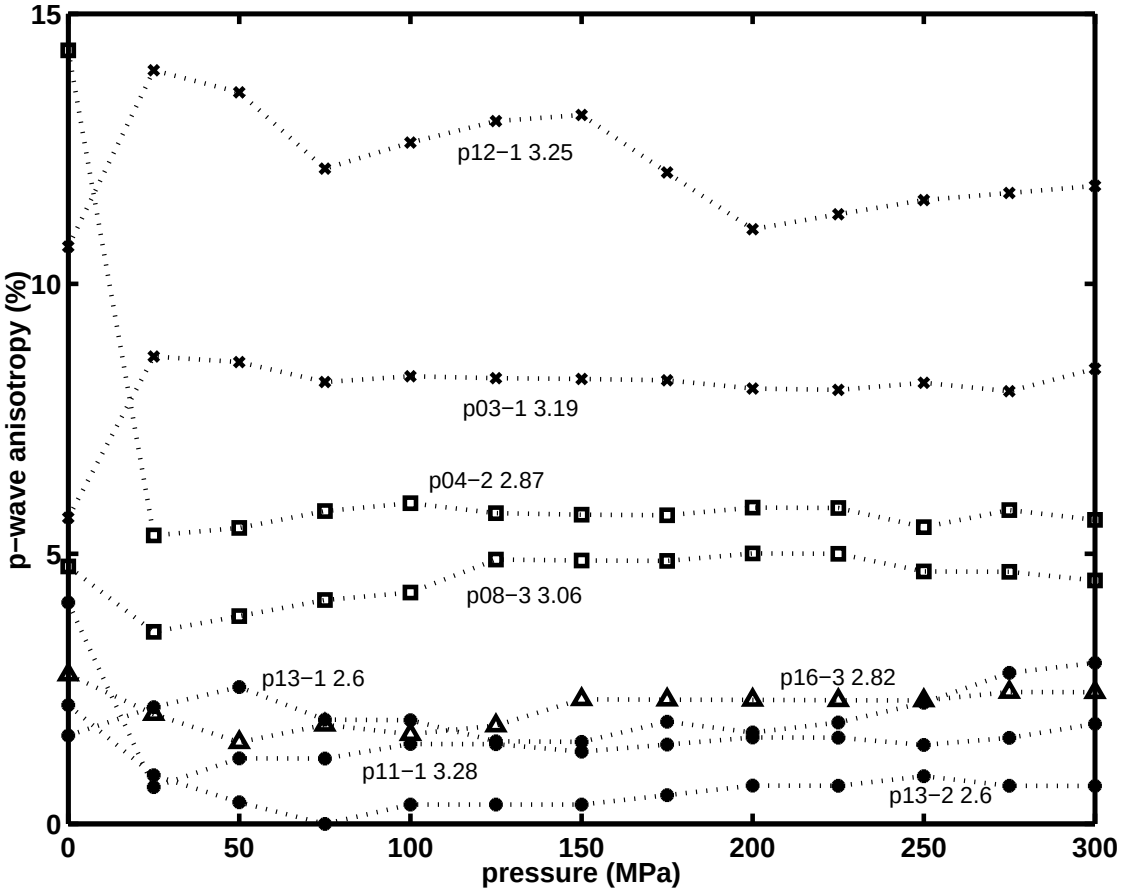

Figure 2.12: P-wave anisotropy vs. pressure; average density following the sample name

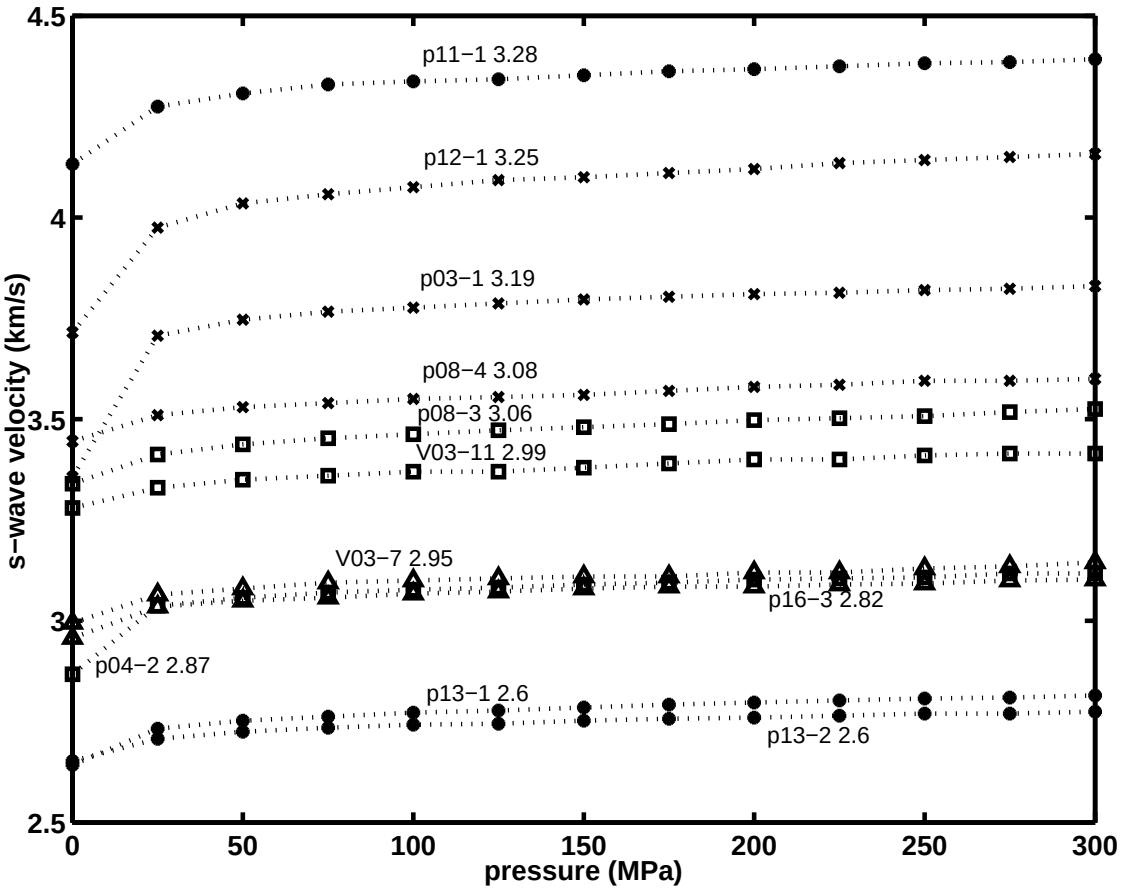

Figure 2.13: Mean S-wave velocities as a function of pressure at room temperature; average density following the sample name

at low pressures (e.g. *Birch*, 1960). The rocks can be considered as a compact aggregate (*Christensen*, 1965) and the velocity-pressure relationship can be described by the linear equation in the high-pressure range:

$$V_s = (V_s)_0 + P(dV_s/dP) \tag{2.23}$$

Where $(V_s)_0$ is the projected zero-pressure velocity (in km/s), and $\frac{dV_s}{dP}$ is the high-pressure slope; $(V_s)_0$ and $\frac{dV_s}{dP}$ for each sample are given in Table 2.8, with average $\frac{dV_s}{dP}$ varying from 2 to $4.25 \times 10^{-4} km/s/MPa$ at pressures above 50 MPa.

The mean shear-wave velocity in this study, defined as: $[Vyx + Vyz + Vzx + Vzy]/4$, is plotted as a function of pressure in Figure 2.13. While the shear wave velocities are

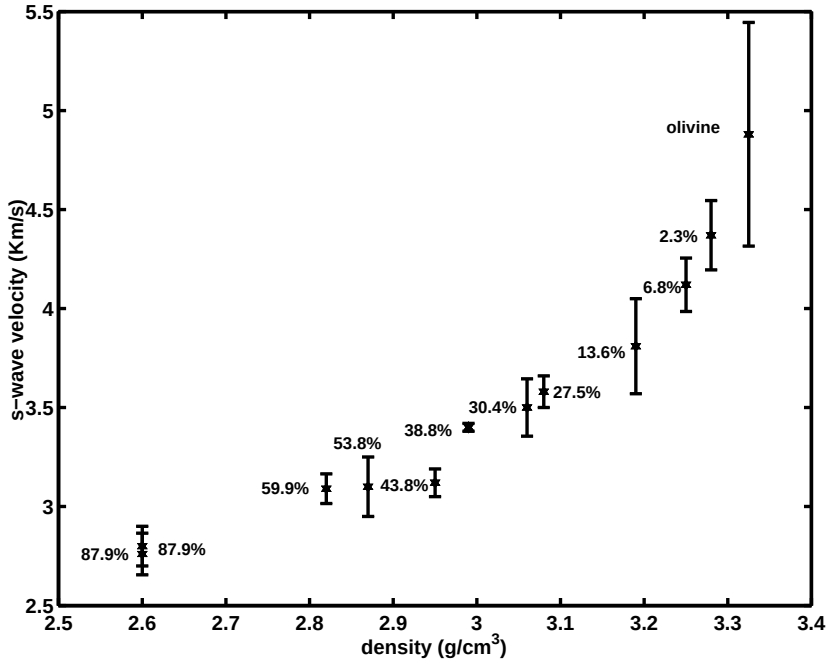

Figure 2.14: Mean Vs vs. density at 200 MPa and room temperature (Errorbar range from Vmin to Vmax; percentage is serpentinization degree)

sensitive to microcracks and density, as noted above, the higher density samples (P 03-1, P12-1, P11-1) display high average velocities (3.81 - 4.37 km/s, 200MPa). The samples with high serpentinization degree (P 13-1 and P 13-2) display much lower average velocity (2.76 - 2.8 km/s, 200MPa).

Figure 2.14 illustrates the variation of S-wave velocity with density. The S-wave velocities show the clear and constant increment with density.

Figure 2.15 illustrates the variation of S-wave anisotropy with density. There is not a clear relationship between S-wave anisotropy and density.

Figure 2.16 illustrates the variation of the Vp/Vs ratio and Poisson's ratio with density at 200 and 50MPa, respectively. In general, both the Vp/Vs ratio and Poisson's ratio are larger at 200MPa than at 50 MPa; the Vp/Vs ratios and Poisson ratios have similar slopes of -0.5 and -0.15 and uniform decrease with density at 50 MPa and 200 MPa. That is, there is a continuous increment of Vp/Vs ratio and Poisson's ratio with the serpentinization degree in Pindos and Vourinos Ophiolite. The Poisson's ratio and Vp/Vs ratio at 200 MPa are shown in table 2.9.

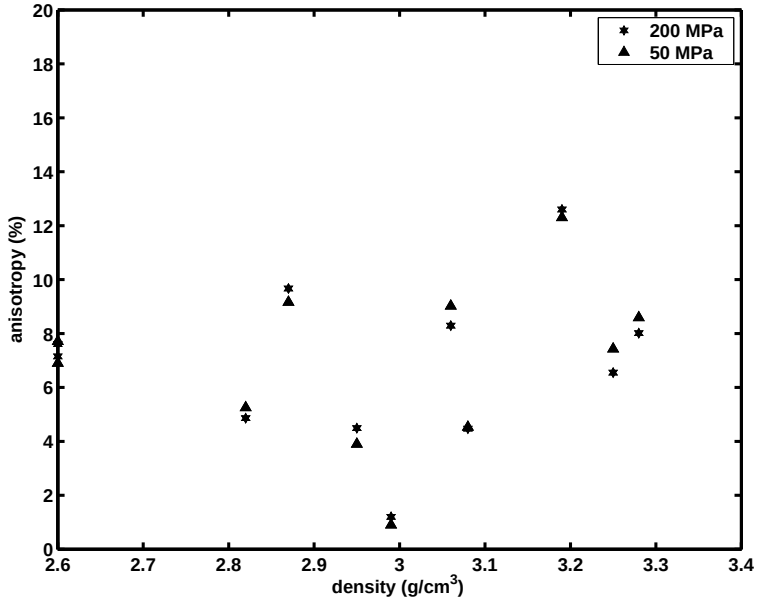

Figure 2.15: S-wave anisotropy vs. density at 200 MPa and room temperature

The shear-wave anisotropy coefficient, A_s, is defined as:

$$A_s = 100\%(Vs_{max} - Vs_{min})/Vs_{mean} \tag{2.24}$$

Figure 2.17 illustrates the variation of S-wave anisotropy with pressure(less than 50 MPa). S-wave anisotropy generally increases with increasing pressure at low pressure except P04-2 and P12-1. We attribute this variation to the rapid closure of oriented cracks at low pressure that oppose the LPO anisotropy. For P04-2 and P12-1, S-wave anisotropy decreases with increasing pressure at low pressure. This relationship can be attributed to the closure of the oriented microcracks that reinforce the anisotropy. As pressure higher than 50 MPa, all variations are small, and gradually reach a constant value.

The shear-wave splitting coefficient $(\triangle V_s)$ is defined as the difference in velocity between two orthogonally polarized shear waves traveling in the same propagation direction. As can be seen in Table 2.7 and Figure 2.18 and 2.19, $\triangle V_s$, is sensitive to a variety of factors, including pressure, overall mineralogy and propagation direction. The shear-wave splitting of samples increase or decrease in low pressure (less than 50 MPa) depending on amount of microcracks and if their directions reinforce or oppose the anisotropy. In the high-pressure field, $\triangle V_s$, roughly approaches a constant value, indicating that it is

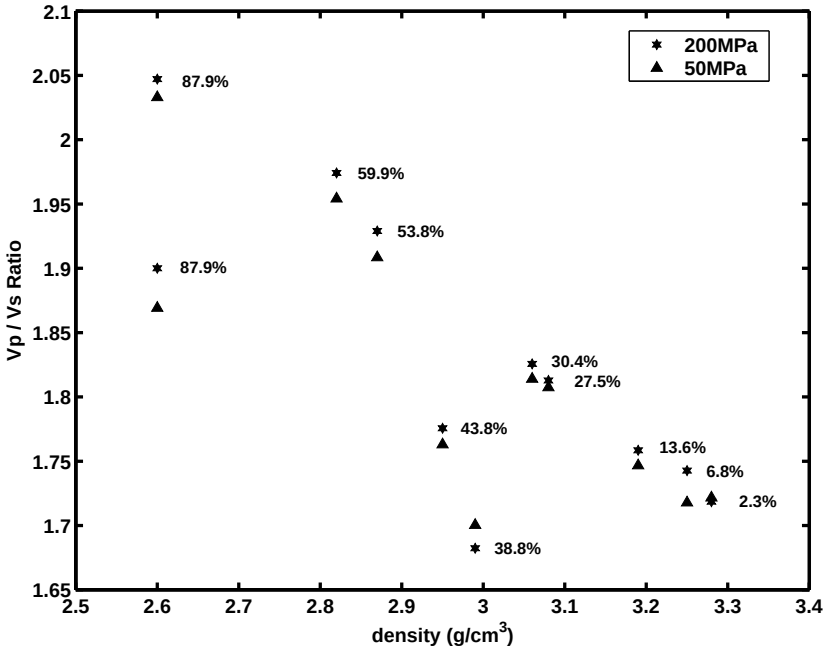

(a)

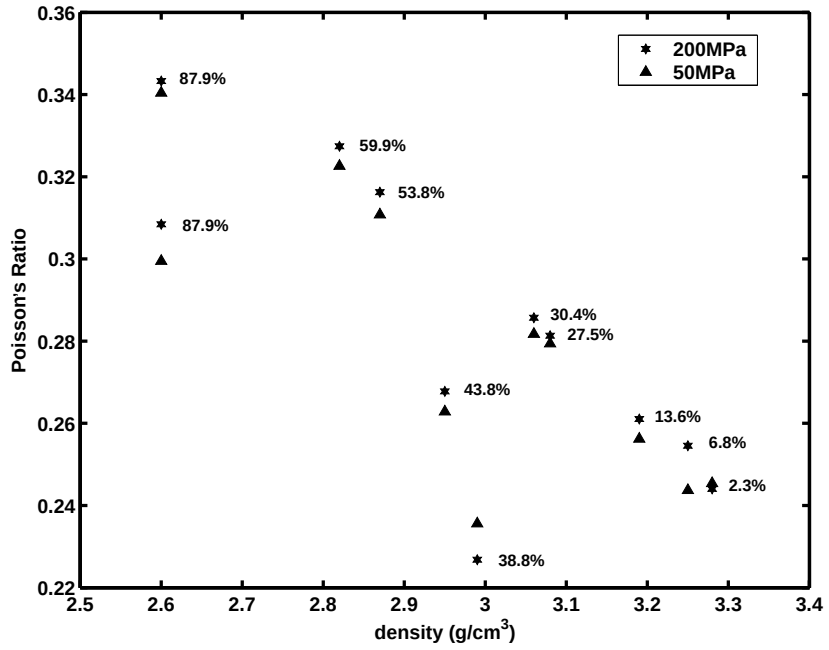

(b)

Figure 2.16: Poisson's Ratio and Vp/Vs ratio vs. density at 200 / 50 MPa and room temperature; percentage is serpentinization; Top: Vp/Vs ratio vs. density Bottom: Poisson's Ratio vs. density; $\sigma = \frac{1}{2}\left\{1 - 1/[(\frac{V_p}{V_s})^2 - 1]\right\}$

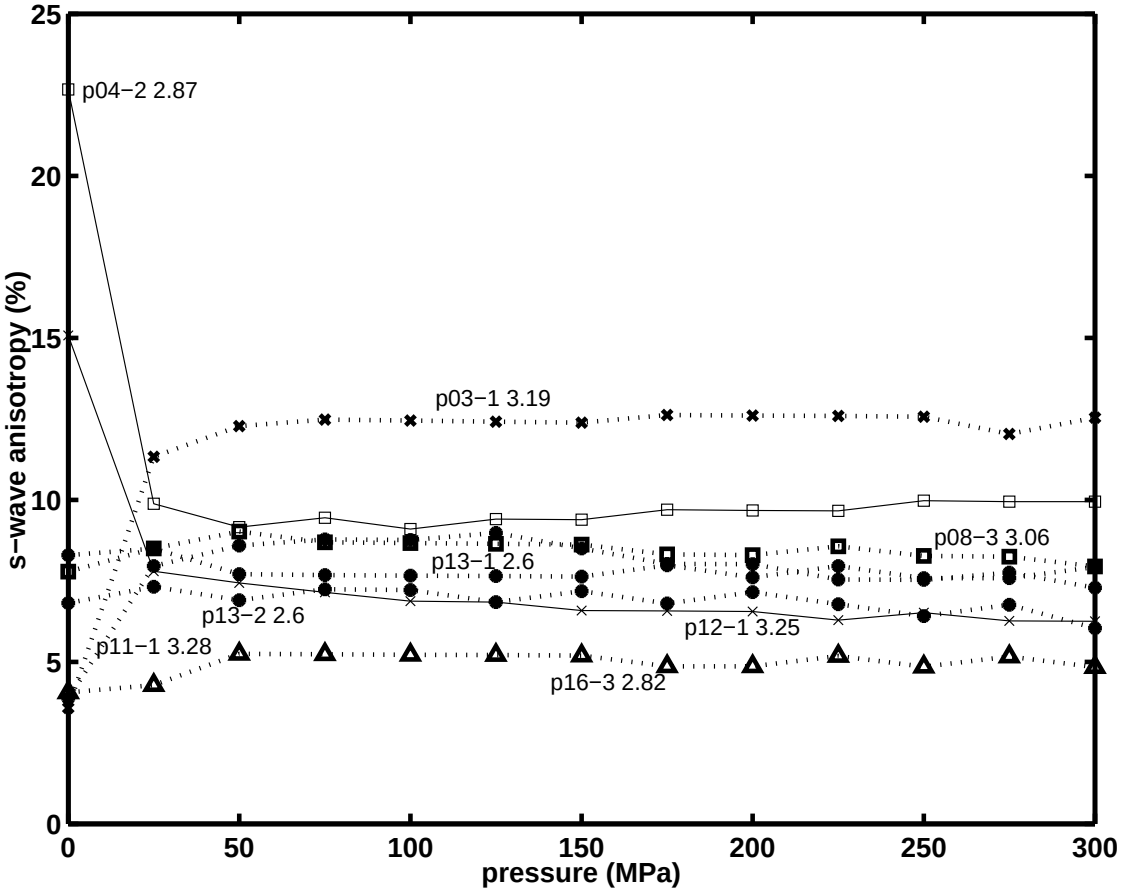

Figure 2.17: S-wave anisotropy vs. pressure; average density following the sample name

controlled by the intrinsic properties (i.e., the mineralogy and LPO) of the rocks. Below the "crack-closing pressure", microcracks make a contribution to shear-wave splitting, as proposed by *Crampin* (1981). In general, the samples with lowest density have the smallest S-wave splitting in all directions. This again reinforces the observation of decreasing anisotropy with degree of serpentinization. For most samples the S-wave splitting usually ranges from 0.02 to 0.2 km/s. Generally, the largest splitting at elevated pressures is observed for waves propagating parallel to the foliation (parallel to X or Y). The most pronounced shear-wave splitting is observed in samples P 03-1 and P 11-1. As can be seen in Table 2.8 and Figures 2.18 and 2.19, for these two samples (with low degree of serpentinization), $\triangle V_s(Y) > \triangle V_s(Z)$ and $\triangle V_s$ typically ranges from 0.35 to 0.48 km/s in the foliation plane in these samples. The least shear-wave splitting value is observed for propagation perpendicular to foliation.

The shear wave splitting (SWS) along the Y and Z directions and density does not display a clear relationship in Figure 2.20. In general, the samples in high serpentinization degree, with low-density, have low SWS values.

2.5.3 Elastic stiffness and symmetry

Elastic stiffnesses C_{ij} are calculated and estimated directly from the observed phase velocities. Table 2.10 lists the calculated elastic stiffnesses for 11 samples from Pindos and Vourinos Ophiolites (Greece).

Determination of elastic stiffnesses from the ultrasonic phase velocity measurements has long been employed (*Cheadle et al.*, 1991; *Mah*, 1999; *Mah and Schmitt*, 2003). Within planes of symmetry and along principal axes, the elastic constants can be derived from phase velocity measurements using the formulas dependent on symmetry (Eq. 2.17).

In this study, the samples are characterized on the basis of the observed texture and the assumed symmetry. Samples in which the elastic moduli differ by less than the expected levels of uncertainty are assumed to be quasi-isotropic. In principal, those in which $C_{11} \approx C_{22} \neq C_{33}$ and $C_{44} \approx C_{55} \neq C_{66}$ are considered to be transversely isotropic. And those with $C_{11} \neq C_{22} \neq C_{33}$ and $C_{44} \neq C_{55} \neq C_{66}$ are orthorhombic. Unfortunately, the velocities in the Y and Z directions were measured meaning that the elastic constants C_{22} and C_{33} could be determined. The stiffness C_{11} was not determined in these tests.

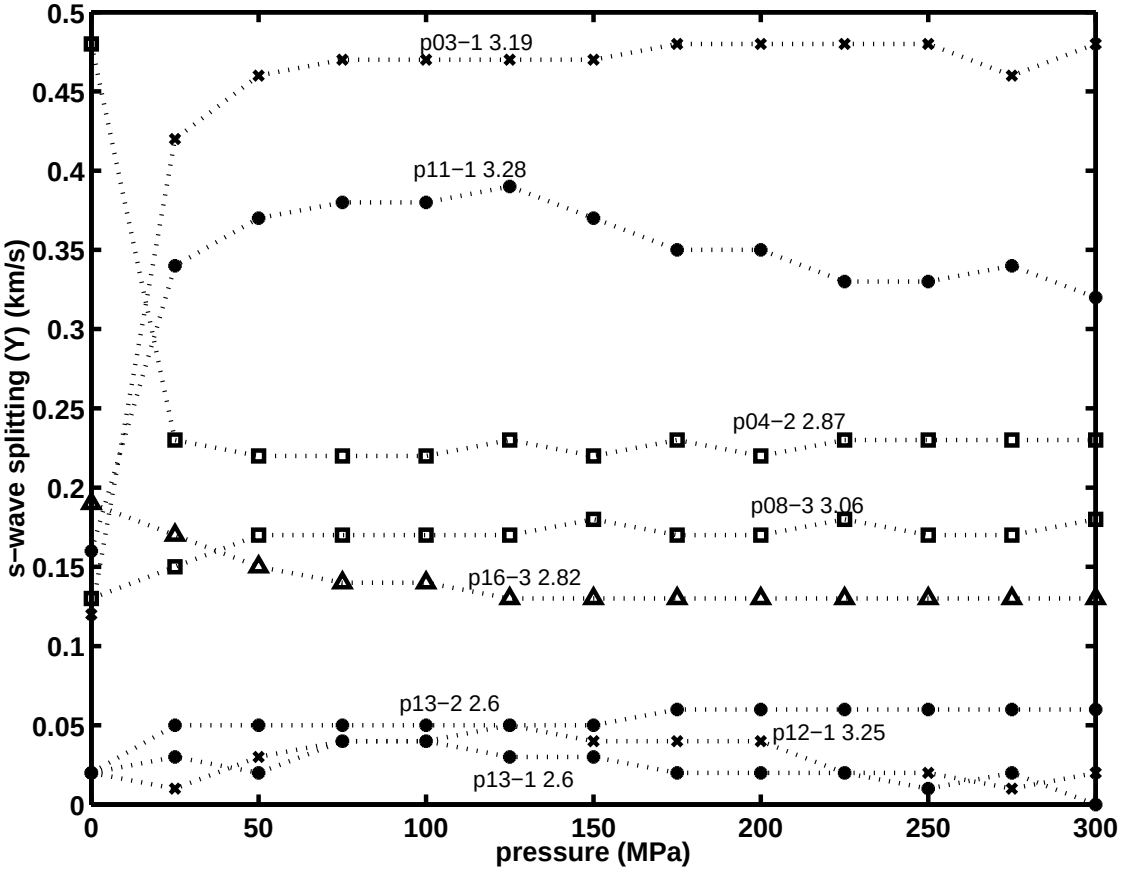

Figure 2.18: S-wave splitting (Y) vs. pressure; average density following the sample name

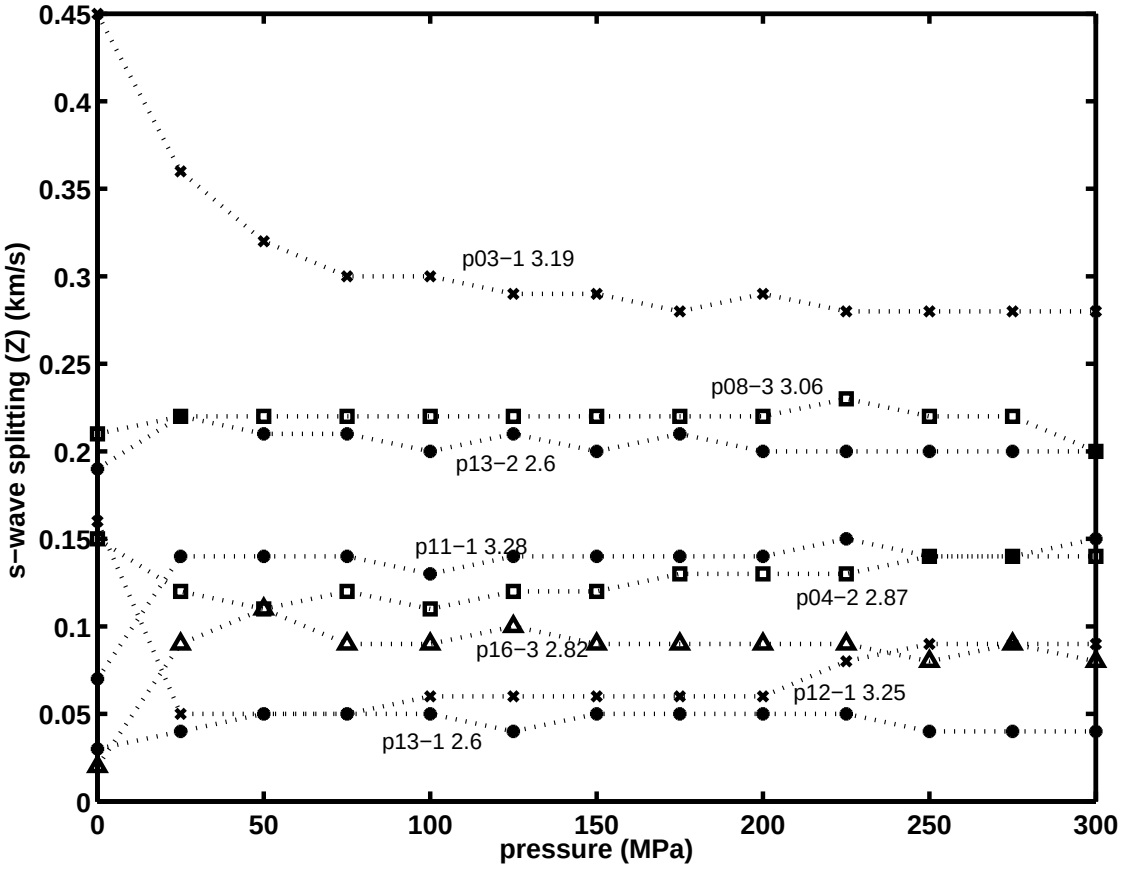

Figure 2.19: S-wave splitting (Z) vs. pressure; average density following the sample name

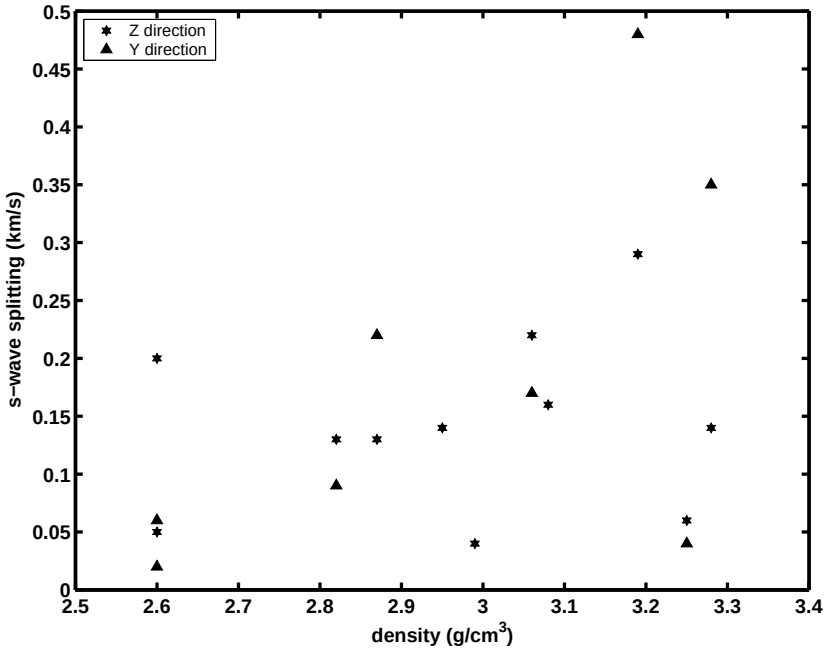

Figure 2.20: Shear wave splitting vs. density at 200 MPa and room temperature

The symmetry of samples can only be estimated and assessed by examination of other stiffnesses determined in the measurements. As the degree of serpentinization increases, the elastic stiffnesses of all the samples decrease, and the symmetry tends to evolve from orthorhombic to quasi-isotropic. These results are summarized in table 2.10.

2.5.4 Conclusion

In this study, the seismic properties and their directional dependence have been measured in eleven serpertinized dunite rock outcrop samples from Pindos and Vourinos ophiolites (Greece). The compressional velocities were measured to confining pressures of 300 MPa in mutually orthogonal directions to investigate anisotropic properties with respect to the visible textural properties of rocks. The shear-wave velocities were measured at two orthogonal polarizations for each direction to determine shear-wave splitting and correlate it with P-wave anisotropy. Once the material is anisotropic there will generally be compressional waves propagating with different velocities in the different directions, and the polarizations of two distinct shear waves propagating will lead to the shear wave splitting. For all the samples, $V_p(Z) < V_p(Y)$. Shear wave splitting with

$\triangle V_s(Y) > \triangle V_s(Z)$ is obvious only in samples P 03-1, P11-1, and P 04-2. Sample symmetries estimated from relative values of the determined elastic constants show two types of quasi-isotropic and orthorhombic.

The density, serpentine ration β, mean velocities, anisotropies, and shear wave splitting (200MPa), are summarized in Table 2.11. In general, the P- and S-wave velocities, the percentage of P- and S-waves anisotropy, and the shear wave splitting decreases with increasing degree of serpentinization.

As found in the work of other authors (*Ji and Salisbury*, 1993a; *Ji et al.*, 1993b; *Barruol and Kern*, 1996; *Kern et al.*, 1996; *Dewandel et al.*, 2003), the P- / S-wave velocity and anisotropy measured here on eleven samples from Pindos and Vourinos ophiolite (Greece) exhibit an intrinsic anisotropy controlled at low pressures by the microcrack network and at higher pressures by the lattice preferred orientation of olivine and serpentine. Our result and the laboratory relationships between velocities and density by different authors (*Christensen*, 1965, 1966a,b; *Kern*, 1993; *Horen et al.*, 1996) for serpentinite and peridotite are shown in Figure 2.21. Observed Vp anisotropy varied from quasi-isotropic to weakly anisotropic (Ap = 11%). The pressure invariance of the observed P-wave anisotropy and the shear-wave splitting above 100 MPa indicates that the microcracks play only a small role even at lower pressures, and that the lattice preferred orientation (LPO) is mainly responsible for the measured seismic anisotropy in these rocks.

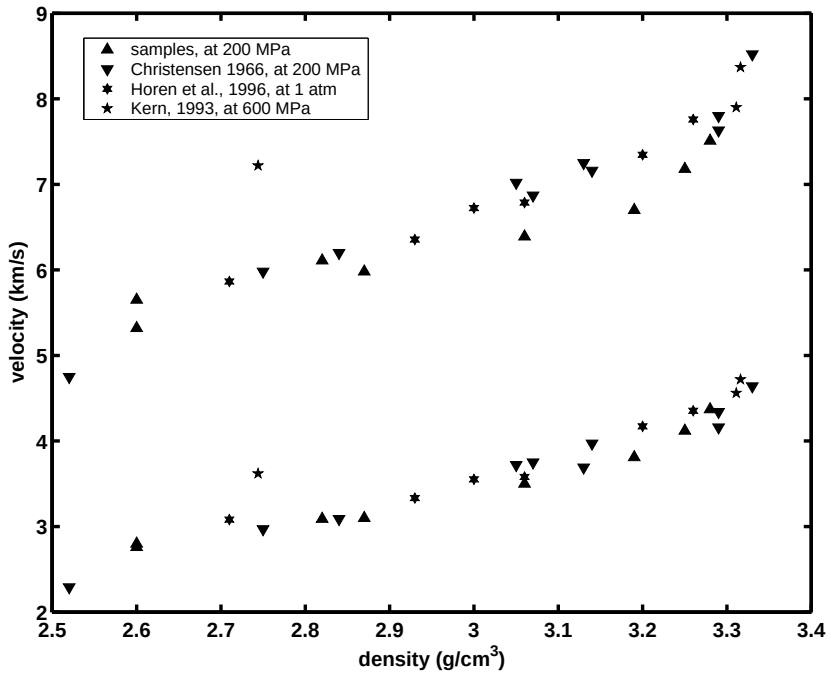

Figure 2.21: Mean velocities (top group: P-wave; bottom group: S-wave) vs. density at room temperature

Table 2.7: P-wave velocities at various pressures for samples in the Pindos and Vourinos ophiolite (Greece)

Density		Velocity (km/s) in pressures (MPa)													Pres. derivative		
(g/cm^3)	Direction	0	25	50	75	100	125	150	175	200	225	250	275	300	$(Vp)_0$	$\frac{dV_p}{d_P}(10^{-4})$	R^2
P 03-1	Z	6	6.19	6.27	6.33	6.36	6.39	6.4	6.42	6.43	6.45	6.46	6.47	6.48	6.27	7	0.93
	Y	6.35	6.75	6.83	6.87	6.91	6.94	6.95	6.97	6.97	6.99	7.01	7.01	7.05	6.83	7	0.95
3.19	Ave. Vp	6.18	6.47	6.55	6.6	6.64	6.67	6.68	6.7	6.7	6.72	6.74	6.74	6.77	6.55	7	0.94
	A %	5.67	8.66	8.55	8.18	8.29	8.25	8.24	8.22	8.06	8.04	8.17	8.01	8.43			
P 04-2	Z	5.12	5.65	5.68	5.7	5.72	5.74	5.77	5.78	5.8	5.81	5.84	5.85	5.87	5.65	7	0.99
	Y	5.91	5.96	6	6.04	6.07	6.08	6.11	6.12	6.15	6.16	6.17	6.2	6.21	5.99	7	0.99
2.87	Ave. Vp	5.52	5.81	5.84	5.87	5.9	5.91	5.94	5.95	5.98	5.99	6.01	6.03	6.04	5.82	7	0.99
	A %	14.3	5.34	5.48	5.79	5.94	5.75	5.72	5.71	5.86	5.85	5.5	5.81	5.63			
P 08-3	Z	5.94	6.08	6.12	6.14	6.17	6.18	6.2	6.21	6.23	6.24	6.27	6.28	6.29	6.1	6	0.99
	Y	6.23	6.3	6.36	6.4	6.44	6.49	6.51	6.52	6.55	6.56	6.57	6.58	6.58	6.38	8	0.91
3.06	Ave. Vp	6.09	6.19	6.24	6.27	6.31	6.34	6.36	6.37	6.39	6.4	6.42	6.43	6.44	6.24	7	0.95
	A %	4.77	3.55	3.85	4.15	4.28	4.89	4.88	4.87	5.01	5	4.67	4.67	4.51			
P 08-4 (3.08)	Z	6.25	6.33	6.38	6.41	6.43	6.45	6.46	6.48	6.49	6.51	6.52	6.53	6.54	6.37	6	0.99
P 11-1	Z	7.27	7.34	7.37	7.39	7.39	7.41	7.43	7.44	7.45	7.46	7.47	7.48	7.49	7.35	5	0.98
	Y	6.98	7.39	7.46	7.48	7.5	7.52	7.53	7.55	7.57	7.58	7.58	7.6	7.63	7.44	6	0.99
3.28	Ave. Vp	7.13	7.37	7.42	7.44	7.45	7.47	7.48	7.5	7.51	7.52	7.53	7.54	7.56	7.4	5.5	0.99
	A %	4.1	0.68	1.21	1.21	1.48	1.47	1.34	1.47	1.6	1.6	1.46	1.59	1.85			
P 12-1	Z	6.11	6.4	6.47	6.58	6.61	6.61	6.62	6.7	6.78	6.77	6.77	6.77	6.77	6.51	1	0.84
	Y	6.8	7.36	7.41	7.43	7.5	7.53	7.55	7.56	7.57	7.58	7.6	7.61	7.62	7.24	7	0.89
3.25	Ave. Vp	6.46	6.88	6.94	7.01	7.06	7.07	7.09	7.13	7.18	7.18	7.19	7.19	7.2	6.88	4	0.87
	A %	10.7	14	13.5	12.1	12.6	13	13.1	12.1	11	11.3	11.6	11.7	11.8			
P 13-1	Z	4.85	5.04	5.07	5.13	5.16	5.2	5.23	5.24	5.27	5.28	5.29	5.29	5.29	5.1	7	0.91
	Y	4.93	5.15	5.2	5.23	5.26	5.28	5.31	5.34	5.36	5.38	5.41	5.44	5.45	4.16	1	0.99
2.6	Ave. Vp	4.89	5.1	5.14	5.18	5.21	5.24	5.27	5.29	5.32	5.33	5.35	5.37	5.37	4.63	4	0.95
	A %	1.64	2.16	2.53	1.93	1.92	1.53	1.52	1.89	1.69	1.88	2.24	2.8	2.98			
P 13-2	Z	5.45	5.53	5.56	5.57	5.58	5.6	5.62	5.63	5.63	5.65	5.65	5.67	5.68	5.54	5	0.99
	Y	5.33	5.48	5.54	5.57	5.6	5.62	5.64	5.66	5.67	5.69	5.7	5.71	5.72	5.54	6	0.98
2.6	Ave. Vp	5.39	5.51	5.55	5.57	5.59	5.61	5.63	5.65	5.65	5.67	5.68	5.69	5.7	5.54	5.5	0.99
	A %	2.2	0.9	0.4	0	0.36	0.36	0.36	0.53	0.71	0.71	0.88	0.7	0.7			
P 16-3	Z	5.71	5.84	5.91	5.94	5.97	5.99	6	6.02	6.03	6.05	6.06	6.07	6.08	5.91	6	0.99
	Y	5.87	5.96	6	6.05	6.07	6.1	6.14	6.16	6.17	6.19	6.2	6.22	6.23	6	8	0.96
2.82	Ave. Vp	5.79	5.9	5.96	6	6.02	6.05	6.07	6.09	6.1	6.12	6.13	6.15	6.16	5.96	7	0.98
	A %	2.76	2.03	1.51	1.83	1.66	1.82	2.31	2.3	2.3	2.29	2.28	2.44	2.44			
V 03-11 (2.99)	Z	5.46	5.52	5.56	5.59	5.62	5.65	5.67	5.7	5.72	5.74	5.75	5.77	5.8	5.53	9	0.99
V 03-7 (2.95)	Z	5.31	5.4	5.43	5.45	5.47	5.49	5.51	5.52	5.54	5.55	5.58	5.6	5.62	5.39	7	0.99

Table 2.8: S-wave velocities at various pressures for samples in the Pindos and Vourinos ophiolite (Greece)

Density		Velocity (km/s) in pressures (MPa)													Pres. derivative		
(g/cm^3)	Direction	0	25	50	75	100	125	150	175	200	225	250	275	300	$(Vs)_0$	$\frac{dV_s}{d_P}(10^{-4})$	R^2
P 03-1	ZX	4.1	4.18	4.2	4.21	4.22	4.22	4.23	4.23	4.24	4.24	4.24	4.25	4.25	4.19	2	0.99
	ZY	3.65	3.82	3.88	3.91	3.92	3.93	3.94	3.95	3.95	3.96	3.96	3.97	3.97	3.91	3	0.94
3.19	$\triangle Vs(Z)$	0.45	0.36	0.32	0.3	0.3	0.29	0.29	0.28	0.29	0.28	0.28	0.28	0.28	0.28		
	YX	3.15	3.44	3.45	3.46	3.47	3.48	3.49	3.49	3.5	3.5	3.51	3.52	3.52	3.45	3	0.98
	YZ	3.27	3.86	3.91	3.93	3.94	3.95	3.96	3.97	3.98	3.98	3.99	3.98	4	3.91	3	0.94
	$\triangle Vs(Y)$	0.12	0.42	0.46	0.47	0.47	0.47	0.47	0.48	0.48	0.48	0.48	0.46	0.48	0.46		
	Ave. Vs	3.36	3.71	3.75	3.77	3.78	3.79	3.8	3.8	3.81	3.81	3.82	3.82	3.83	3.76	3	0.95
	A %	3.57	11.3	12.3	12.5	12.4	12.4	12.4	12.6	12.6	12.6	12.6	12	12.5	12.2		
P 04-2	ZX	3.11	3.16	3.17	3.19	3.19	3.2	3.21	3.22	3.23	3.23	3.24	3.25	3.25	3.17	3	0.99
	ZY	2.96	3.04	3.06	3.07	3.08	3.08	3.09	3.09	3.1	3.1	3.1	3.11	3.11	3.06	2	0.99
2.87	$\triangle Vs(Z)$	0.15	0.12	0.11	0.12	0.11	0.12	0.12	0.13	0.13	0.13	0.14	0.14	0.14	0.11		
	YX	2.94	3.09	3.11	3.12	3.13	3.14	3.14	3.15	3.15	3.16	3.16	3.17	3.17	3.1	2	0.99
	YZ	2.46	2.86	2.89	2.9	2.91	2.91	2.92	2.92	2.93	2.93	2.93	2.94	2.94	2.89	2	0.98
	$\triangle Vs(Y)$	0.48	0.23	0.22	0.22	0.22	0.23	0.22	0.23	0.22	0.23	0.23	0.23	0.23	0.21		
	Ave. Vs	2.87	3.04	3.06	3.07	3.08	3.08	3.09	3.1	3.1	3.11	3.11	3.12	3.12	3.06	2.25	0.99
	A %	22.7	9.88	9.16	9.45	9.1	9.41	9.39	9.69	9.67	9.66	9.98	9.94	9.94	9.17		
P 08-3	ZX	3.19	3.25	3.27	3.29	3.3	3.31	3.32	3.33	3.34	3.34	3.35	3.36	3.38	3.26	4	0.98
	ZY	3.4	3.47	3.49	3.51	3.52	3.53	3.54	3.55	3.56	3.57	3.57	3.58	3.58	3.5	3	0.98
3.06	$\triangle Vs(Z)$	0.21	0.22	0.22	0.22	0.22	0.22	0.22	0.22	0.22	0.23	0.22	0.22	0.2	0.24		
	YX	3.45	3.54	3.58	3.59	3.6	3.61	3.62	3.62	3.63	3.64	3.64	3.65	3.66	3.57	3	0.99
	YZ	3.32	3.39	3.41	3.42	3.43	3.44	3.44	3.45	3.46	3.46	3.47	3.48	3.48	3.4	3	0.99
	$\triangle Vs(Y)$	0.13	0.15	0.17	0.17	0.17	0.17	0.18	0.17	0.17	0.18	0.17	0.17	0.18	0.17		
	Ave. Vs	3.34	3.41	3.44	3.45	3.46	3.47	3.48	3.49	3.5	3.5	3.51	3.52	3.53	3.43	3.25	0.99
	A %	7.78	8.5	9.02	8.69	8.66	8.64	8.62	8.32	8.29	8.57	8.27	8.24	7.94	9.03		
P 08-4	ZX	3.51	3.59	3.61	3.62	3.63	3.64	3.64	3.65	3.66	3.67	3.68	3.68	3.69	3.6	3	0.99
	ZY	3.38	3.43	3.45	3.46	3.47	3.47	3.48	3.49	3.5	3.5	3.51	3.51	3.51	3.44	2	0.99
3.08	$\triangle Vs(Z)$	0.13	0.16	0.16	0.16	0.16	0.17	0.16	0.16	0.16	0.17	0.17	0.17	0.18	0.16		
	Ave. Vs	3.45	3.51	3.53	3.54	3.55	3.56	3.56	3.57	3.58	3.59	3.6	3.6	3.6	3.52	2.5	0.99
P 11-1	ZX	4.15	4.22	4.25	4.27	4.28	4.28	4.28	4.29	4.29	4.29	4.3	4.3	4.3	4.26	1	4.15
	ZY	4.22	4.36	4.39	4.41	4.41	4.42	4.42	4.43	4.43	4.44	4.44	4.44	4.45	4.39	2	4.22
3.28	$\triangle Vs(Z)$	0.07	0.14	0.14	0.14	0.13	0.14	0.14	0.14	0.14	0.15	0.14	0.14	0.15	0.13		
	YX	4.16	4.43	4.48	4.51	4.52	4.53	4.54	4.54	4.55	4.55	4.56	4.57	4.57	4.49	3	0.99
	YZ	4	4.09	4.11	4.13	4.14	4.14	4.17	4.19	4.2	4.22	4.23	4.23	4.25	4.09	6	0.98
	$\triangle Vs(Y)$	0.16	0.34	0.37	0.38	0.38	0.39	0.37	0.35	0.35	0.33	0.33	0.34	0.32	0.4		
	Ave. Vs	4.13	4.28	4.31	4.33	4.34	4.34	4.35	4.36	4.37	4.38	4.38	4.39	4.39	4.31	3	0.99
	A %	3.87	7.95	8.59	8.78	8.76	8.98	8.5	8.02	8.01	7.54	7.53	7.75	7.29	9.29		

Cont' Table 2.8

Density		Velocity (km/s) in pressures (MPa)													Pres. derivative		
(g/cm^3)	Direction	0	25	50	75	100	125	150	175	200	225	250	275	300	$(Vs)_0$	$\frac{dVs}{d_P}(10^{-4})$	R^2
P 12-1	ZX	3.4	3.81	3.88	3.91	3.93	3.95	3.96	3.97	3.98	3.99	3.99	4	4.01	3.9	4	0.96
	ZY	3.56	3.86	3.93	3.96	3.99	4.01	4.02	4.03	4.04	4.07	4.08	4.09	4.1	3.92	6	0.98
3.25	$\triangle Vs(Z)$	0.16	0.05	0.05	0.05	0.06	0.06	0.06	0.06	0.06	0.08	0.09	0.09	0.09	0.02		
	YX	3.94	4.11	4.15	4.16	4.17	4.18	4.19	4.2	4.21	4.23	4.24	4.25	4.25	4.13	4	0.98
	YZ	3.96	4.12	4.18	4.2	4.21	4.23	4.23	4.24	4.25	4.25	4.26	4.26	4.27	4.18	3	0.97
	$\triangle Vs(Y)$	0.02	0.01	0.03	0.04	0.04	0.05	0.04	0.04	0.04	0.02	0.02	0.01	0.02	0.05		
	Ave. Vs	3.72	3.98	4.04	4.06	4.08	4.09	4.1	4.11	4.12	4.14	4.14	4.15	4.16	4.03	4.25	0.97
	A %	15.1	7.8	7.43	7.15	6.87	6.84	6.59	6.57	6.55	6.29	6.52	6.27	6.25	6.94		
P 13-1	ZX	2.54	2.63	2.65	2.66	2.67	2.68	2.68	2.69	2.69	2.7	2.71	2.71	2.72	2.65	2	0.99
	ZY	2.57	2.67	2.7	2.71	2.72	2.72	2.73	2.74	2.74	2.75	2.75	2.75	2.76	2.7	2	0.98
2.6	$\triangle Vs(Z)$	0.03	0.04	0.05	0.05	0.05	0.04	0.05	0.05	0.05	0.05	0.04	0.04	0.04	0.05		
	YX	2.72	2.83	2.84	2.86	2.87	2.87	2.88	2.88	2.89	2.89	2.89	2.9	2.89	2.85	2	0.95
	YZ	2.74	2.8	2.82	2.82	2.83	2.84	2.85	2.86	2.87	2.87	2.88	2.88	2.89	2.81	3	0.97
	$\triangle Vs(Y)$	0.02	0.03	0.02	0.04	0.04	0.03	0.03	0.02	0.02	0.02	0.01	0.02	0	0.04		
	Ave. Vs	2.64	2.73	2.75	2.76	2.77	2.78	2.79	2.79	2.8	2.8	2.81	2.81	2.82	2.75	2	0.99
	A %	6.81	7.32	6.9	7.24	7.21	6.84	7.18	6.8	7.15	6.78	6.41	6.76	6.04	7.27		
P 13-2	ZX	2.69	2.77	2.79	2.8	2.8	2.81	2.81	2.82	2.82	2.82	2.83	2.83	2.83	2.71	2	0.99
	ZY	2.5	2.55	2.58	2.59	2.6	2.6	2.61	2.61	2.62	2.62	2.63	2.63	2.63	2.58	2	0.99
2.6	$\triangle Vs(Z)$	0.19	0.22	0.21	0.21	0.2	0.21	0.2	0.21	0.2	0.2	0.2	0.2	0.2	0.13		
	YX	2.72	2.78	2.79	2.8	2.81	2.81	2.82	2.83	2.83	2.84	2.84	2.84	2.85	2.71	2	0.99
	YZ	2.7	2.73	2.74	2.75	2.76	2.76	2.77	2.77	2.77	2.78	2.78	2.78	2.79	2.74	2	0.99
	$\triangle Vs(Y)$	0.02	0.05	0.05	0.05	0.05	0.05	0.05	0.06	0.06	0.06	0.06	0.06	0.06	0.03		
	Ave. Vs	2.65	2.71	2.73	2.74	2.74	2.75	2.75	2.76	2.76	2.77	2.77	2.77	2.78	2.69	2	0.99
	A %	8.29	8.49	7.71	7.68	7.66	7.65	7.63	7.98	7.61	7.96	7.58	7.58	7.93	4.84		
P 16-3	ZX	3.02	3.08	3.09	3.08	3.09	3.1	3.1	3.11	3.11	3.11	3.11	3.12	3.12	3.07	2	0.96
	ZY	2.92	2.99	2.98	2.99	3	3	3.01	3.02	3.02	3.02	3.03	3.03	3.04	2.99	2	0.94
2.82	$\triangle Vs(Z)$	0.02	0.09	0.11	0.09	0.09	0.1	0.09	0.09	0.09	0.09	0.08	0.09	0.08	0.08		
	YX	2.85	2.95	2.99	3.01	3.02	3.03	3.04	3.04	3.04	3.05	3.05	3.06	3.06	2.98	2	0.99
	YZ	3.04	3.12	3.14	3.15	3.16	3.16	3.17	3.17	3.17	3.18	3.18	3.19	3.19	3.14	2	0.95
	$\triangle Vs(Y)$	0.19	0.17	0.15	0.14	0.14	0.13	0.13	0.13	0.13	0.13	0.13	0.13	0.13	0.16		
	Ave. Vs	2.96	3.04	3.05	3.06	3.07	3.07	3.08	3.09	3.09	3.09	3.09	3.1	3.1	3.05	2	0.97
	A %	4.06	4.28	5.25	5.23	5.22	5.21	5.19	4.86	4.86	5.18	4.85	5.16	4.83	4.93		
V 03-11	ZX	3.21	3.26	3.28	3.29	3.32	3.32	3.33	3.34	3.34	3.35	3.35	3.37	3.38	3.28	3	0.95
	ZY	3.18	3.23	3.25	3.26	3.27	3.27	3.28	3.29	3.3	3.3	3.31	3.32	3.32	3.24	3	0.99
2.99	$\triangle Vs(Z)$	0.03	0.03	0.03	0.03	0.05	0.05	0.05	0.05	0.04	0.05	0.04	0.05	0.06	0.04		
	Ave. Vs	3.2	3.25	3.27	3.28	3.3	3.3	3.31	3.32	3.32	3.33	3.33	3.35	3.35	3.26	3	0.97
V 03-7	ZX	2.91	3	3.02	3.03	3.03	3.04	3.04	3.04	3.05	3.05	3.06	3.06	3.08	3	2	0.93
	ZY	3.08	3.13	3.14	3.16	3.17	3.17	3.18	3.18	3.19	3.19	3.2	3.21	3.21	3.14	2	0.99
2.95	$\triangle Vs(Z)$	0.17	0.13	0.12	0.13	0.14	0.13	0.14	0.14	0.14	0.14	0.14	0.15	0.13	0.14		
	Ave. Vs	3	3.07	3.08	3.1	3.1	3.11	3.11	3.11	3.12	3.12	3.13	3.14	3.15	3.07	2	0.96

Table 2.9: Poisson's and Vp / Vs ratio at 200 MPa

Sample	Density (g/cm^3)	$Vs_{(mean)}$ (km/s)	$Vp_{(mean)}$ (km/s)	Poisson's Ratio	Vp/Vs Ratio	Serpentinization (%)
P03-1	3.19	3.81	6.7	0.26	1.76	13.6
P04-2	2.87	3.1	5.98	0.32	1.93	53.8
P08-3	3.06	3.5	6.39	0.29	1.83	30.4
P11-1	3.28	4.37	7.51	0.24	1.72	2.3
P12-1	3.25	4.12	7.18	0.25	1.74	6.8
P13-1	2.6	2.8	5.32	0.31	1.9	87.9
P13-2	2.6	2.76	5.65	0.34	2.05	87.9
P16-3	2.82	3.09	6.1	0.33	1.97	59.9
V03-11	2.99	3.4	5.72	0.23	1.68	38.8
V03-7	2.95	3.12	5.54	0.27	1.78	43.8
P08-4	3.08	3.58	6.49	0.28	1.81	27.5

Table 2.10: Calculated elastic stiffnesses (GPa) for samples in the Pindos and Vourinos ophiolite (Greece) at 300 MPa

Propagation	XX	YY	ZZ	ZY or YZ	ZX or XZ	XY or YX	Elastic	Ave. density
Sample	C_{11}	C_{22}	C_{33}	C_{44}	C_{55}	C_{66}	Symmetry	(g/cm^3)
P 03-1	-	155	132	50	57	39	ORTHO	3.19
P 04-2	-	109	97	26	30	28	ORTHO	2.87
P 08-3	-	131	119	38	34	40	ORTHO	3.06
P 11-1	-	188	182	61	60	67	quasi-IO	3.28
P 12-1	-	186	149	56	51	58	ORTHO	3.25
P 13-1	-	75	72	21	19	22	quasi-IO	2.6
P 13-2	-	84	82	19	21	21	quasi-IO	2.6
P 16-3	-	107	103	27	27	26	quasi-IO	2.82
P 08-4	-	-	130	38	41	-	-	3.08
V 03-7	-	-	91	30	27	-	-	2.95
V 03-11	-	-	98	33	33	-	-	2.99
Forsterite	328	200	235	66.7	81.3	80.9	ORTHO	3.22

Noted: C_{44}, C_{55}, and C_{66} calculated by average velocities; Assumed C_{11} to agree with symmetry

Table 2.11: Parameters of velocity anisotropy at 300 MPa

Sample	β(%)	Density (g/cm^3)	Vp (Km/s)	Ap (%)	Vs (Km/s)	As (%)	$\triangle$ Vs (km/s)
P03-1	13.6	3.19	6.7	8.06	3.81	12.6	0.39
P04-2	53.8	2.87	5.98	5.86	3.1	9.67	0.18
P08-3	30.4	3.06	6.39	5.01	3.5	8.29	0.2
P11-1	2.3	3.28	7.51	1.6	4.37	8.01	0.25
P12-1	6.8	3.25	7.18	11	4.12	6.55	0.05
P13-1	87.9	2.6	5.32	1.69	2.8	7.15	0.04
P13-2	87.8	2.6	5.65	0.71	2.76	7.61	0.13
P16-3	59.9	2.82	6.11	2.3	3.09	4.86	0.11
P 08-4	27.5	3.08	6.49		3.58		0.16
V 03-7	43.8	2.95	5.54		3.12		0.14
V 03-11	38.8	2.99	5.72		3.32		0.04

Density, Serpentine ratio β, Average Ultrasonic Velocities (Vp/Vs), Anisotropies (Ap/As), S-wave splitting

Chapter 3

Magnetic Susceptibility and AMS

3.1 Introduction

The dependence of magnetic properties on a preferred direction is called magnetic anisotropy. The variation of susceptibility with orientation is called Anisotropy of Magnetic Susceptibility (*Tarling and Hrouda*, 1993) or usually just AMS. The variation of susceptibility with orientation can be described mathematically in terms of a second-rank tensor and can be simply visualized as a susceptibility ellipsoid. Magnetic fabrics defined by anisotropy of magnetic susceptibility (AMS) are sensitive indicators of rock texture and strain. Magnetic fabric techniques use this characteristic to infer the petrofabric of rocks so that their origin and structural evolution can be determined. Consequently, AMS (usually, measured at low magnetic field and room temperature) is a useful tool for its intrinsic petrofabric meanings. The AMS measurement procedures principally include: at first, the collection of oriented rock samples; second, determination of the strength of the magnetization at a number of different orientations; and finally, analysis and illustration. AMS can be interpreted in terms of the net shape of the grains and the degree of their crystalline alignments, which, in turn, can be interpreted and compared to other petrofabric techniques such as Electron Back Scatter Diffraction (EBSD). Thus, it is theoretically reasonable to compare petrofabrics by magnetic anisotropy with those of other rock physical techniques such as elastic anisotropy as discussed in the previous chapter.

While the making AMS measurements is rather straightforward, their interpretation is not simple. It is essential to establish the compositions, sizes and physical relationships of mineral grains before attempting geological interpretations of magnetic fabrics.

Obviously, analysis of AMS plays a particular role in the studies of many branches of the earth science. For example, research of AMS in paleomagnetism revealed some interesting features related with strain in the last decades (*Borradaile*, 1988; *Rochette et al.*, 1992), and relationships between the grain shape, structural axes and magnetic axes help to understand and reconstruct the rock's framework.

A compound's magnetic susceptibility K is defined with $M = K \times H$, where M is the induced magnetization of the material and H is the inducing magnetic field. K is most often measured at room temperature and low-field strength (≤ 1 mT),*Rochette et al.* (1992). The principles and applications related to anisotropy of low field magnetic susceptibility reviewed by many authors (*Hrouda*, 1982; *Borradaile*, 1988; *Jackson*, 1991; *Borradaile and Henry*, 1997). The statistical process and treatment of AMS data from a set of specimens to define the mean AMS tensor was done by the tensorial mean method (*Jelinek*, 1978).

3.2 Theory and method of determining AMS

The study that AMS can be used for petrofabric and other branches of the earth science, on consequently comes from the contention that AMS is caused by intrinsic magnetic properties. At first, magnetic properties arise from the motion of electrically charged particles. All materials have magnetic properties at temperatures above absolute zero. Then, AMS arises the magnetic fabric caused by the preferred orientation of minerals. In general, the preferred orientation of crystallographic axes controls the grain shape and determines the magnitude and direction of AMS for most minerals and rocks. The bulk susceptibility and its anisotropy represent a summation of the susceptibility of all the mineral species that are present in a sample. What follows is a brief theoretical review related with magnetic anisotropy.

3.2.1 Classes of Magnetic Materials

When a magnetic field is applied to materials, the electron spins produce a magnetization opposite to the applied field. As mentioned earlier, all materials are magnetic in general. The difference is just that some materials are much more magnetic than others. The main reason is that in some materials there is no collective interaction of atomic magnetic

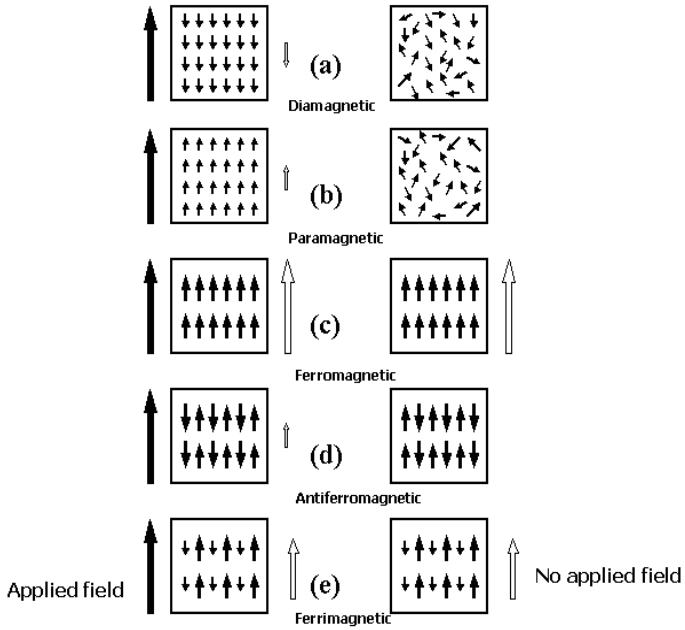

Figure 3.1: Different forms of magnetization (Modified from Tarling and Hrouda, 1993). Solid arrow: Applied magnetic field; Hollow arrow: Magnetization

moments, whereas in other materials there is a very strong interaction between atomic moments. So, usually the different types of magnetism is categorized by how these materials respond to magnetic fields. The magnetic behavior of materials can be classified into the following five major groups: Diamagnetism, Paramagnetism, Ferromagnetism, Ferrimagnetism, and Antiferromagnetism (Figure 3.1).

3.2.2 Domain Theory

The magnetic material is actually composed of small regions that called magnetic domains. In each domain the local magnetization is saturated but not necessarily parallel. Each domain is separated from its neighbor by a block wall. The phenomena that magnetization of ferrimagnetic materials can be greatly influenced by the application even a very low magnetic field comes from this truth. Although domains are small ($\sim 10^{-6} - \sim 10^{-4} m$), they are still much larger than atomic distances($\sim 10^{-10} m$). Without external applied field, the domains arrange themselves to minimize the magnetostatic energy associated with their surface poles. The magnetic behavior of a domain-sized

particle is significantly different from that of one containing multidomain-sized particles, even if the composition and total quantity of the ferromagnetic materials are the same.

The existence of domains is hinted at by the observation that some magnetic properties, and in particular, coercivity and remanence vary greatly with grain size. The magnetic behavior can be subdivided on the basis of grain size into four ranges: SPM: superparamagnetic; SD: single domain; PSD: Pseudo-single domain; and MD: multidomain (*Dunlop and Özdemir*, 1997).

If the grain is small, the magnetization within it is uniform in direction and is aligned with specific crystallographic axes. However, in large grains a number of volume elements are developed, each with its magnetization aligned along the 'easy' axes (*Tarling and Hrouda*, 1993).

3.2.3 Anisotropy of magnetic susceptibility

The dependence of magnetic properties on a preferred direction is called magnetic anisotropy. There are several different types of magnetic anisotropy:

- Magnetocrystalline Anisotropy
- Stress Anisotropy
- Shape Anisotropy

Magnetocrystalline anisotropy is an intrinsic property that arises from the action of lattice forces on the electron-spin configuration along a specific direction termed the easy plane or the easy axis. Stress Anisotropy is another effect related to spin-orbit coupling called magnetostriction. Magnetostriction arises from the strain dependence of the anisotropy constants. Shape anisotropy is due to the shape of a mineral grain. The surface charge distribution of the magnetic mineral is another source of a magnetic field. As noted earlier, this variation of susceptibility with orientation is called Anisotropy of magnetic susceptibility. In reality, only a few rocks have the induced magnetization of the same strength from a symmetrically shaped specimen irrespective of the direction in which a weak field is applied. Such rock samples are magnetically isotropic. In most rock samples the strength of the magnetization induced by a weak field of constant strength

depends on the orientation of the sample within the field. Such rocks are magnetically anisotropic. The variation of susceptibility with orientation can be described mathematically in terms of a second-rank tensor and can be simply visualized as a susceptibility ellipsoid (Figure 1.2). The anisotropy of magnetic susceptibility used in most published articles is usually determined from measurements of susceptibility in a weak field (≤ 1 mT) unless specifically stated.

The magnitude of the anisotropy depends on two factors: the anisotropy of the particles themselves and the degree of their alignment. It must be emphasized that no one method of measurement is capable of resolving the contributions of these two factors. Furthermore, the shape anisotropy of a ferrimagnetic grain can differ radically depending on whether it is multi- or single-domain because of the markedly different hysteresis loops of such domains. Thus, extreme care is needed when attempting to interpret any magnetic anisotropy in terms of some physical process.

3.2.4 Theory and method of determining AMS

The aim of a mathematical description is to give a physical concept of the values measured for magnetic susceptibility, to derive the fundamental possibilities of exterminating the anisotropy and evaluate their accuracy (*Janák*, 1965). The theory of calculation of AMS has been discussed in the past, and various authors described methods of calculating the susceptibility tensor using least squares techniques (*Granar*, 1958; *Girdler*, 1961; *Janák*, 1965; *Jelinek*, 1977; *Hanna*, 1977). Here is a general summary of their work in the past.

When a low field ($\leq$ 1mT) is applied to a magnetically anisotropic specimen, the magnetization, M, is not parallel to the applied field, H, and its three orthogonal components can be defined as:

$$\begin{aligned} M_1 &= K_{11}H_1 + K_{12}H_2 + K_{13}H_3 \\ M_2 &= K_{21}H_1 + K_{22}H_2 + K_{23}H_3 \\ M_3 &= K_{31}H_1 + K_{32}H_2 + K_{33}H_3 \end{aligned} \tag{3.1}$$

This is equivalent to:

$$M_i = K_{ij} H_j (i, j = 1, 2, 3) \tag{3.2}$$

Where K_{ij} is the second-order tensor. This can also be expressed as a symmetric matrix:

$$K_{ij} = \begin{pmatrix} K_{11} & K_{12} & K_{13} \\ K_{12} & K_{22} & K_{23} \\ K_{31} & K_{32} & K_{33} \end{pmatrix} \tag{3.3}$$

Of these parameters, $K_{12} = K_{21}$, $K_{23} = K_{32}$, $K_{31} = K_{13}$, so six independent components must be determined to completely define the susceptibility ellipsoid. If the material is magnetically isotropic, these off diagonal components are equal to zero.

The record value in the direction n of the external field with the measuring equipment is the projection of the vector of of the real susceptibility into the direction n(Figure 3.2(a)). When choosing the directions, the purpose is to keep the relation for the directional susceptibility simple , the chosen direction easily realizable, and the measurements accurate. A suitable system (Bartington 18-position) of measurement is shown in Figure 3.2(b). The anisotropy tensor contains 6 unknown coefficients and therefore a system of six independent measurements is enough for its determination. By multiplying the measured deviations (directional consine) by the corresponding calibration instrument constant, we can determine the values of the directional susceptibilities $\kappa_1 ... \kappa_9$.

After that, K_{ij} can be measured and calculated from the directional susceptibilities $\kappa_1 ... \kappa_9$. For instance, the value $\kappa_4, \kappa_5, \kappa_6$ for $K_{ij} (i \neq j)$:

$$\begin{pmatrix} K_{23} \\ K_{13} \\ K_{12} \end{pmatrix} = \begin{pmatrix} 0 & -1/2 & -1/2 & -1 & 0 & 0 \\ -1/2 & 0 & -1/2 & 0 & 1 & 0 \\ -1/2 & -1/2 & 0 & 0 & 0 & 1 \end{pmatrix} \begin{pmatrix} \kappa_1 \\ \kappa_2 \\ \kappa_3 \\ \kappa_4 \\ \kappa_5 \\ \kappa_6 \end{pmatrix} \tag{3.4}$$

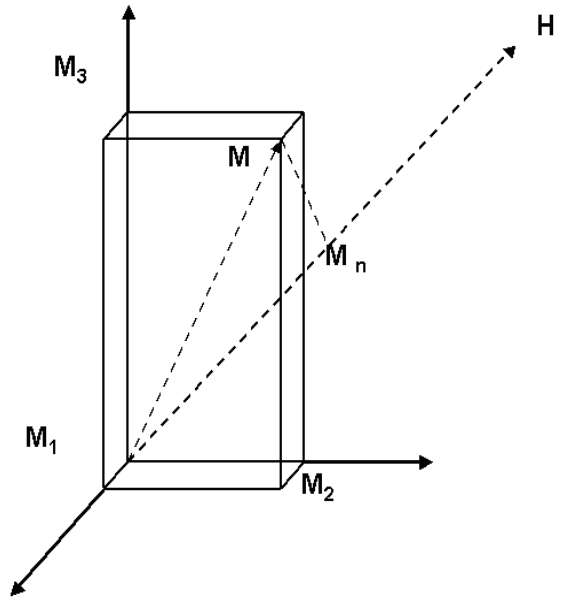

(a)

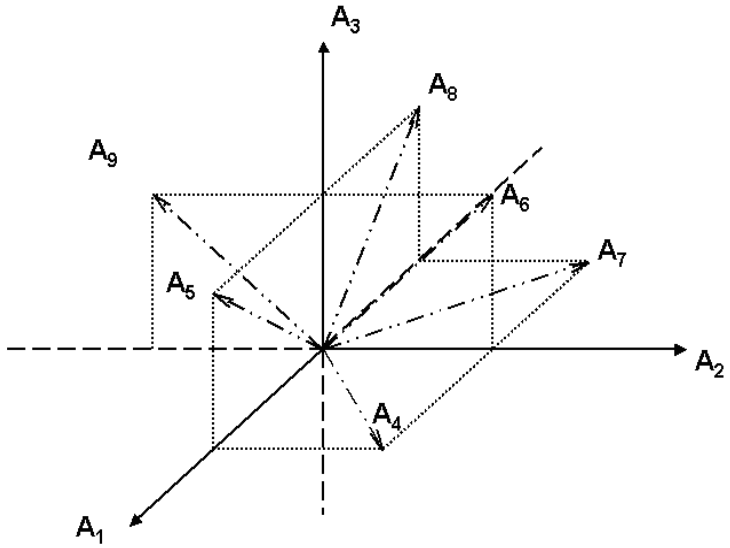

(b)

Figure 3.2: Top: Magnetic field H and Magnetization M; Bottom:Directions $A_1 ... A_9$ in AMS measurement (Modified from Girdler, 1961; Janák, 1965).

Similarly. use the values of $\kappa_7, \kappa_8, \kappa_9$ for $K_{ij}(i \neq j)$:

$$\begin{pmatrix} K_{23} \\ K_{13} \\ K_{12} \end{pmatrix} = \begin{pmatrix} 0 & 1/2 & 1/2 & -1 & 0 & 0 \\ 1/2 & 0 & 1/2 & 0 & -1 & 0 \\ 1/2 & 1/2 & 0 & 0 & 0 & -1 \end{pmatrix} \begin{pmatrix} \kappa_1 \\ \kappa_2 \\ \kappa_3 \\ \kappa_7 \\ \kappa_8 \\ \kappa_9 \end{pmatrix} \tag{3.5}$$

By using least square solution, it is possible obtain an estimate for the best fit of the susceptibility-ellipsoid and hence for the magnitudes and directions of the principal axes. The final equation giving the six coefficients K_{ij} is:

$$\begin{pmatrix} K_{11} \\ K_{22} \\ K_{33} \\ K_{23} \\ K_{31} \\ K_{12} \end{pmatrix} = \frac{1}{18} \begin{pmatrix} 10 & -2 & -2 & 4 & 4 & -2 & 4 & 4 & 2 \\ -2 & 10 & -2 & 4 & -2 & 4 & 4 & -2 & 4 \\ -2 & -2 & 10 & -2 & 4 & 4 & -2 & 4 & 4 \\ 0 & 0 & 0 & 0 & 0 & 9 & 0 & 0 & -9 \\ 0 & 0 & 0 & 0 & 9 & 0 & 0 & -9 & 0 \\ 0 & 0 & 0 & 9 & 0 & 0 & -9 & 0 & 0 \end{pmatrix} \begin{pmatrix} \kappa_1 \\ \kappa_2 \\ \kappa_3 \\ \kappa_4 \\ \kappa_5 \\ \kappa_6 \\ \kappa_7 \\ \kappa_8 \\ \kappa_9 \end{pmatrix} \tag{3.6}$$

The directions of principal axes can be calculated by:

$$\tan\theta = \frac{n_2}{n_1} \tag{3.7}$$

$$\sin\phi = n_3 \tag{3.8}$$

Where n_i are the directional cosines of the principal axis, then, the direction cosines are converted to the (θ, ϕ) notation where θ is the angle of declination in degrees measured clockwise from OA_1 and ϕ is the angle of inclination with reference to the $A_1 - A_2$ plane. According to *Janák* (1965), the average deviation of such coefficients is less than 1 %.

3.3 Magnetic susceptibility measurement

There are different methods that can to be used measure magnetic anisotropy. Each method provides information that enable the anisotropy of magnetic susceptibility to be described in terms of a triaxial ellipsoid. *Jelinek* (1977) used the 15-position scheme. *Borradaile and Stupavsky* (1995) generally summarized and reviewed measurement schemes. In our lab, AMS measurement uses the 18-position system of Bartington MS2B sensor with AMSWIN- BAR software.

3.3.1 Sample preparation

The sampling method for AMS is the same as those used to collect oriented rock for paleomagnetic purposes (*Cox and Doell*, 1960; *Collison*, 1983; *Tarling*, 1983; *Tarling and Hrouda*, 1993). All such methods compromise between (i) the need for speed and accuracy during orientation and collection under field conditions and (ii) the size and shape of specimens required for the different instruments. Most of the instruments used to measure anisotropy are designed for specimens of specific sizes and shapes, these are usually identical to those required for the measurement of paleomagnetic properties (*Collison*, 1983; *Tarling*, 1983). Cylinders and cubes are normally used. The two most common standard shapes are cylinders with a diameter of 2.5 cm and a height of 2.1 cm and cubes of 2.0 cm per side (Figure 3.3). In this study, we use 2.54 cm (1-inch) length $\times$ 2.54 cm diameter core required by the operation manual from Bartington. After the velocity anisotropy measurements, the same cores were shortened and flattened as 2.54 cm diameter $\times$ 2.54 cm length cylinder core for AMS measurement.

The frequency dependence of susceptibility should be considered during the AMS measurement. Changing frequency means changing the time of reaction of grains in applied field. That is, the domain sizes will shift to smaller or bigger volumes based on

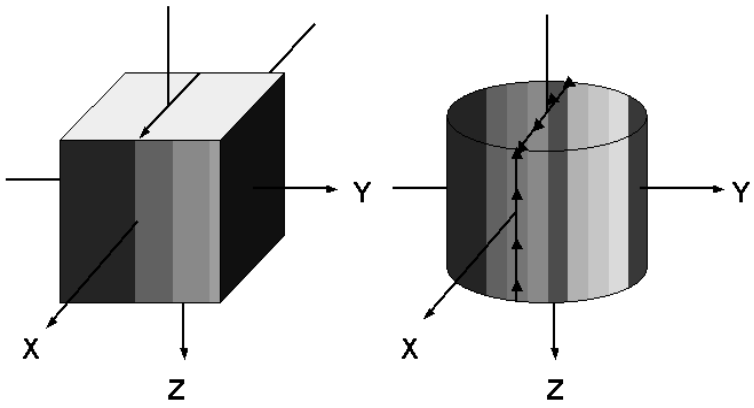

Figure 3.3: Standard specimens for AMS measurement

variance of frequency. Experimental results show that more grains become blocked when the frequency of measurement increases. The decrease percentage in initial susceptibility per decade of frequency is: 1-20% for SPM grains; $< 1\%$ for SD and MD grains (*Dunlop and Özdemir*, 1997). In this study, the AMS was measured on a Bartington MS2B Sensor in conjunction with the AMSWIN-BAR software, operating at a fixed frequency of 0.465 kHz (LF), with an applied field of 250 μT. The three principal axes defining the AMS ellipsoid are determined from the 18-position orientation scheme.

3.3.2 AMS calculation and illustration

A wide range of parameters have been used in the literature about the applications of AMS to both magnetic properties and petrofabrics. This short introduction is intended to provide explanations for the parameters used in this study.

The anisotropy of low-field magnetic susceptibility (AMS) is usually determined after measuring the susceptibility of a rock specimen along different directions. This enables one to calculate the AMS tensor, which can be represented by an ellipsoid with minimum (K_3), intermediate (K_2) and maximum (K_1) susceptibility axes: $K_1 \geq K_2 \geq K_3$.

The mean susceptibility is represented by: K = (K1 + K2 + K3)/3.

The ratios of the pairs of the principal susceptibilities are commonly used to characterize the magnetic fabric. Numerous parameters have been defined both for the quantification of the magnitude of anisotropy and for defining the shape of the ellipsoid. The parameters can usually be divided into two main groups - those dealing with the magnitude and shape of the susceptibility ellipsoid and those concerned with the spatial orientation of the principal axes of the ellipsoid.

The anisotropy degree parameter for the magnitude of anisotropy is particularly sensitive to variation in the total susceptibility, which is defined on the ratio of the maximum and minimum susceptibilities (*Nagata*, 1961):

$$P = K_1/K_3$$

Owens (1974) proposed another parameter for magnitude of anisotropy - the normalized anisotropy degree:

$$S = (K_1 - K_3)/K_{mean}$$

Currently, the rock-magnetic literature strongly recommend that the corrected anisotropy degree should be adopted. It was proposed by *Jelinek* (1981), :

$$P_J = exp\sqrt{\{2[(\eta_1 - \eta_m)^2 + (\eta_2 - \eta_m)^2 + (\eta_3 - \eta_m)^2]\}}$$

Where $\eta_1 = lnK_1; \eta_2 = lnK_2; \eta_3 = lnK_3; \eta_m = (\eta_1 + \eta_2 + \eta_3)/3$. The parameter P_J incorporates both the intermediate and mean susceptibility rather than just the maximum and minimum values, thus, it is a more informative parameter than P alone. Also, It is better to expresses the magnetic property by logarithmic values of susceptibility.

The shape of the anisotropy ellipsoid can be expressed in terms of the ratios or differences of the axial values. Most early parameters were based on ratios.

For example, here is lineation (*Balsey and Buddington*, 1960):

$$P_1 = L = K_1/K_2$$

and foliation (*Stacey*, 1960):

$$P_3 = F = K_2/K_3$$

T, the parameter for the shape ellipsoid combines lineation and foliation parameters, which includes all three principal susceptibilities in its calculation. The magnetic literatures recommended that this shape parameter should be adopted (*Jelinek*, 1981; *Hrouda*, 1982). T can be expressed as:

$$T = \left[\frac{2ln(K_2/K_3)}{ln(K_1/K_3)}\right] - 1$$

$0 < T \leq 1$ corresponds to oblate (disk) shapes ; $-1 \leq T < 0$ corresponds to prolate (rod) shapes; $T = 0$ corresponds to the shape of neutral (plane-strain) ellipsoid ($P_J = P$).

3.4 Results and discussion

An AMS measurement principally involves the field acquistion of an oriented rock sample followed by determination of its magnetization in different directions with known orientation. As noted, this is measured in 18 different directions in our procedure. Then, all differences can be analyzed and illustrated. AMS can be fundamentally interpreted in terms of the net shape of the grains of major phase and the degree of their crystalline alignments by its intrinsic petrofabric meaning, which, in turn, can be compared and interpreted in the same way as in all other petrofabric techniques. AMS results for the 8 samples from the Pindos and Vourinos Ophiolite are presented in Table 3.1. All reported values of magnetic susceptibility were measured at low field and room temperature. The values observed here are consistent with the wide range of susceptibilities from3.1 $\times 10^{-3}$ to 18 $\times 10^{-3}$ SI (*Blum*, 1997) on serpentines.

The mean magnetic susceptibility, $K_m = (K_1 + K_2 + K_3)/3$, varies from 50.9 $\times 10^{-5}$ to 444.8 $\times 10^{-5}$ SI in the samples from the Pindos and Vourinos Ophiolite with an overall mean magnetic susceptibility of 221.7$\times 10^{-5}$ SI. The highest value is obtained from P 16-3, the serpentinized dunite, due to the presence of abundant magnetite by serpentinization of rock. Therefore, the magnetic fabrics mainly are produceed by magnetite grains. The lowest value comes from the P 12-1, the dunite, and is primarily due to the paramagnetic mineral olivine. These values do not significantly depart from the data published by *Toft et al.* (1990). Hence, in the samples from the Pindos and Vourinos Ophiolite, contribution from both the paramagnetic and ferrimagnetic minerals has to be taken into account when magnetite is present from the process of serpentinization.

Table 3.1: The AMS measurement Data at room temperature and low field for samples in the Pindos and Vourinos ophiolite (Greece)

Sample		Declination $(degree)$	Inclination $(degree)$	Eigenvalue $(degree)$	Susceptibility $(mean, 10^{-5}SI)$	Anisotropy (%)	Serpentinization β (%)
P 03-1	K_{min}	3.4	83.2	90.2	101.9	18.9	13.6
	K_{int}	222.1	5.3	106.1			
	K_{max}	131.7	4.2	109.5			
P 08-3	K_{min}	307	50.9	291.3	302.3	7	30.4
	K_{int}	115.3	38.5	303			
	K_{max}	209.9	5.8	312.6			
P 13-1	K_{min}	4.3	64.3	291.1	317.8	15.1	87.9
	K_{int}	223	20.6	323.2			
	K_{max}	127.4	14.7	339.1			
P 13-2	K_{min}	51.4	69	307.5	330.7	14.8	87.9
	K_{int}	215.3	20.3	328.1			
	K_{max}	307.3	5.4	356.5			
P 11-1	K_{min}	6.1	81.1	117.2	126.1	13.9	2.3
	K_{int}	96.2	0	126.3			
	K_{max}	186	8.9	134.7			
P 04-2	K_{min}	126.6	86.1	92.4	99	10.9	53.8
	K_{int}	16.5	1.3	101.5			
	K_{max}	286.5	3.7	103.2			
P 16-3	K_{min}	212.4	58.8	29.8	444.8	219.2	59.9
	K_{int}	82.2	21.3	299.8			
	K_{max}	343.3	21.6	1004.7			

In principal, the magnetic anisotropy will be greatly influenced by the samples' composition. In the samples from Pindos and Vourinos Ophiolite, the smallest value of AMS $((K_1 - K_3)/K_{mean})$ is 13.7% (P 12-1) among all dunite samples, while the values of AMS of samples P 08-3 and P 04-2 are 7% and 10.9%, respectively. The reason for this difference may be related to the differing composition of the protoliths with the P 08-3 and P 04-2 being serpentinized harzburgites; while the others are from dunite. The largest AMS value comes from P16-3 at 219.2%. Its average magnetic susceptibility is 444.8 $\times 10^{-5}$ SI, which definitely implies the existence of ferromagnetic minerals.

The magnitude and direction of all the samples' principal axes are shown in Figure 3.4. The maximum and intermediate axes have no special declination trend as there is no orientation with their original geographic position. Their inclination, however, is mostly near the edge of the polar plot. This further suggests that the orientation of the sampling was closely perpendicular to foliation. The minimum K axis shows the non-random distribution with its direction clustering in the direction perpendicular to textural planes

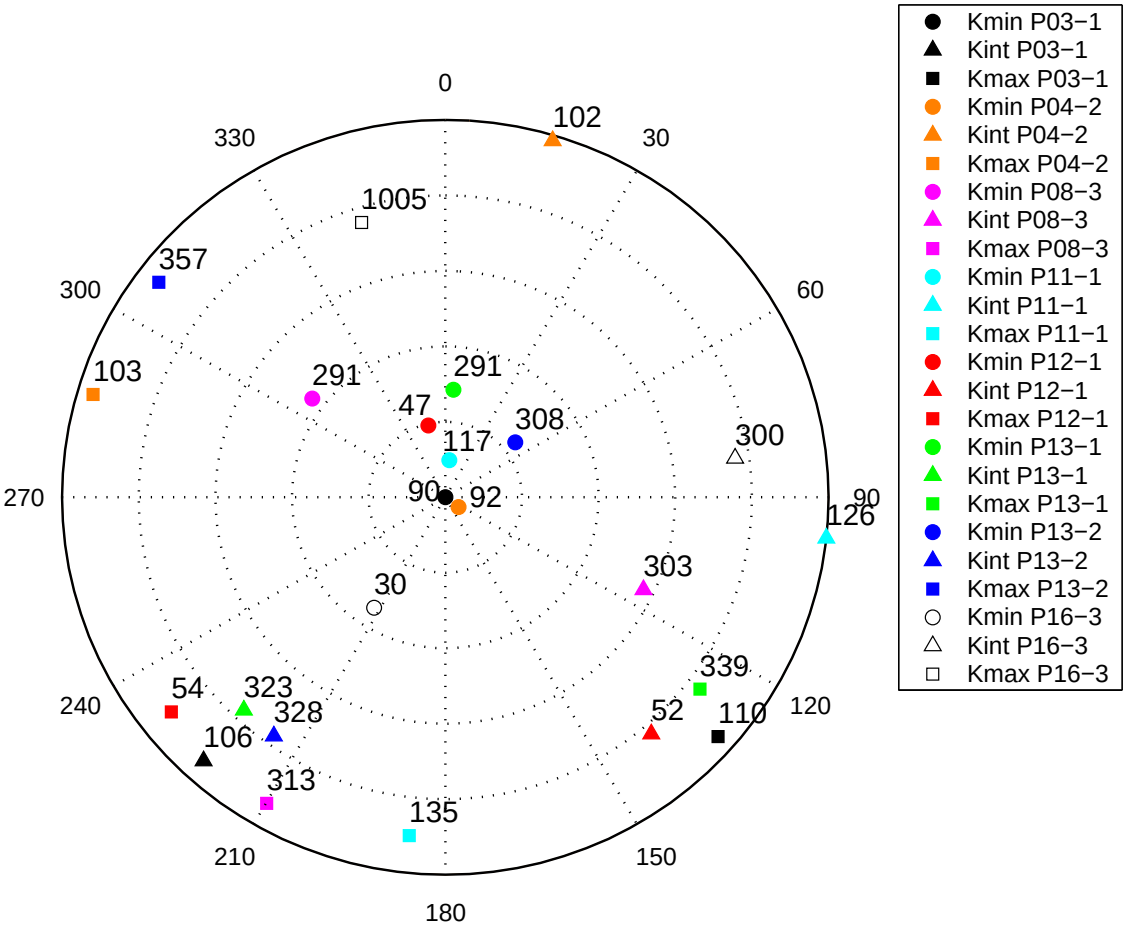

Figure 3.4: The magnitude and direction of all samples' principal axes

(this is, the direction of Z-axis in seismic anisotropy, which is perpendicular to the cutting plane with 90 degree inclination in Figure 3.4). The samples P 08-3 and P16-3 deviate from this trend, due to the fact that the textures were not easily discernable in these two rocks. Their sampling orientation was neither parallel nor perpendicular to the foliation.

Typical ellipsoids are shown in Figure 3.5. The AMS degree of P 03-1 is largest among these three samples. Relying on the specific relationship between the magnetic axes of rock-forming minerals and their shape and crystallographic axes, the usual relationship between AMS and petrofabric, leading to the expression 'normal magnetic fabric', exists in this study by comparing magnetic fabric and rock fabric displayed by visual texture

and thin section in P 03-1 and P 13-1 as the example study. The normal magnetic fabric corresponds to the situation where K_1 is parallel to the structural lineation (of stretching, flow or current origin) and K_3 is perpendicular to the structural foliation (flattening, flow or bedding plane). Magnetic fabric and rock texture are quite similar, that is, the symmetry of the AMS ellipsoid mimics the petrofabric symmetry. As shown in Figure 3.5, P 03-1 and P 13-1 are 'normal' with their inclination of Kmin axis 3.4^0 and 4.3^0, respectively. The plane consisting of Kmax and Kint compare with rock foliation favorably. For the case of sample P 08-3, because of sampling orientation non-perpendicular to foliation, the principal axes of AMS immediately show its difference comparing with other samples (neither are K_1 and K_2 perpendicular to the sampling direction, nor K_3 is parallel to it), which conversely imply that AMS is a useful indication in rock texture.

The anisotropy degree of AMS given by lineation $(P1)$ and foliation $(P3)$ is shown in Figure 3.6. Although there is no clear relationship between $P1$ and $P3$, the result still shows that most samples are below the slope of unit gradient $P_1/P_3 = 1$. That means most are oblate except for P 13-2 (prolate fabrics i.e. above the slope).

The AMS strength and shape have been expressed using Jelinek's parameters (T and P_J) in Figure 3.7, respectively. The figures show that most magnetic susceptibility ellipsoids are oblate for the samples from Pindos and Vourinos Ophiolite. All P_J values vary from 1.03 to 4.72, (average 1.52). The P_J values of all the other samples lie between 1.03 and 1.1 except for P 16-3. That means all samples are weakly magnetic anisotropy except for P 16-3. As illustrated by the distribution of the data, T ranges from -0.12 to 0.7, (average 0.35). All other samples' T values are above the $T = 0$ in the $T - P_J$ graph (Figure 3.7), which means that all others are oblate $(0 < T < 1)$ except for P 13-2 $(-1 < T < 0)$. The values of P 11-1 and P 08-3 are very small, 0.075 and 0.116, respectively. So, they could be classified as neutral ellipsoids (plot close to $T = 0$).

3.5 Conclusion

AMS can be expressed by the tensors that relate the intensity of the applied field (H) to the acquired magnetization (M) of a material through the equation:$M_i = K_{ij}H_j \quad (i, j = 1, 2, 3)$, where K_{ij} is the second-order symmetrical tensor referred to as the susceptibility.

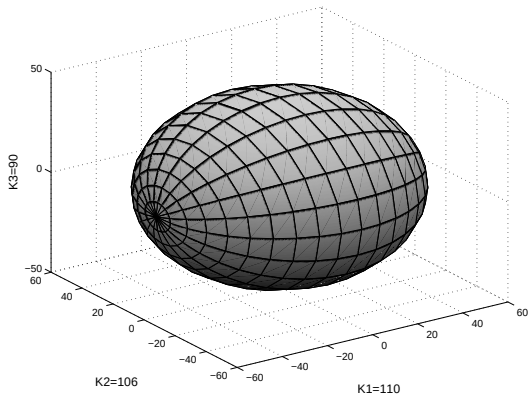

(a) P03-1

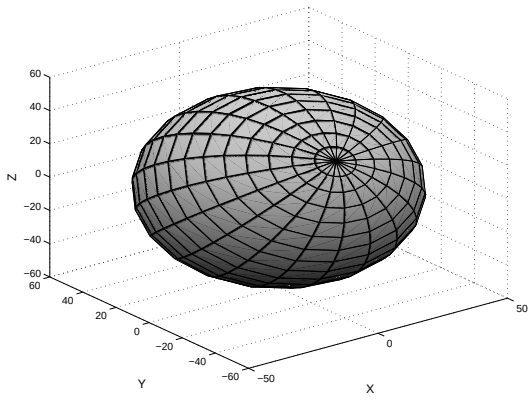

(b) P03-1

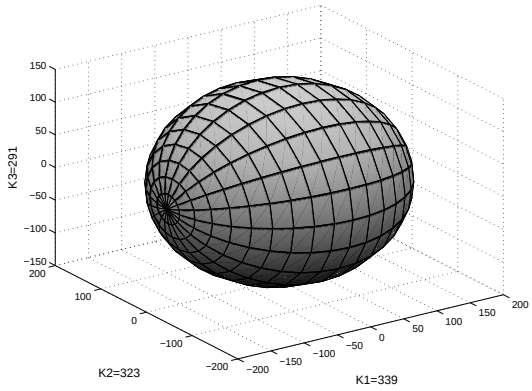

(c) P13-1

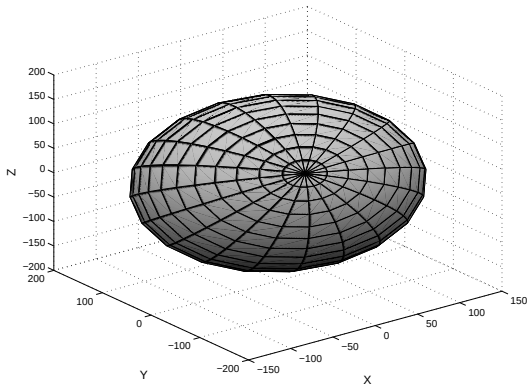

(d) P13-1

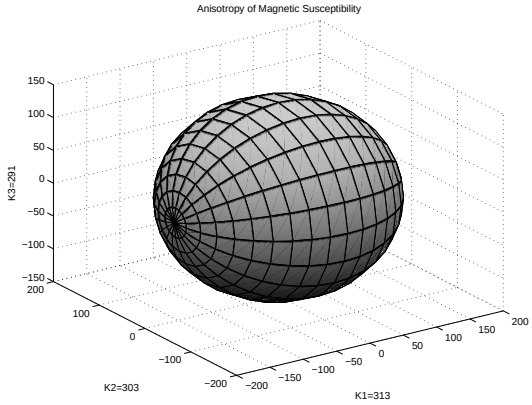

(e) P08-3

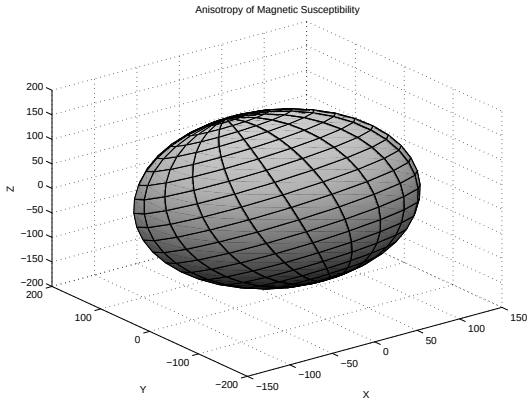

(f) P08-3

Figure 3.5: The typical ellipsoids of samples P 03-1, P13-1, P08-3; To the left: in coordinates of principal axes of AMS, where Z is parallel to K_3. To the Right: in coordinates of reality, where Z is perpendicular to top of the core

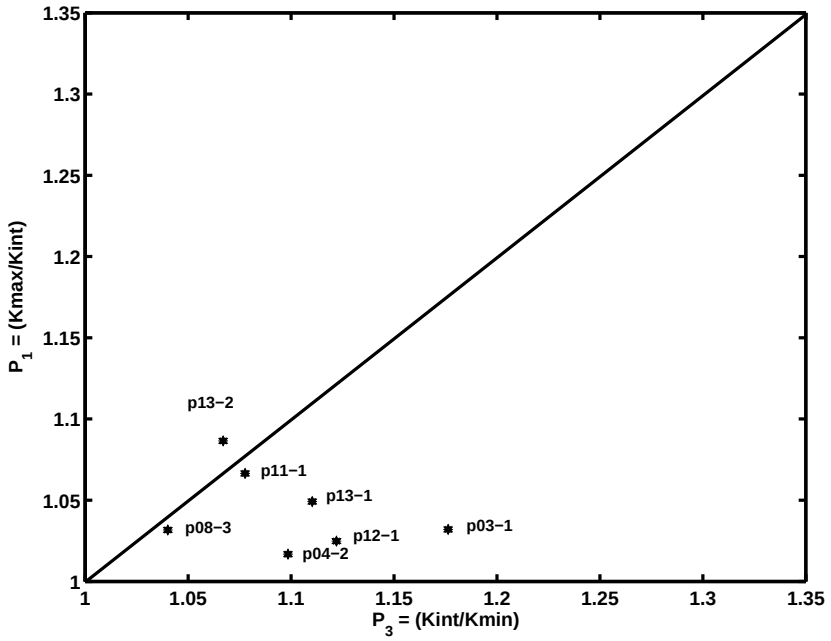

Figure 3.6: Plot of Lineation $(P1)$ vs. Foliation $(P3)$

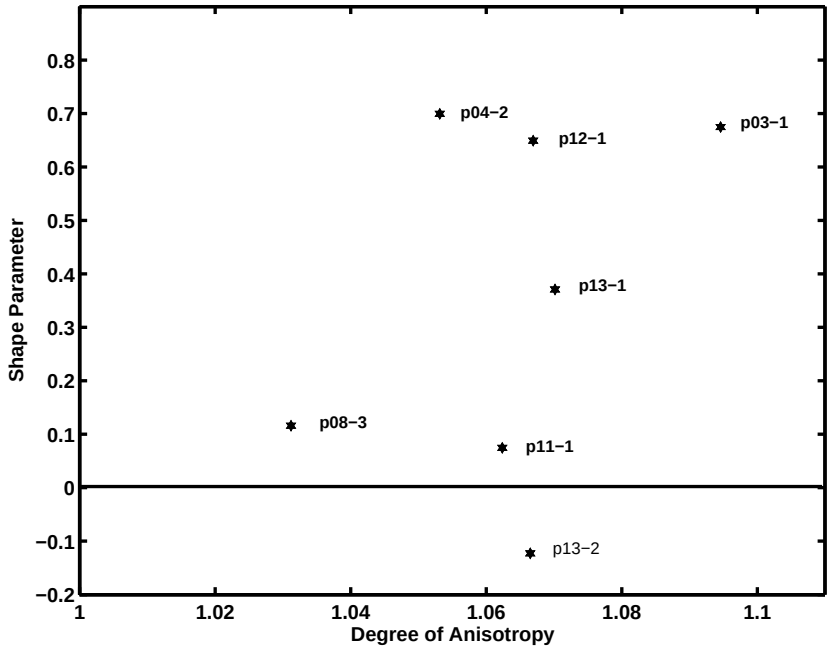

Figure 3.7: Plot of corrected anisotropy degree (P_J) with shape parameter (T)

Table 3.2: Parameters of describing AMS ellipsoid (Parameters defined in 3.3.3)

Sample	K_{mean} $(10^{-5}SI)$	Anisotropy (%)	Density (g/cm^3)	P_J	T	Foliation (K_2/K_3)	Lineation (K_1/K_2)	β (%)
P 13-1	317.8	15.1	2.6	1.07	0.371	1.11	1.049	87.9
P 13-2	330.7	14.8	2.6	1.067	-0.123	1.067	1.087	87.9
P 04-2	99	10.9	2.87	1.053	0.7	1.099	1.017	53.8
P 08-3	302.3	7	3.06	1.031	0.116	1.04	1.032	30.4
P 03-1	101.9	18.9	3.19	1.095	0.675	1.176	1.032	13.6
P 11-1	126.1	13.9	3.28	1.062	0.075	1.078	1.067	2.3
P 12-1	50.9	13.7	3.25	1.067	0.649	1.122	1.049	6.8
P 16-3	444.8	219.2	2.82	4.723	0.313	10.06	3.351	59.9
Average	221.7	39.2	2.96	1.521	0.347	2.219	1.336	42.8

Noted: β : Serpentinization ratio

AMS describes the variation of magnetic susceptibility with direction within a material, and represents the contributions of all rock forming minerals (i.e., dia-, para-, ferri-, and ferromagnetic). Since both paramagnetic and ferrimagnetic minerals are present in this study, the bulk AMS is due to the combination of the anisotropy from the preferred crystallographic orientations of the paramagnetic matrix minerals, and the anisotropy of magnetite grains. Normally, The K_{max} axis represents the magnetic lineation while K_{min} is the pole of the magnetic foliation (the plane containing K_{max} and K_{int} axes).

In general, the variation of the samples' bulk susceptibility is related to their percentage of serpentinization. Table 3.2 lists characterization of magnetic susceptibility and descriptive parameters of the AMS ellipsoid. The overall mean magnetic susceptibility is 221.7×10^{-5} SI, which is close to previously published value(*Toft et al.*, 1990). A plot of the degree of lineation and foliation and a Jelinek's parameters $T - P_J$ graph show that the magnetic susceptibility ellipsoids are mostly oblate in the samples from the Pindos and Vourinos Ophiolite. Examinations that employ the P_J value suggest that the AMS of all the samples except for P16-3 are weakly anisotropic. The variation of AMS degree depends on composition and category of samples, usually between 10 to 20 percent. The AMS degree of dunite group seems to be bigger than serpentinized harzburgite in this study. P16-3 has the largest magnetic susceptibility, the reason is probably because of the heterogeneity of magnetite distribution. Very often the accumulation of magnetic mineral fragments can dominate the entire signal, even if all the minerals contribute to the overall bulk susceptibility.

Chapter 4

Comparison between seismic anisotropy and AMS

4.1 Introduction

Both magnetic fabric and elastic anisotropy measurements were performed on 8 samples of the Pindos and Vourinos ophiolite (Greece). AMS (anisotropy of magnetic susceptibility) and seismic anisotropy are two external manifestations of the intrinsic physical properties of these samples. The correlation between the AMS fabric and rock fabric has been widely discussed (*Hrouda*, 1982; *Borradaile and Henry*, 1997; *Rochette et al.*, 1992; *Yaouancq and Macleod*, 2000; *Bascou et al.*, 2002); the same is the correlation between seismic anisotropy and rock fabric (*Mainprice and Silver*, 1993; *Ji and Salisbury*, 1993a; *Ji et al.*, 1993b; *Barruol and Kern*, 1996; *Kern et al.*, 1996; *Dewandel et al.*, 2003). Measurements and theory of the seismic anisotropy and AMS have been reviewed and discussed in the chapter 2 and 3, respectively. This chapter will largely focus on the comparison of the magnetic to the elastic anisotropy based on these laboratory results.

4.2 Serpentinization influences AMS and seismic anisotropy

The influence by serpentinization on AMS fabric may be more complex than for seismic anisotropy because it results from the combination of all the minerals forming the rock, especially ferrimagnetic or ferromagnetic minerals which may only exist in trace amount. This influence was seen in this study because magnetite can be generated in the serpentinization reaction.

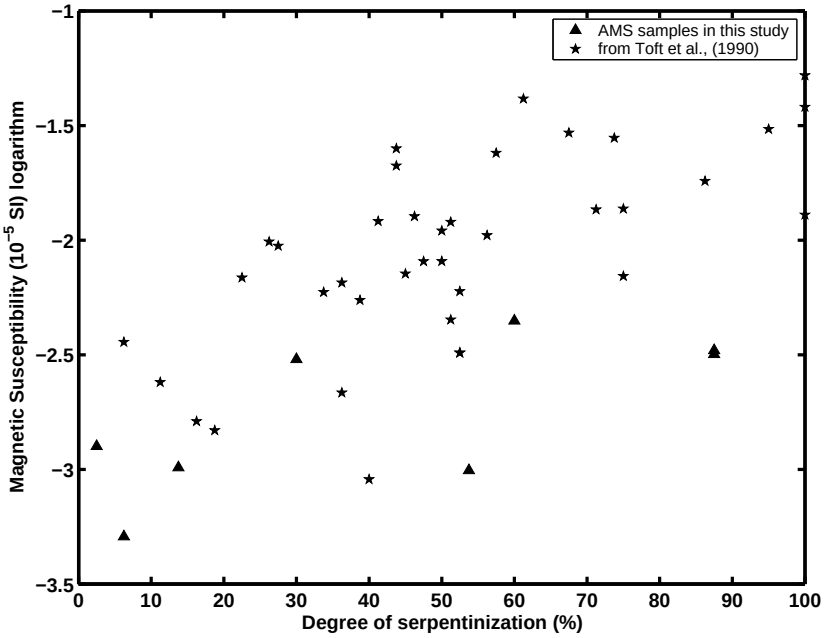

Figure 4.1: Degree of serpentinization vs. mean magnetic susceptibility; Data from this study and that of *Toft et al.* (1990)

4.2.1 Serpentinization and magnetite

Serpentinization is a simple and widespread hydrothermal alteration process, which produces serpentine group minerals, brucite, and magnetite. Serpentine replace the olivine grains by hydration reaction along cracks. Progressive serpentinization create serpentine-filled fractures and form a grid-pattern on the block of peridotite. During the serpentinization, ferrous iron reacts with oxygen and form magnetite (*Best*, 2003). Usually, magnetite occur as the accessory phases. But, because the ferrimagnetic minerals have positive and large susceptibilities compared to the para- and diamagnetic minerals, they are important in AMS studies. Magnetite generated from olive and pyroxene during the reaction of serpentinization will enhance the magnetic susceptibility of the whole rock assemblage. So, the rock may have high magnetic susceptibilities compared both with protoliths and with typical crustal rocks (*Toft et al.*, 1990). The variation of magnetic susceptibility with serpentinization is plotted in Figure 4.1. Several serpentinization reactions from past studies are as follow:

Burch (1968) described density and porosity changes due to serpentinization by:

$$\begin{aligned} 2Mg_2SiO_4 + 3H_2O &= Mg_3Si_2O_5(OH)_4 + Mg(OH)_2 \\ Olivine &= serpentine + brucite \end{aligned} \tag{4.1}$$

$$\begin{aligned} Mg_2SiO_4 + MgSiO_3 + 2H_2O &= Mg_3Si_2O_5(OH)_4 \\ Olivine + enstatite &= serpentine \end{aligned} \tag{4.2}$$

Saad (1969) described iron partitioning by:

$$\begin{aligned} 6Mg_{1.5}Fe_{0.5}SiO_4 + 6H_2O + 0.5O_2 &= 3Mg_3Si_2O_5(OH)_4 + Fe_3O_4 \\ Olivine &= serpentine + magnetite \end{aligned} \tag{4.3}$$

The magnetite is the most common ferrimagnetic mineral (*Hrouda*, 1982). It exhibits spontaneous magnetization, Curie temperatures (578 ^oC), hysteresis, and remanence similar to ferromagnetic mineral like mental iron. However, iron and magnetite have different magnetic structures. The pure iron has a different Curie temperature close to 800 ^oC, either. In order to prove the presence of pure magnetite in this study, we have done the thermomagnetic analysis and isothermal remanent magnetization (IRM) experiments. The Curie temperature of 580 ^oC was revealed the presence of pure magnetite in Figure 4.2. Another evidence came from Figure 4.3. We measured the magnetic moment of the sample during three stages, including the processes demagnetized, saturated in a progressive applied field, and finally reduced to zero and re-saturated in the backfield direction. When the sample was applied a very low field in the opposite direction, the magnetic moment greatly drops down. This phenomena means that ferrimagnetic minerals may exist. The fact that the IRM was saturated twice in an applied field around 300 mT suggest that the ferrimagnetic mineral is magnetite.

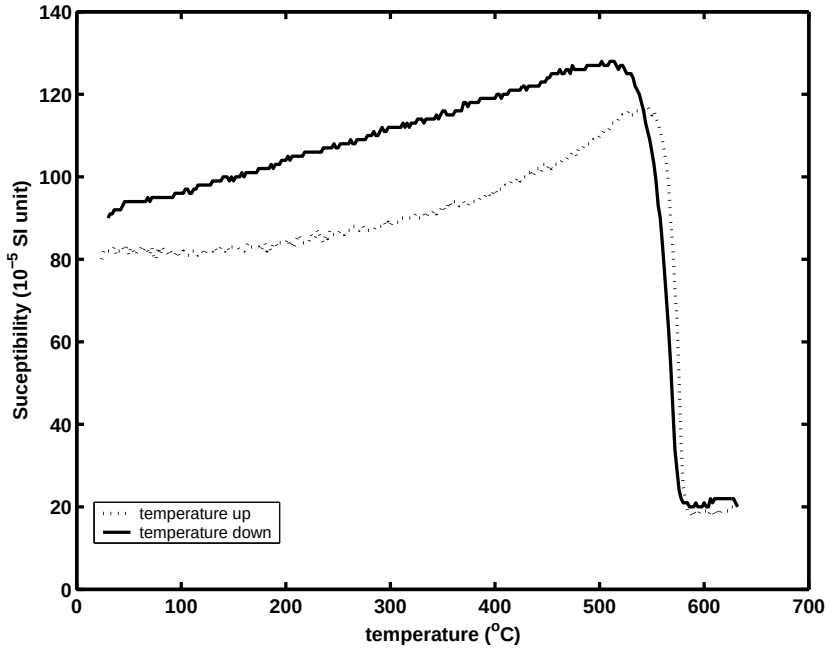

Figure 4.2: Magnetic susceptibility vs temperature for sample P 16-3

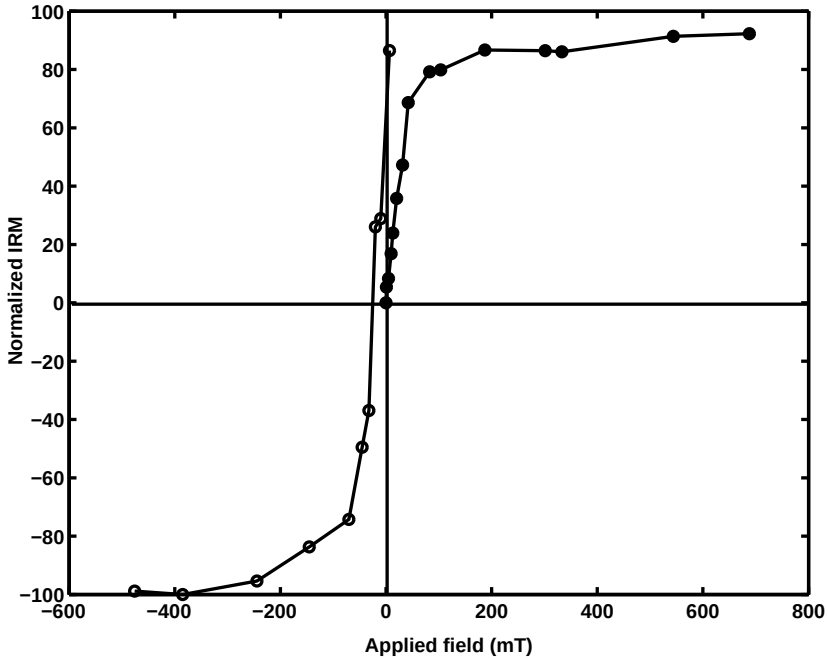

Figure 4.3: Isothermal remanent magnetization for sample P 16-3; the sample P 16-3 was demagnetized at first, then, saturated in a progressively strong applied field, finally, gradually reduced to zero in the backfield direction.

4.2.2 AMS influenced by rock-forming minerals

Mostly, AMS can be a good linkage between the magnetic fabric and the rock fabric in the normal fabric situation. The bulk magnetic susceptibility is usually determined by the volume of the paramagnetic, diamagnetic, and ferrimagnetic (as an accessory phase) material in the entire rock. Usually, the orientation of AMS carrier mineral is the representative of major phases, or accessory ferrimagnetic phase can mimic the orientation of the main phase.

The magnetic fabric of rocks is governed by the AMS carrier minerals. Because the ferrimagnetic minerals have positive and large susceptibilities compared to the para- and diamagnetic minerals, it plays a important role even if as an accessory phase. For magnetite, the AMS is controlled dominantly by their shape anisotropy.

Because most rock-forming minerals are paramagnetic(amphibole, biotite, garnet etc.) or diamagnetic(quartz, feldspars, calcite etc.), they are two important forms of magnetization. Diamagnetism is very weakly magnetized in the opposite direction to the applied field, typically characterized by a negative and small magnetic susceptibility. It is due to the non-cooperative behavior of orbiting electrons when exposed to an applied magnetic field. Paramagnetic materials become a little stronger magnetized in the same direction as in the applied field. In this class of materials, some of the atoms or ions in the material have a net magnetic moment due to unpaired electrons. One of the most important atoms with unpaired electrons is iron. Both of them have no external magnetic field after removal of the applied field. Magnetic susceptibility in these minerals is also temperature dependent. In paramagnetic and diamagnetic minerals, the AMS is typically magnetocrystalline, being determined by the crystallographic lattice preferred orientation of these mineral grains.

As discussed before in most rock-forming minerals, the AMS is due to shape anisotropy and / or magnetocrystalline anisotropy. So, two factors including the anisotropy of the particles themselves and the degree of their alignment determine the magnitude of the magnetic anisotropy. The anisotropy of the individual particles comprise components - crystalline, stress, and shape anisotropy. It must be emphasized here again that no one method of measurement is capable of resolving the contributions of these two factors.

Furthermore, the shape anisotropy of a ferrimagnetic grain can differ radically, in terms of magnitude, depending on whether it is multi- or single-domain. Also, be ware of the distribution anisotropy, which means that non-uniform distribution of interacting ferrimagnetic grains may also results the magnetic anisotropy(*Hargraves et al.*, 1991; *Stephenson*, 1994). All factors will contribute to the complexity of magnetic fabric interpretation. Thus, extreme care and analysis of rocks are needed before attempting to interpret any magnetic anisotropy.

4.2.3 Seismic anisotropy influenced by serpentinization

The influence to seismic anisotropy by serpentinization has been in depth described in chapter 2. In general, the P- and S-wave velocities, the percentage of P- and S-wave anisotropy, and shear wave splitting decreases with increasing degree of serpentinization. The intrinsic seismic anisotropy is controlled by the mineral fabric preferred orientation. In the samples from the Pindos and Vourinos ophiolite (Greece), the olivine relicts are surrounded by the serpentine in the partially serpentinized dunite. The experimental measurements in chapter 2 showed that the seismic anisotropy decreases with the increment of serpentinization in peridotites (*Christensen*, 1966b; *Horen et al.*, 1996). The degree of serpentinization of rock samples has been estimated by mass density measurements, using the linear relation between density and serpentinization established by *Christensen* (1966b). The velocity changes with serpentinization from our laboratory results and those by *Christensen* (1966b) are plotted in Figure 4.4. The macroscopic velocity anisotropy of P- and S-wave velocities was attributed to the controlling of olivine in the peridotite and serpentine lattice preferred orientation (LPO) in the serpentinite (*Kern*, 1993; *Barruol and Kern*, 1996; *Dewandel et al.*, 2003). Olivine usually exhibits a strong preferred orientation. Contrast to olivine, the orthopyroxene texture is less pronounced in literatures. Our laboratory data indicates that most micro-cracks are closed below confining pressure of 100 MPa. Above this pressure the wave velocities and anisotropies are mainly controlled by preferred orientation of the mineral. Comparing with the previous research (*Kern*, 1993; *Dewandel et al.*, 2003) and constituent minerals by X-ray diffraction for the samples, the anisotropy of olivine may play an important role in the Pindos and Vourinos ophilite.

Along the perpendicular direction to rock foliation, the P-wave velocities are lowest

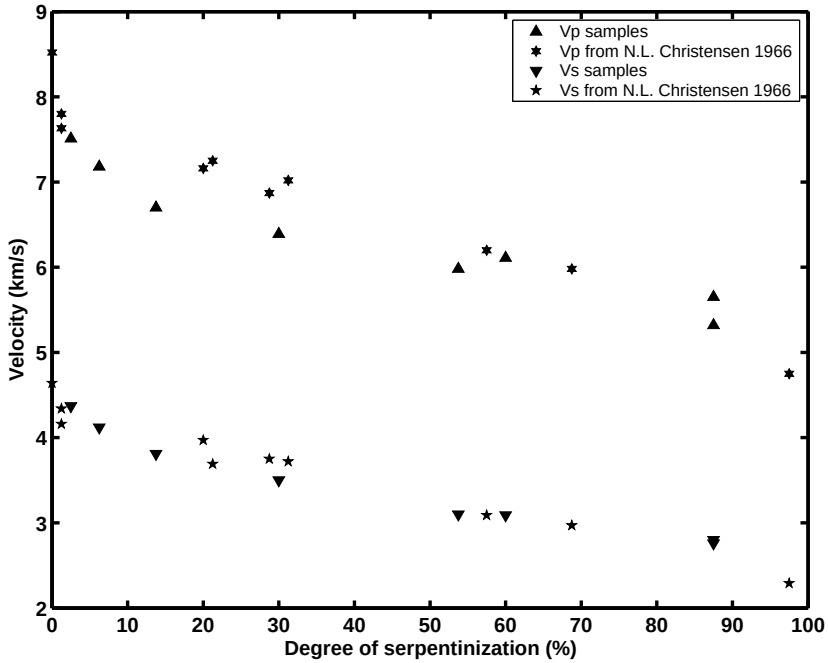

Figure 4.4: Variation of mean velocities (at 200 MPa) vs. Degree of serpentinization

in experiments. The serpentine network seems quite regular and homogeneous. The decrease of seismic anisotropy with serpentinization degree shows that the bulk anisotropy of these rocks primarily results from preferred olivine orientation. The microcracks may play a role in this, but the relatively uniform values observed at pressures in excess of 50 MPa suggests that this role at best is minor.

4.3 Comparison between magnetic fabric and seismic anisotropy

A comparison the orientations and the intensities was carried out to look for a correlation between magnetic fabrics and seismic anisotropy. The AMS fabric orientation is displayed and compared with laboratory slow or fast Vp directions for each sample in Figure 4.5 and 4.6, using information in Figure 3.4 suggest that 75 percent of the samples K_{min} axes have an inclination more than 64 degrees, which means the K_{min} axes of most samples cluster at a direction roughly perpendicular to the rock's principal texture foliation, this latter having been selected only on the basis of visual examination of the samples. As a result, the magnetic fabrics of the samples are maybe distributed in two

groups with this characteristic:

- Normal magnetic fabrics in which K_{min} is nearly perpendicular to the rock foliation plane and is roughly parallel to the Z-axis of velocity measurement;
- Scattered magnetic fabrics (P16-3 and P08-3) for which there is no coincidence between K_{min} axis of the susceptibility ellipsoid and the Z-axis of velocity measurement;

The 72 percent K_{max} and K_{int} axes of samples have inclinations less than 20 degrees. That means there is a roughly coincidence between the plane consisting of K_{max} and K_{int} and the principle rock texture foliation that causes the seismic anisotropy. There is a random declination distribution of the AMS axes because there was no special geographic orientation in samples in the field when they were obtained(Table 3.1 and Figure 3.4).

The direction of the rock's microcrack distributions may have a direct relationship with the crystal structure of the minerals. The orientations of the olivine microcrack networks are therefore related to the whole rock fabrics. From Figure 4.1, we see the serpentine distribution network surrounding olivine grains. Because the original microcrack network will induce the secondary magnetic minerals distribution in serpentinization, the secondary magnetite produced in the serpentinization reaction may simulate the rock fabrics along the microcrack network. So, The preferred orientation of magnetite should be indirectly linked to olivine grain distribution. Based on AMS and seismic anisotropy experiments, the rock textures deduced from magnetic fabric and the seismic anisotropy generally compare favorably in the laboratory measurements. That is, if the preferred orientation of the AMS carrier minerals consists of original paramagnetic minerals or if the secondary magnetic minerals mimic the orientation of the main phases, the AMS and seismic anisotropy are well correlated. Thus, the AMS may offer useful preliminary information with regard to the foliation and the mineral fabric for the whole rocks, regardless of whether it is caused by crystalline or shape anisotropy. This may greatly aid laboratory work because even if we know the crystal anisotropy of olivine and other minerals, it remains difficult to properly select the anisotropic direction of rocks for measurements. As a result, it maybe useful to carry out AMS prior to machining of samples for elastic anisotropic measurements in order to guide the sample preparation.

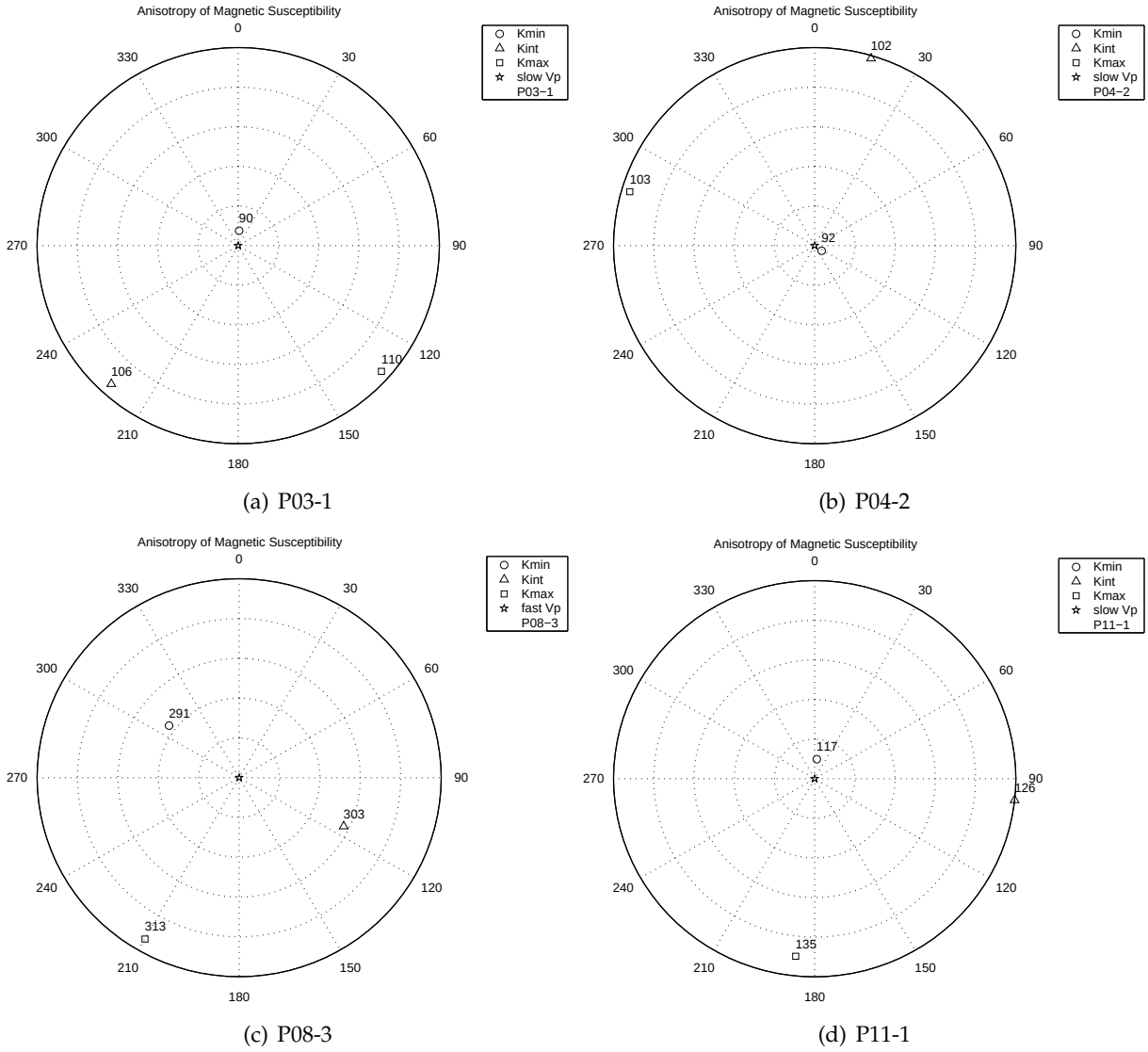

(a) P03-1

(b) P04-2

(c) P08-3

(d) P11-1

Figure 4.5: AMS Minimum, intermediate, and maximum susceptibility axes of samples

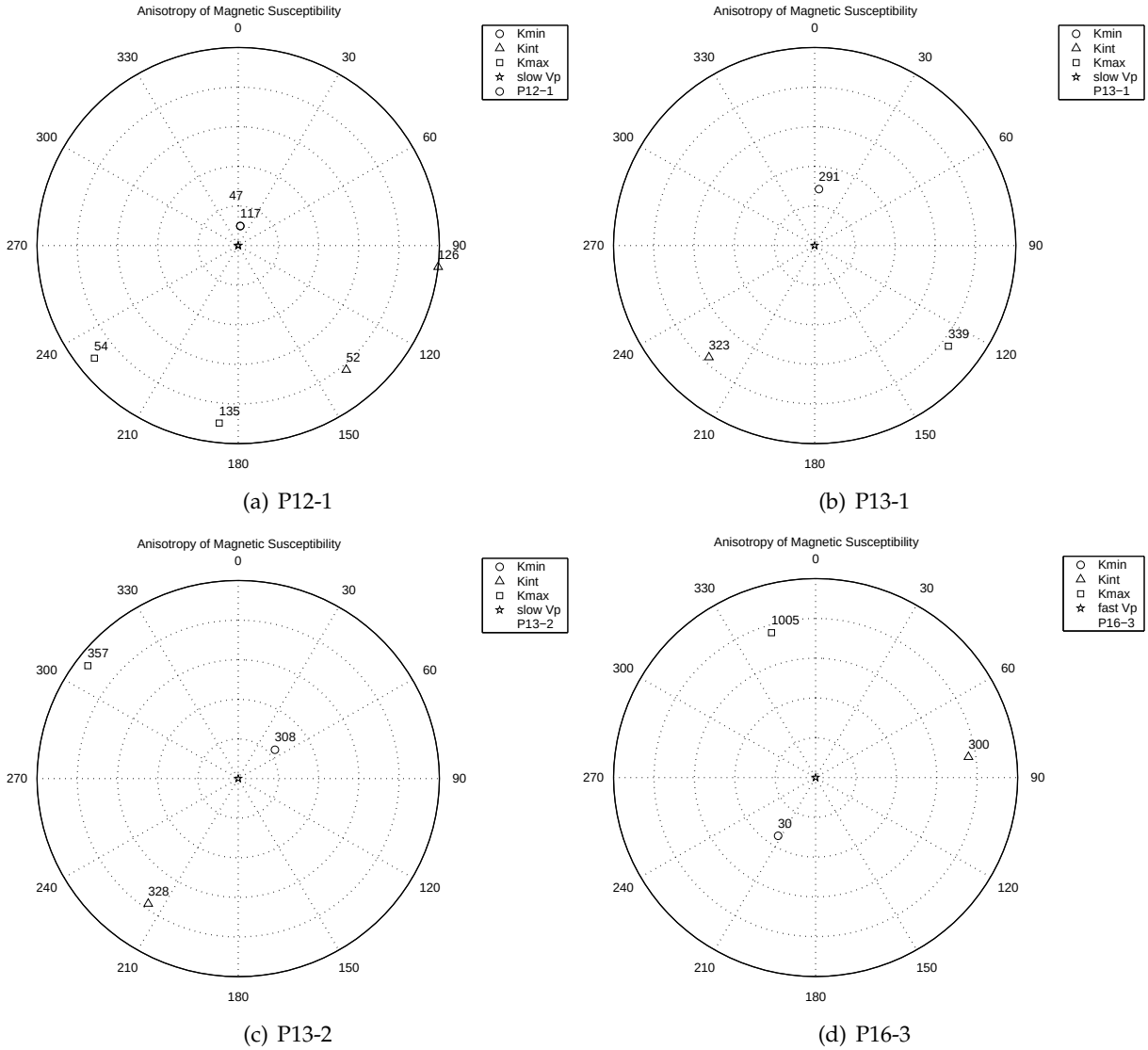

(a) P12-1 (b) P13-1

(c) P13-2 (d) P16-3

Figure 4.6: Cont' AMS Minimum, intermediate, and maximum susceptibility axes of samples

Table 4.1: P-wave velocities and magnetic susceptibilities along Z-axis and within XY plane

	P13-2	P13-1	P11-1	P08-3	P04-2	P03-1	P12-1	P16-3
Kzz mean	264.8	246.2	97.6	243	79.2	79.2	39.9	439.2
Kxy mean	329.5	314.3	125.4	292.5	98.9	105.1	509	627.3
Kzz/Kxy	0.8	0.78	0.78	0.83	0.8	0.75	0.78	0.7
Vp zz (m/s; 200MPa)	5632	5270	7454	6234	5798	6428	6777	6035
Vp xy (m/s; 200MPa)	5672	5359	7566	6546	6151	6974	7568	6174
Vp zz/Vp xy	0.99	0.98	0.99	0.95	0.94	0.92	0.9	0.98

Noted: $K_{xy} = \frac{K_{xx}+K_{yy}}{2}$

Most samples display a rough coincidence between the rock foliation and the fabric deduced from AMS measurements except for P08-3 and P16-3. For these two, the indications of foliation from AMS and from seismic anisotropy are still similar, but totally different with their sample-cutting planes. The samples P08-3 and P16-3 show abnormal phenomena in AMS measurement, because K_{min} is not perpendicular to "presumed foliation plane". The velocity measurements are also anomalous for these samples in that sample-cutting plane is far away "presumed foliation plane". Usually, sample-cutting surfaces are parallel or perpendicular to the visible principal rock texture,i.e. "presumed foliation plane", but these two were without a clear visible texture making selection of the surface to cut problematic. Thin sections (Figure A.3 and A.9 in Appendix) and X-ray diffractions (Figure C.7 and C.8 in Appendix) show that both 'non-coincidences' in AMS and in seismic anisotropy come from the sampling directions being neither perpendicular nor parallel to the foliation of rock in these two. Despite this, the phenomena show that both the AMS and the velocities are sensitive to the rock fabric. In addition, the comparison between AMS and seismic anisotropy in P16-3 proves that the secondary magnetite indeed tracks the preferred orientation of the real rock fabrics. Otherwise, the accumulation of magnetic minerals may overlap the original rock fabrics of P16-3 (Figure A.9 in Appendix), which will lead to non-coincidence between AMS and the seismic anisotropy direction.

Even though the serpentine group minerals have a complex composition, we still hope to try some quantitative comparison between the intensities and directional dependence between AMS and the seismic anisotropy. The results show that there is not only a

coincidence in the direction, but also possible in the intensities between AMS and seismic anisotropy. The AMS are more sensitive to the composition of samples. P-wave velocities (200 MPa) ratio $Vpzz/Vpxy$ and magnetic susceptibility ratio Kzz/Kxy in Z-axis and along X and Y plane are listed in table 4.1. The ratios show that both magnetic susceptibility and velocity have the smaller value along the Z-axis than along XY plane. Kzz is the average magnetic susceptibility along the Z-axis, and Kxy is the average magnetic susceptibility along the X and Y-axis. Kzz/Kxy display a directional dependence in the magnetic susceptibility similar to that for the measurement of velocity anisotropy, but the the relative difference of velocities are much smaller than the magnetic susceptibility.

In order to make a more valid comparison between velocity anisotropy and variable trend of AMS intensities, we choose the anisotropic ratios of different parameters including the P-wave velocities at 200 MPa and Kzz and Kxy. For the convenience of comparison, the anisotropic ratios are defined by the same calculation method for both seismic and magnetic parameters as the ratio between the difference and average value of each one: $(A_{max} - A_{min}) \times 2/(A_{max} + A_{min})$.

Figure 4.7 somehow shows the correlation between seismic anisotropy ratio and magnetic anisotropy ratio in harzburgite and dunite groups, respectively. Without a big change in magnetic susceptibility, the seismic anisotropy may increase while magnetic anisotropy increase, except the P 12-1 and P16-3. That maybe caused by the extreme value of their magnetic susceptibility, see table 3.1. AMS is much more sensitive to the rock composition than the seismic anisotropy. The comparability between magnetic anisotropy ratio and seismic anisotropy ratio is only available in the strictly limited lithological scale. The variances of accessory magnetic minerals should be noted as an important influence in quantitative comparison in the future.

4.4 Conclusion

In this chapter, we compare the AMS with seismic anisotropy in a suite of samples from the Pindos and Vourinos ophiolite (Greece), with densities ranging from 2.6 to 3.28 g/cm^3, corresponding to degrees of serpentinization from 87.9 % to 2.3 %. Because the serpentinization reaction can produce magnetite, the magnetic anisotropy ratio increases with

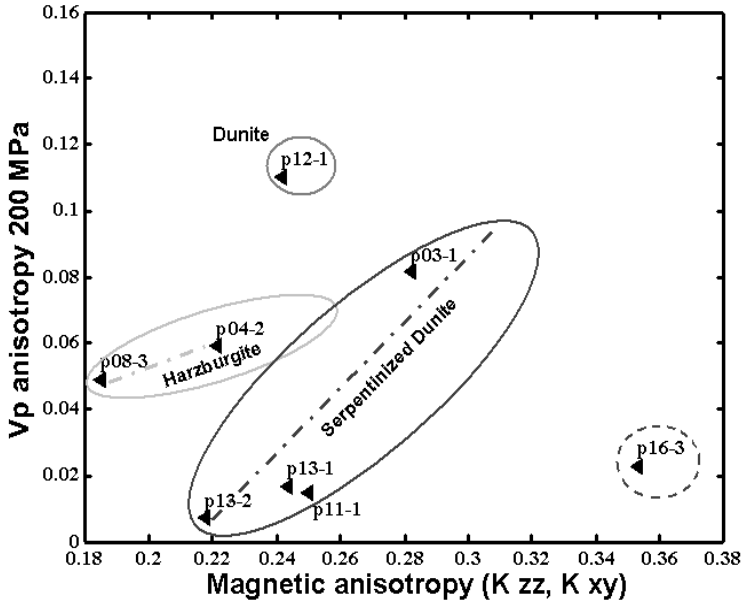

Figure 4.7: Vp anisotropy (200 MPa) vs. Magnetic anisotropy

seismic anisotropy properly only within the necessary limit that there is not too much variability of the magnetic minerals among samples. The magnitude of bulk magnetic susceptibility in laboratory measurements shows that the bulk AMS of the rocks come from both the paramagnetic minerals and magnetite. There is a generally good coincidence between the magnetic fabric and the rock texture deduced from seismic method. The K_{min} axis of the AMS ellipsoid trends to be perpendicular to the rock foliation plane for most samples; and the magnetic fabric plane (consisting of K_{max} and K_{int}) trends to coincide with the rock foiliation plane. From the comparison with other research (*Siegesmund and Dahms*, 1994; *Yaouancq and Macleod*, 2000; *Lagroix and Borradaile*, 2000; *Bascou et al.*, 2002), AMS could be acted as a proxy for the orientation distribution of rock fabric (Figure 4.8). But, caution is necessary in the direct interpretation of preferred crystallographic orientations of crustal rocks before determining the reliability of AMS in some samples. In our case, the reason is that AMS arise from paramagnetic minerals and the secondary magnetite that follows the orientation of the main phases. Velocities and calculation of elastic properties in chapter 2 evaluated the symmetries and rock texture of samples. The symmetric axis of samples all have a good coincidence with K_{min} axis of

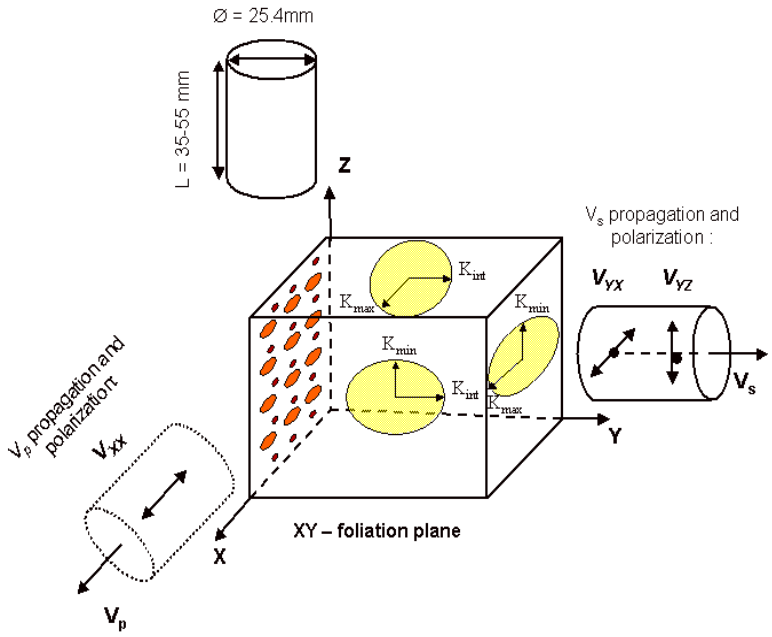

Figure 4.8: Schematic comparison between magnetic fabric and rock texture

their AMS ellipsoid. The rock fabric deduced from AMS ellipsoid generally correlated with the principal texture of the rocks.

Therefore, by comparing the similarity, we conclude that determining rock fabric from the magnetic fabrics could be a useful proxy for petrofabric measurement to predict. We should obtain more useful information quantitatively concerning the factors to influence the relationship between the intensity of magnetic susceptibility and the rock magnetic fabric for more pure minerals and typical rocks. These may further allow us to compare rock fabrics with the magnetic fabrics.

Chapter 5

Future work

Vourinos Ophiolite with high magnetic susceptibility is a good candidate for comparison between AMS studies and seismic anisotropy . Magnetic fabrics are usually representative of the secondary magnetite in serpentinization and the primary paramagnetic minerals assemblage. The secondary magnetite produced in serpentinization can somehow mimic the principal rock texture. The studies show that generally there are coincidences in both directions and possible intensities between anisotropy of magnetic susceptibility and seismic anisotropy, although some angular departures between axes in two different systems are present. Nonetheless, studying and understanding the similarity between AMS and seismic anisotropy may help to develop a new method using fabrics deduced from fast and simple AMS measurements instead of traditional laboratory ultrasonic methods. This could guide the design of elastic anisotropy measurement in the future.

Magnetic susceptibility, AMS, P- and S-wave velocities, and seismic anisotropy are all external manifestations of the intrinsic crystallographic properties of rock-forming minerals. Magnetic fabrics were obtained from the AMS measurements; petrofabric was evaluated based on P- and S-wave velocity measurement on the same samples. The relationship between petrofabric and magnetic fabric and their mutual directional dependence, compared favorably. This study presents only a semi-qualitative conclusion at this point in the research, but it identified an interesting correlation between anisotropy of magnetic susceptibility (AMS) and seismic anisotropy, this will allow us to develop numerical method to quantitatively evaluate the comparability in the future. On the

other hand, anisotropy of low field magnetic susceptibility (AMS), as a sensitive indicator of rock texture and strain by its intrinsic petrofabric meanings, is used to measure and deduce the petrofabric of rocks. But, although sensitive, its interpretation could be easily complex by tiny compositional changes, for example, magnetite in reaction of serpentinization. So, caution is always necessary. In general, the degree of preferential orientation of the magnetic and other rock-forming minerals contained in a rock has significant effects both in the magnetic ellipsoid and the seismic anisotropy. Although we conclude that the magnetic fabrics could be an useful proxy in determining the petrofabric, this is not to imply that the comparability between magnetic anisotropy and seismic anisotropy is simple. Some problems could arise in the interpretation of the magnetic fabrics of rocks just as in other techniques of petrofabric analysis. Quantitatively comparison between AMS and seismic anisotropy will be the important topic in the future work. To accurately evaluate the influence of mineral orientation and composition, theoretical work on the quantitative relationship between the magnetic fabric and rock fabric is imperative. In addition, to really compare rock texture and quantitatively describe mineral orientation, more quantitative texture information will need to be obtained from X-ray, neutron, or electron (EBSD) background scattered diffraction techniques to improve the texture analysis in this phase.

The numerical modeling method offers a good approach to assess the petrofabric quantitatively for single crystal and polymineralic assembly both for seismic anisotropy and AMS. For seismic anisotropy, velocities are closely related to the intrinsic structure. Seismic velocities by laboratory experiment can be used to evaluate anisotropies, elasticity, and symmetries for the whole mineral assembly. Since seismic properties of single crystals are known for many rock-forming minerals, the overall seismic velocities and anisotropies of polycrystalline rocks could be computed according to the Christoffel equation and Voigt-Reuss-Hill averaging scheme by considering the LPO and the fraction volume of each constituent mineral. There are many theoretical works to explain the relationship between seismic anisotropy and the texture of the constituent minerals by considering the single crystal properties and quantifying the elastic properties. But, comparison to seismic anisotropy, however, there are few laboratory and theoretical works devoted to AMS calculation. In principle, we could calculate AMS from texture,

LPO, and the properties of single crystal by considering their fraction volume, using similar methods as used for computation of seismic properties. For the theoretical work of AMS, one of the major problems concerning with the source of magnetic susceptibility is the quantitative relationship between the magnetic fabric and rock fabric. Another problem is a lack of detailed magnetic database of minerals and rock, because magnetic susceptibilities of single crystal usually vary in a range instead of a constant value by the sensitivity to its composition.

We still need to obtain more useful information quantitatively concerning the factors influencing relationships between the intensity of magnetic susceptibility and the magnetic fabric. A more sophisticated theoretical model of AMS will help to understand the complexities of magnetic fabric by different minerals and rocks.

Bibliography

Anderson, D. L., B. J. Minster, and D. Cole, The effect of oriented cracks on seismic velocities, *J. Geophys. Res.*, *79*, 4011–4015, 1974.

Auld, B. A., *Acoustic fields and waves in solids*, R.E. Krieger, 1990.

Bachman, R. T., Acoustic anisotropy in marine sediments and sedimentary rocks, *J. Geophys. Res.*, *84*, 7661–7663, 1979.

Baker, D. W., and N. L. Carter, Seismic velocity anisotropy calculated for ultramafic minerals and aggregates, *Geophys. Monogr., Am. Geophys. Union*, *16*, 157 –166, 1972.

Balsey, J. R., and A. F. Buddington, Magnetic susceptibility anisotropy and fabric of some adirondack granites and orthogneisses, *Am. J. Sci.*, *258(A)*, 6–20, 1960.

Banik, N. C., Velocity anisotropy of shales and depth estimation in the north sea basin, *Geophysics*, *49*, 1411–1419, 1984.

Barruol, G., and H. Kern, Seismic anisotropy and shear-wave splitting in the lower-crustal and upper-mantle rocks from the ivrea zone-experimental and calculated data, *Phys. Earth Planet. Inter.*, *95*, 175– 194, 1996.

Bascou, J., M. I. B. Raposo, A. Vauchez, and M. E. Silva, Titanohematite lattice-preferred orientation and magnetic anisotropy in high temperature mylonites, *Earth and Planet. Sci. Lett.*, *198*, 77–92, 2002.

Bass, J. D., Elasticity of minerals, glasses, and melts, in *Mineral Physics and Crystallgraphy,A Handbook of Physical Constants*, edited by A. R. S. 2, 1995.

Best, M. G., *Igneous and metamorphic petrology*, Blackwell publishing, 2003.

Birch, F., The velocity of compressional waves in rocks to 10 kilobars. 1, *J. Geophys. Res.*, *65*, 1083–1102, 1960.

Birch, F., The velocity of compressional waves in rocks to 10 kilobars. 2, *J. Geophys. Res.*, *66*, 2199–2224, 1961.

Blum, P., *Physical properties handbooks: a guide to the shipboard measurement of physical properties of deep-sea cores*, ODP Tech. Note, 26, 1997.

Borradaile, G., Magnetic susceptibility, petrofabrics and strain, *Tectonphysics*, *156*, 1–20, 1988.

Borradaile, G., Magnetic fabrics and petrofabrics: their orientation distributions and anisotropies, *J. Struct. Geol.*, *23*, 1581–1596, 2001.

Borradaile, G., and B. Henry, Tectonic applications of magnetic susceptibility and its anisotropy, *Earth Sci. Rev.*, *42*, 49–93, 1997.

Borradaile, G. J., and Stupavsky, Anisotropy of magnetic susceptibility: Measurement schemes, *Geophysical Research Letters*, *22*, 1957–1960, 1995.

Burch, S. H., Tectonic emplacement of the burro mountain ultramafic body, southern santa lucia range, california, *Geol. Soc. Am. Bull.*, *79*, 527–546, 1968.

Carlson, R., The abundance of ultramafic rocks in atlantic oceanic crust, *Geophysical Journal International*, *144*, 37–48, 2001.

Cheadle, S. P., R. J. Brown, and D. C. Lawton, Orthorhombic anisotropy: A physical seismic modeling study, *Geophysics*, *56*, 1603– 1613, 1991.

Cholach, P., J. Molyneux, and D. R. Schmitt, Flin flon belt seismic anisotropy: elastic symmetry, heterogeneity, and shear wave splitting, *submitted to Can. J. Earth Sciences, manuscript pp. 50.*, 2004.

Christensen, N. I., Compressional wave velocities in metamorphic rocks at pressures to 10 kilobars, *J. Geophys. Res.*, *70*, 6147–6164, 1965.

Christensen, N. I., Shear wave velocities in metamorphic rocks at pressures to 10 kilobars, *J. Geophys. Res.*, *71*, 3549–3556, 1966a.

Christensen, N. I., Elasticity of ultrabasic rocks, *J. Geophys. Res.*, *71*, 5921– 5931, 1966b.

Christensen, N. I., The abundance of serpentinites in the oceanic crust, *J. of Geology*, *80*, 709– 719, 1972.

Christensen, N. I., Poisson's ratio and crustal seismology, *Journal of Geophysical Research*, *101(B2)*, 3139–3156, 1996.

Christensen, N. I., and S. Landquist, Pyroxene orientation within the upper mantle, *Bull. Geol. Soc. Am.*, *93*, 279–288, 1982.

Christensen, N. I., and M. H. Salisbury, Seismic anisotropy in the oceanic upper mantle: Evidence from the bay of islands ophiolite complex, *J. Geophys. Res.*, *84*, 4601– 4610, 1979.

Collison, D., *Methods in Rock Magnetism and Paleomagnetism*, Chapman and Hall, London, 503p., 1983.

Cox, A., and R. R. Doell, Review of paleomagnetism, *Bull. Geol. Soc. Am.*, *71*, 645–768, 1960.

Crampin, S., Seismic wave propagation through a cracked solid: polarization as a possible dilatancy diagnostic, *Geophy. J. R. Astron. Soc.*, *53*, 467–496, 1978.

Crampin, S., A review of wave motion in anisotropic and cracked elastic-media, *Wave Motion*, *3*, 343–391, 1981.

Deer, Z., Howie, *An introduction to The Rock - Forming Minerals*, 2nd ed., Longman Scientific and Technical, 1992.

Dewandel, B., F. Boudier, H. Kern, W. Warsi, and D. Mainprice, Seismic wave velocity and anisotropy of serpentinized peridotite in the oman ophilite, *Tectonophysics*, *370*, 77–94, 2003.

Dunlop, D., and O. Özdemir, *Rock magnetism: Fundamentals and frontiers*, Cambridge University Press, 1997.

Escartín, J., G. Hirth, and B. Evans, Effects of serpentinization on the lithospheric strength and the style of normal faulting at slow-spreading ridges, *Earth and Planetary Science Letters*, *151*, 181–190, 1997.

Escartín, J., G. Hirth, and B. Evans, Strength of slightly serpentinized peridotites: Implications of the tectonics of oceanic lithosphere, *Geology*, *29*, 1023–1026, 2001.

Fedorov, F. I., *Theory of elastic waves in crystals*, Plenum Press, 1968.

Gass, I. G., S. J. Lippard, and A. W. Shelton, *Ophiolites and oceanic lithosphere*, 13 ed., Geological Society London, Special Publication, 1984.

Girdler, R. W., The measurement and computation of anisotropy of magnetic susceptibility of rocks, *Geophys. J. R. Astr. Soc.*, *5*, 34–44, 1961.

Granar, L., Magnetic measurements on swedish varved sediments, *Arkiv. F. Geofysik*, *3*, 1–40, 1958.

Hanna, W. F., Weak-field magnetic susceptibility anisotropy and its dynamic measurement, *U. S. Geol. Surv. Bull.*, *1418*, 1–73, 1977.

Hargraves, R. B., D. Johnson, and C. Y. Chan, Distribution anisotropy: the cause of ams in igneous rocks?, *Geophys, Res. Lett.*, *18*, 2193–2196, 1991.

Helbig, K., *Foundations of anisotropy for exploration seismics*, Pergamon, 1994.

Hess, H. H., Geological hypothesis and the earth's crust under the oceans, *Proceeding of the Royal Society of London*, *222(A)*, 391–408, 1954.

Hess, H. H., Seismic anisotropy of the upper mantle under oceans, *Nature*, *230*, 629–631, 1964.

Holbrook, W. S., W. D. Mooney, and N. I. Christensen, The seismic velocity structure of the deep continental crust, in *The Continental Lower Crust, Developments in Geotectonics*, edited by D. M. Fountain, R. Arculus, and R. Kay, vol. 23, pp. 1–34, 1992.

Horen, H., M. Zamora, and G. Dubuisson, Seismic waves velocities and anisotropy in serpentinized peridotites from xigaze ophiolite: abundance of serpentine in slow spreading ridge, *Geophys. Res. Lett.*, *23*, 9 – 12, 1996.

Hornby, B. E., Experimental determination of the anisotropic elastic properties of shales, in *Seismic anisotropy*, edited by E. Fjar and R. M. Holt, vol. Society of Exploration Geophysicists, pp. 238–296, 1996.

Hrouda, F., Magnetic anisotropy of rocks and its application in geology and geophysics, *Geophys. Surv.*, *5*, 37–82, 1982.

Hrouda, F., The effect of quartz on the magnetic susaceptibility of quartzite, *Stud. Geoph. Geod.*, *30*, 39–45, 1986.

Ising, E., On the magnetic properties of varved clay, *Arkiv Astron. Fysik*, *29 A(5)*, 1–37, 1942.

Jackson, M., Anisotropy of magnetic remanence: a brief review of mineralogical sources, physical origins and geological applications, and comparison with susceptibility anisotropy, *Pure Appl. Geophys.*, *136*, 1–28, 1991.

Janák, F., Determination of anisotropy of magnetic susceptibility of rocks, *Studia geoph. et geod.*, *9*, 290–300, 1965.

Jelinek, V., The statistical theory of measuring anisotropy of magnetic susceptibility of rocks and its applcation, *Brno, Geofyzika*, pp. 1–88, 1977.

Jelinek, V., Statistical processing of anisotropy of magnetic susceptibility measured on groups of specimens, *Studia geoph. et geod.*, *22*, 50–62, 1978.

Jelinek, V., Characterization of the magnetic fabric of rocks, *Tectonphysics*, *79*, 63–67, 1981.

Ji, S., and M. Salisbury, Shear-wave velocities, anisotropy and splitting in high grade mylonites, *Tectonphysics*, *221*, 453–473, 1993a.

Ji, S., M. Salisbury, and S. Hanmer, Petrofabric, p-wave anisotropy and seismic reflectivity of high-grade tectonites, *Tectonphysics*, *222*, 195–226, 1993b.

Ji, S., X. Zhao, and D. Francis, Calibration of shear-wave splitting in the subcontinental upper mantle beneath active orogenic belts using ultramafic xenoliths from the canadian cordillera and alaska, *Tectonphysics*, *239*, 1–28, 1994.

Johnston, J. E., and N. I. Christensen, Seismic anisotropy of shales, *J. Geophys. Res.*, *100(B4)*, 5991– 6003, 1995.

Jones, T., and A. Nur, Seismic velocity and anisotropy in mylonites and the reflectivity of deep crustal fault zones, *Geology*, *10*, 260–263, 1982.

Jones, T., and A. Nur, The nature of seismic reflections from deep crustal fault zones, *J. Geophys. Res.*, *89(B5)*, 3153–3171, 1984.

Kaarsberg, E. A., Introductory studies of natural and artificial argillaceous aggregates by sound-propagation and x-ray diffraction methods, *J. Geol.*, *67*, 447–472, 1959.

Kebaili, A., and D. R. Schmitt, Velocity anisotropy observed in wellbore seismic arrivals: Combined effects of intrinsic properties and layering, *Geophysics*, *61*, 12–20, 1996.

Kern, H., P- and s-waves velocities in a crustal and mantle rocks under the simultaneous action of high confining pressure and high temperature and the effect of the rock microstructure, in *High-Pressure Research in Geosciences*, edited by W. Schreyer, vol. Schweitzerbart, Stuttgart, pp. 15–45, 1982.

Kern, H., P- and s-wave anisotropy and shear wave splitting at pressure and temperature in possible mantle rocks and their relation to the rock fabric, *Phys. Earth Planet. Inter.*, *78*, 245–256, 1993.

Kern, H., L. Burlini, and I. V. Ashchepkov, Fabric-related seismic anisotropy in upper-mantle xenoliths: evidence from measurements and calculations, *Phys. Earth Planet. Inter.*, *95*, 195–209, 1996.

Kern, H., B. Liu, and T. Popp, Relationship between anisotropy of p and s wave velocities and anisotropy of attenuation in serpentinite and amphibolite, *J. Geophys. Res.*, *102(B2)*, 3051–3065, 1997.

Lagroix, F., and G. Borradaile, Magnetic fabric interpretation complicated by inclusions in mafic silicates, *Tectonophysics*, *325*, 207–225, 2000.

Long, C., and N. I. Christensen, Seismic anisotropy of south african upper mantle xenoliths, *Earth and Planetary Science Letters*, *179*, 551–565, 2000.

Mah, M., *Experimental determination of the elastic coefficients of anisotropic materials with the slant-stack method*, M. Sc. thesis, University of Alberta, 1999.

Mah, M., and D. R. Schmitt, Experimental determination of the elastic coefficients of an orthorhombic material, *Geophysics*, *66*, 1217–1225, 2001.

Mah, M., and D. R. Schmitt, Determination of the complete elastic stiffness from ultrasonic velocity measurements, *J. Geophys. Res.*, *108(B1)*, 2016, 2003.

Mainprice, D., and P. Silver, Interpretation of sks-waves using samples from the subcontinental lithosphere, *Phys. Earth Planet. Inter.*, *78*, 257–280, 1993.

Markham, M. F., Measurement of elastic constants by the ultrasonic pulse method, *British J. Appl. Phys.*, *6*, 56–63, 1957.

Molyneux, J. B., and D. R. Schmitt, First break timing: Arrival times by direct correlation, *Geophysics*, *64*, 1492–1501, 1999.

Molyneux, J. B., and D. R. Schmitt, Compressional-wave velocities in attenuating media: A laboratory physical modeling study, *Geophysics*, *65*, 1162–1167, 2000.

Musgrave, M. J. P., *Crystal acoustics*, Holden Day, 1970.

Nagata, T., *Rock magnetism*, 2 ed., Maruzen, Tokyo, 1961.

Nicholas, A., and N. I. Christensen, Formation of anisotropy in upper mantle peridotites - a review, in *Composition, Structure and Dynamics of the Lithosphere - Ashenosphere system*, edited by K. Fuchs and C. Froidevaux, vol. Geodyn. Series, 16, pp. 111–123, 1987.

Nickel, E. H., and M. Nichols, *Mineral reference manual*, Van Nostrand Reinhold. New York, 1991.

Nicolas, A., and J. Poirier, *Crystalline plasticity and solid state flow in metamorphic rocks*, Wiley, London, 1976.

Nur, A., Effects of stress on velocity anisotropy in rocks with cracks, *J. Geophys. Res.*, *76*, 2022–2034, 1971.

Nur, A., and G. Simmons, Stress-induced velocity anisotropy in rocks: an experimental study, *J. Geophys. Res.*, *74*, 6667–6674, 1969.

Nye, J. F., *Physical properties of Crystal*, Oxford University, 1957.

Owens, W. H., Mathematical model studies on factors affecting the magnetic anisotropy of deformed rocks, *Tectonphysics*, *24*, 115–131, 1974.

Owens, W. H., and E. H. Rutter, The development of magnetic susceptibility anisotropy through crystallographic preferred orientation in a calcite rock, *Phys. Earth Planet. Ints.*, *16*, 215–222, 1978.

Pros, Z., and V. Babuska, A method for investigating the elastic anisotropy on spherical rock samples, *Z. Geophys.*, *33*, 289–291, 1967.

Rassios, A., L. Beccaluva, V. Bortolotti, A. Mavrides, and E. M. Moores, The vourinos ophiolitic complex, *Ofioliti*, *8*, 275–292, 1983.

Rassios, A. G., A. ad Smith, Constraints on the formation and emplacement age of western greek ophiolites (vourinos, pindos, and othris) inferred from deformation structures in peridotites, in ophiolites and oceanic crust, in *New insights from Field Studies and the Ocean Drilling Program*, edited by Y. Dilek, E. Moores, D. Elthon, and A. Nicolas, vol. Geological Soc. Amer. Special Paper, 349, pp. 473–483, 2000.

Rochette, P., M. Jackson, , and C. Aubourg, Rock magnetism and the interpretation of anisotropy of magnetic susceptibility, *Rev. Geophys.*, *30*, 209–226, 1992.

Saad, A. H., Magnetic properties of ultramafic rocks from red mountain, california, *Geophysics*, *34*, 974–987, 1969.

Siegesmud, S., T. Takeshita, and H. Kern, Anisotropy of vp and vs in an amphibolite of the deep crust and its relationship to the mineralogical, microstructural and textural characteristics of the rock, *Tectonophysics*, *157*, 25–38, 1989.

Siegesmund, S., and M. Dahms, Fabric-controlled anisotropy of elastic, magnetic and thermal properties of rocks, in *Textures of Geological Materials Deutsche Gesellschaft fr Materialkunde-Informationsgesellschaft-Verlag*, edited by H. J. Bunge, S. Siegesmund, S. Skrotzki, and K. Weber, vol. Oberursel, pp. 353–379, 1994.

Smith, A. G., The tectonic significance of the hellenic-dinaric ophiolites, *Geological Society of London Spec. Pub.*, *76*, 213–243, 1993.

Stacey, F. D., Magnetic anisotropy of igneous rocks, *J. Geophys. Res.*, *65*, 2429–2442, 1960.

Stephenson, A., Distribution anisotropy: two simple models for magnetic lineation and foliation, *Phys. Earth Planet. Inter.*, *82*, 49–54, 1994.

Tarling, D. H., *Palaeomagnetism*, Chapman and Hall, London, 1983.

Tarling, D. H., and F. Hrouda, *The Magnetic Anisotropy of Rocks*, Chapman and Hall, London, 1993.

Thomsen, L., Weak elastic anisotropy, *Geophysics*, *51*, 1954–1966, 1986.

Toft, P. B., J. Arkani-Hamed, and S. E. Haggerty, The effects of serpentinization on density and magnetic susceptibility: a petrophysical model, *Phys. Earth Planet. Inter.*, *65*, 137–157, 1990.

Van Buskirk, W. C., S. C. Cowin, and R. Carter Jr, A theory of acoustic measurement of the elastic constants of a general anisotropic solid, *J. Mater. Sci.*, *21*, 2759–2762, 1986.

Vernik, L., Microcrack-induced versus intrinsic elastic anisotropy in mature hc-source shales, *Geophysics*, *58*, 1703–1706, 1993.

Vernik, L., and A. Nur, Ultrasonic velocity and anisotropy of hydrocarbon source rocks, *Geophysics*, *57*, 727–735, 1992.

Vestrum, R. W., *Group and phase-velocity inversions for the general anisotropic stiffness tensor*, M. Sc. thesis, University of Calgary, 1994.

Weiss, T., S. Siegesmund, and T. Bohlen, Seismic, structural, and petrological models of the subcrustal lithosphere in southern germany: A quantitative revaluuation, *Pure and applied geophysics*, *156*, 53–81, 1999.

White, R., D. McKenzie, and K. O'Nions, Oceanic crustal thickness from seismic measurements and rare earth element inversions, *Journal of Geophysical Research*, *97 (B13)*, 19,683–19,715, 1992.

Winterstein, D. F., Velocity anisotropy terminology for geophysicists, *Geophysics*, *55*, 1070–1088, 1990.

Yaouancq, G., and C. J. Macleod, Petrofabric investigation of gabbros from the oman ophiolite: Comparsion between ams and rock fabric, *Marine Geophysical Researchs*, *21*, 289–305, 2000.

Yin, H., *Acoustic velocity and attenuation of rocks: isotropy, intrinsic anisotropy, and stress induced anisotropy*, Ph.D. thesis, Stanford University, 1992.

Appendix A

Thin section

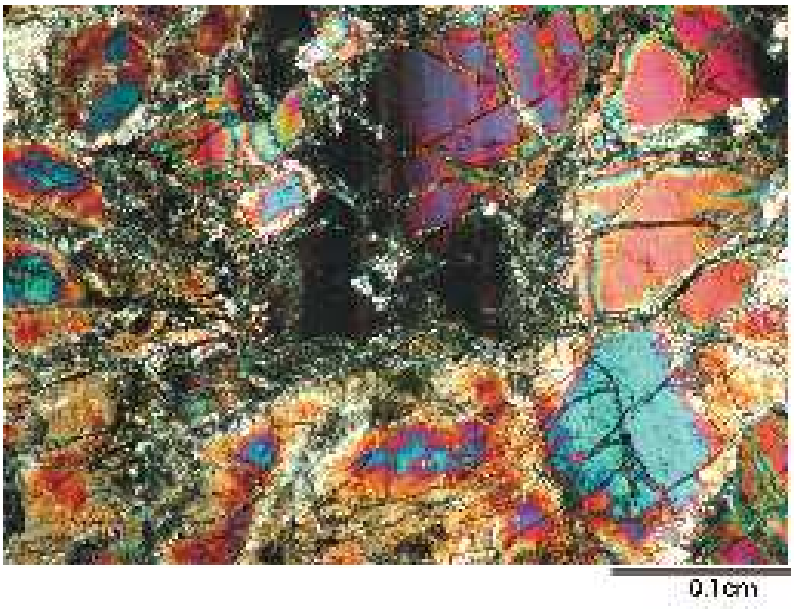

(a)

(b)

Figure A.1: Thin section of sample P 03-1; Top: Parallel to the foliation ($\times$50). Bottom: Normal to the foliation ($\times$50).

(a)

(b)

Figure A.2: Thin section of sample P 04-2; Top: Parallel to the foliation (×50). Bottom: Normal to the foliation (×50).

(a)

(b)

Figure A.3: Thin section of sample P 08-3; Top: Parallel to the foliation (×50). Bottom: Normal to the foliation (×50).

Figure A.4: Thin section of sample P 08-4 (×50).

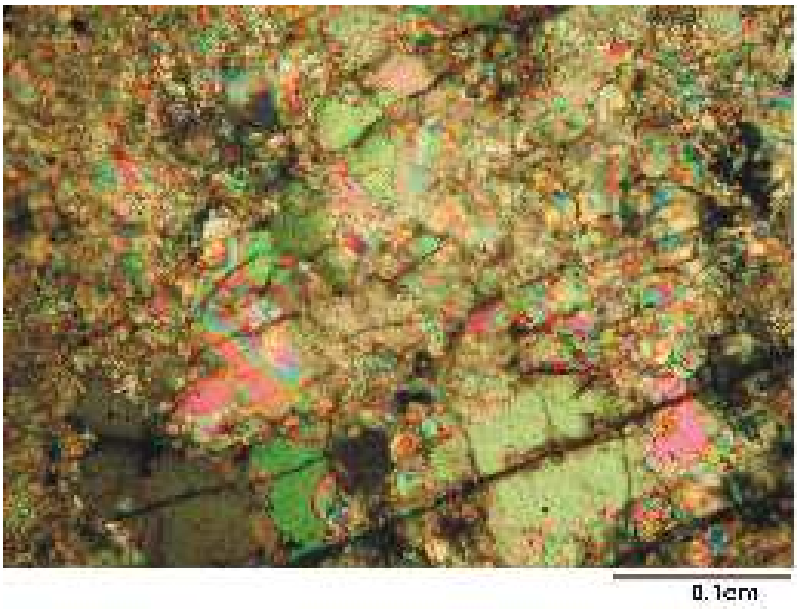

(a)

(b)

Figure A.5: Thin section of sample P 11-1; Top: Parallel to the foliation (×50). Bottom: Normal to the foliation (×50).

(a)

(b)

Figure A.6: Thin section of sample P 12-1; Top: Parallel to the foliation (×50). Bottom: Normal to the foliation (×50).

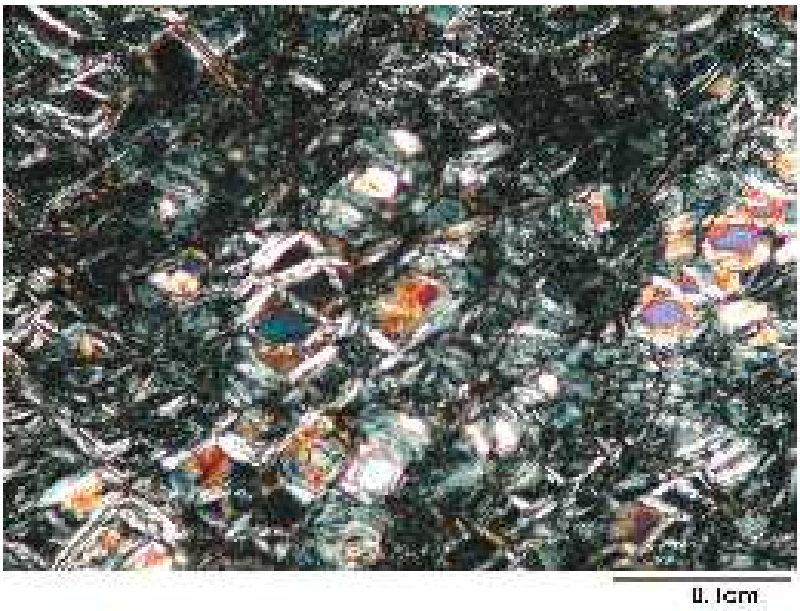

(a)

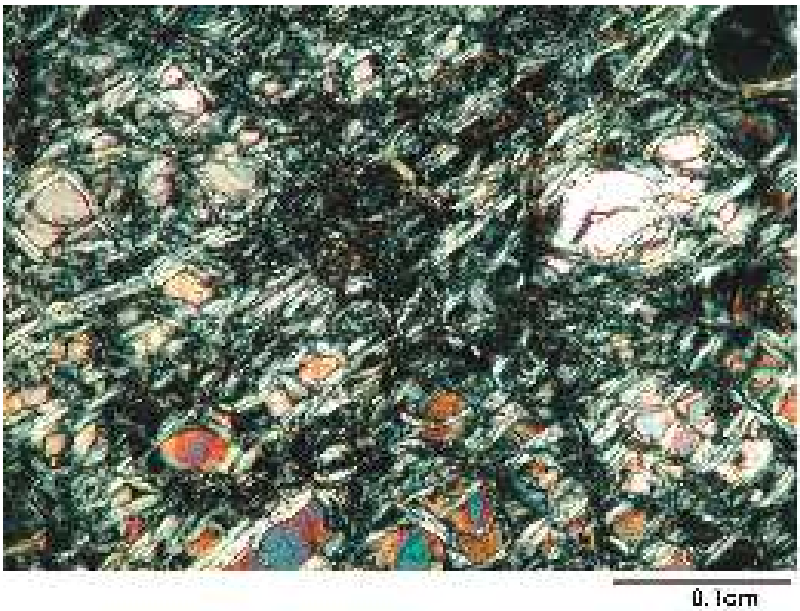

(b)

Figure A.7: Thin section of sample P 13-1; Top: Parallel to the foliation ($\times$50). Bottom: Normal to the foliation ($\times$50).

(a)

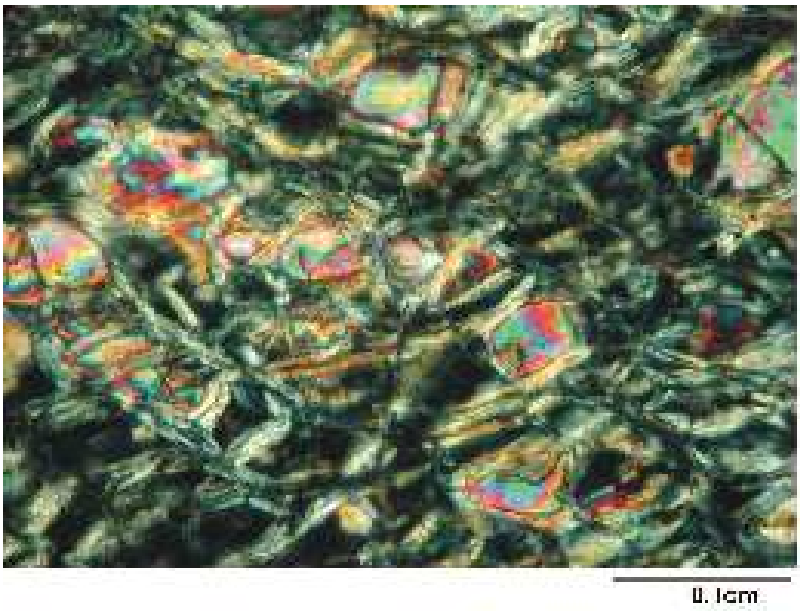

(b)

Figure A.8: Thin section of sample P 13-2; Top: Parallel to the foliation (×50). Bottom: Normal to the foliation (×50).

(a)

(b)

Figure A.9: Thin section of sample P 16-3; Top: Parallel to the foliation (×50). Bottom: Normal to the foliation (×50).

Figure A.10: Thin section of sample V 03-11 ($\times$50).

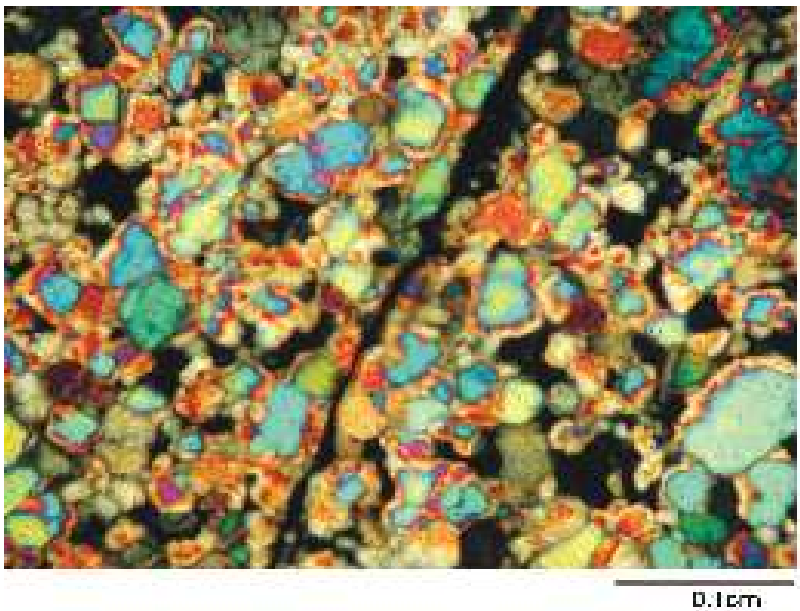

Figure A.11: Thin section of sample V 03-7 ($\times$50).

Appendix B

Velocity Data

Table B.1: P- and S- wave velocities at various confining pressure in sample P 03-1

	P 03-1			P 03-1 Sec(2)		
Pressure [MPa]	$Vs90$ [km/s]	Vp [km/s]	Vs [km/s]	$Vs90$ [km/s]	Vp [km/s]	Vs [km/s]
0	4.10	6.00	3.65	3.15	6.35	3.27
25	4.18	6.19	3.82	3.44	6.75	3.86
50	4.20	6.27	3.88	3.45	6.83	3.91
75	4.21	6.33	3.91	3.46	6.87	3.93
100	4.22	6.36	3.92	3.47	6.91	3.94
125	4.22	6.39	3.93	3.48	6.94	3.95
150	4.23	6.40	3.94	3.49	6.95	3.96
175	4.23	6.42	3.95	3.49	6.97	3.97
200	4.24	6.43	3.95	3.50	6.97	3.98
225	4.24	6.45	3.96	3.50	6.99	3.98
250	4.24	6.46	3.96	3.51	7.01	3.99
275	4.25	6.47	3.97	3.52	7.01	3.98
300	4.25	6.48	3.97	3.52	7.05	4.00

Table B.2: P- and S- wave velocities at various confining pressure in sample P 04-2

	P 04-2			P 04-2 Sec		
Pressure [MPa]	$Vs90$ [km/s]	Vp [km/s]	Vs [km/s]	$Vs90$ [km/s]	Vp [km/s]	Vs [km/s]
0	3.11	5.13	2.96	2.94	5.91	2.46
25	3.16	5.65	3.04	3.09	5.96	2.86
50	3.17	5.68	3.06	3.11	6.00	2.89
75	3.19	5.70	3.07	3.12	6.04	2.90
100	3.19	5.72	3.08	3.13	6.07	2.91
125	3.20	5.74	3.08	3.14	6.08	2.91
150	3.21	5.77	3.09	3.14	6.11	2.92
175	3.22	5.78	3.09	3.15	6.12	2.92
200	3.23	5.80	3.10	3.15	6.15	2.93
225	3.23	5.81	3.10	3.16	6.16	2.93
250	3.24	5.84	3.10	3.16	6.17	2.94
275	3.25	5.85	3.11	3.17	6.20	2.94
300	3.25	5.87	3.11	3.17	6.21	2.94

Table B.3: P- and S- wave velocities at various confining pressure in sample P 08-3

	P 08-3			P 08-3 Sec		
Pressure [MPa]	$Vs90$ [km/s]	Vp [km/s]	Vs [km/s]	$Vs90$ [km/s]	Vp [km/s]	Vs [km/s]
0	3.45	6.23	3.32	3.19	5.94	3.40
25	3.54	6.30	3.39	3.25	6.08	3.47
50	3.58	6.36	3.41	3.27	6.12	3.49
75	3.59	6.40	3.42	3.29	6.14	3.51
100	3.60	6.44	3.43	3.30	6.17	3.53
125	3.61	6.49	3.44	3.31	6.18	3.53
150	3.62	6.51	3.44	3.32	6.20	3.54
175	3.62	6.52	3.45	3.33	6.21	3.55
200	3.63	6.55	3.46	3.34	6.23	3.56
225	3.64	6.56	3.46	3.34	6.24	3.57
250	3.64	6.57	3.47	3.35	6.27	3.57
275	3.65	6.58	3.48	3.36	6.28	3.58
300	3.66	6.58	3.48	3.38	6.29	3.58

Table B.4: P- and S- wave velocities at various confining pressure in sample P 08-4

	P 08-4		
Pressure [MPa]	$Vs90$ [km/s]	Vp [km/s]	Vs [km/s]
0	3.51	6.25	3.38
25	3.59	6.33	3.43
50	3.61	6.38	3.45
75	3.62	6.41	3.46
100	3.63	6.43	3.47
125	3.64	6.45	3.47
150	3.64	6.46	3.48
175	3.65	6.48	3.49
200	3.66	6.49	3.50
225	3.67	6.51	3.50
250	3.68	6.52	3.51
275	3.68	6.53	3.51
300	3.69	6.54	3.51

Table B.5: P- and S- wave velocities at various confining pressure in sample P 11-1

	P 11-1			P 11-1 Sec		
Pressure [MPa]	$Vs90$ [km/s]	Vp [km/s]	Vs [km/s]	$Vs90$ [km/s]	Vp [km/s]	Vs [km/s]
0	4.15	7.27	4.22	4.16	6.98	4.00
25	4.22	7.34	4.36	4.43	7.39	4.09
50	4.25	7.37	4.39	4.48	7.46	4.11
75	4.27	7.39	4.41	4.51	7.48	4.13
100	4.28	7.39	4.41	4.52	7.50	4.14
125	4.28	7.41	4.42	4.53	7.52	4.14
150	4.28	7.43	4.42	4.54	7.53	4.17
175	4.29	7.44	4.43	4.54	7.55	4.19
200	4.29	7.45	4.43	4.55	7.57	4.20
225	4.29	7.46	4.44	4.55	7.58	4.22
250	4.30	7.47	4.44	4.56	7.58	4.23
275	4.30	7.48	4.44	4.57	7.61	4.23
300	4.30	7.49	4.45	4.57	7.63	4.25

Table B.6: P- and S- wave velocities at various confining pressure in sample P 12-1

	P 12-1			P 12-1 Sec		
Pressure [MPa]	$Vs90$ [km/s]	Vp [km/s]	Vs [km/s]	$Vs90$ [km/s]	Vp [km/s]	Vs [km/s]
0	3.40	6.11	3.56	3.94	6.80	3.96
25	3.81	6.40	3.86	4.11	7.36	4.12
50	3.88	6.47	3.93	4.15	7.41	4.18
75	3.91	6.58	3.96	4.16	7.43	4.20
100	3.93	6.61	3.99	4.17	7.50	4.21
125	3.95	6.61	4.01	4.18	7.53	4.23
150	3.96	6.62	4.02	4.19	7.55	4.23
175	3.97	6.70	4.03	4.20	7.56	4.24
200	3.98	6.78	4.04	4.21	7.57	4.25
225	3.99	6.77	4.07	4.23	7.58	4.25
250	3.99	6.77	4.08	4.24	7.60	4.26
275	4.00	6.77	4.09	4.25	7.61	4.26
300	4.01	6.77	4.10	4.25	7.62	4.27

Table B.7: P- and S- wave velocities at various confining pressure in sample P 13-1

	P 13-1			P 13-1 Sec		
Pressure [MPa]	$Vs90$ [km/s]	Vp [km/s]	Vs [km/s]	$Vs90$ [km/s]	Vp [km/s]	Vs [km/s]
0	2.54	4.85	2.57	2.72	4.93	2.74
25	2.63	5.04	2.67	2.83	5.15	2.80
50	2.65	5.07	2.70	2.84	5.20	2.82
75	2.67	5.13	2.71	2.86	5.23	2.82
100	2.67	5.16	2.72	2.87	5.26	2.83
125	2.68	5.20	2.72	2.87	5.28	2.84
150	2.68	5.23	2.73	2.88	5.31	2.85
175	2.69	5.24	2.74	2.88	5.34	2.86
200	2.69	5.27	2.74	2.89	5.36	2.87
225	2.70	5.28	2.75	2.89	5.38	2.87
250	2.71	5.29	2.75	2.89	5.41	2.88
275	2.71	5.29	2.75	2.90	5.44	2.88
300	2.72	5.29	2.76	2.90	5.45	2.89

Table B.8: P- and S- wave velocities at various confining pressure in sample P 13-2

	P 13-2			P 13-2 Sec		
Pressure [MPa]	$Vs90$ [km/s]	Vp [km/s]	Vs [km/s]	$Vs90$ [km/s]	Vp [km/s]	Vs [km/s]
0	2.69	5.45	2.50	2.72	5.33	2.70
25	2.77	5.53	2.55	2.78	5.48	2.73
50	2.79	5.56	2.58	2.79	5.54	2.74
75	2.80	5.57	2.59	2.80	5.57	2.75
100	2.80	5.58	2.60	2.81	5.60	2.76
125	2.81	5.60	2.60	2.81	5.62	2.76
150	2.81	5.62	2.61	2.82	5.64	2.77
175	2.82	5.63	2.61	2.83	5.66	2.77
200	2.82	5.63	2.62	2.83	5.67	2.77
225	2.82	5.65	2.62	2.84	5.69	2.78
250	2.83	5.65	2.63	2.84	5.70	2.78
275	2.83	5.67	2.63	2.85	5.71	2.78
300	2.83	5.68	2.63	2.85	5.72	2.79

Table B.9: P- and S- wave velocities at various confining pressure in sample P 16-3

	P 16-3			P 16-3 Sec		
Pressure [MPa]	$Vs90$ [km/s]	Vp [km/s]	Vs [km/s]	$Vs90$ [km/s]	Vp [km/s]	Vs [km/s]
0	2.85	5.87	3.04	3.02	5.71	2.92
25	2.95	5.96	3.12	3.08	5.84	2.99
50	2.99	6.00	3.14	3.09	5.91	2.98
75	3.01	6.05	3.15	3.08	5.94	2.99
100	3.02	6.07	3.16	3.09	5.97	3.00
125	3.03	6.10	3.16	3.10	5.99	3.00
150	3.04	6.14	3.17	3.10	6.00	3.01
175	3.04	6.16	3.17	3.11	6.02	3.02
200	3.04	6.17	3.17	3.11	6.03	3.02
225	3.05	6.19	3.18	3.11	6.05	3.02
250	3.05	6.20	3.18	3.11	6.06	3.03
275	3.06	6.22	3.19	3.12	6.07	3.03
300	3.06	6.23	3.19	3.12	6.08	3.04

Table B.10: P- and S- wave velocities at various confining pressure in sample V 03-11

	P 03-11		
Pressure [MPa]	$Vs90$ [km/s]	Vp [km/s]	Vs [km/s]
0	3.21	5.46	3.18
25	3.26	5.52	3.23
50	3.28	5.56	3.25
75	3.29	5.59	3.26
100	3.32	5.62	3.27
125	3.32	5.65	3.27
150	3.33	5.67	3.28
175	3.34	5.70	3.29
200	3.34	5.72	3.30
225	3.35	5.74	3.30
250	3.35	5.75	3.31
275	3.37	5.77	3.32
300	3.38	5.80	3.32

Table B.11: P- and S- wave velocities at various confining pressure in sample V 03-7

P 03-7			
Pressure [MPa]	$Vs90$ [km/s]	Vp [km/s]	Vs [km/s]
0	2.91	5.31	3.08
25	3.00	5.40	3.13
50	3.02	5.43	3.14
75	3.03	5.45	3.16
100	3.03	5.47	3.17
125	3.04	5.49	3.17
150	3.04	5.51	3.19
175	3.04	5.52	3.18
200	3.05	5.54	3.19
225	3.05	5.55	3.19
250	3.06	5.58	3.20
275	3.06	5.60	3.21
300	3.08	5.62	3.21

Appendix C

X-ray diffraction

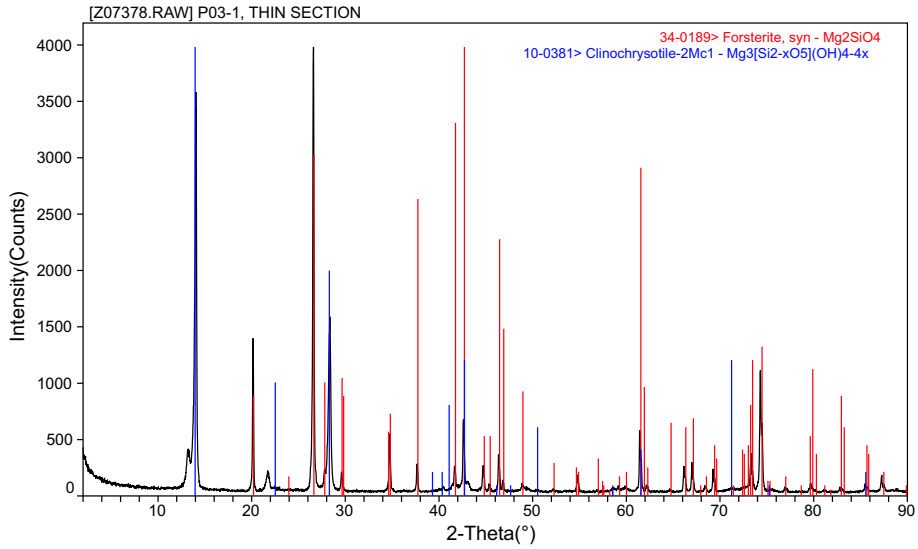

(a)

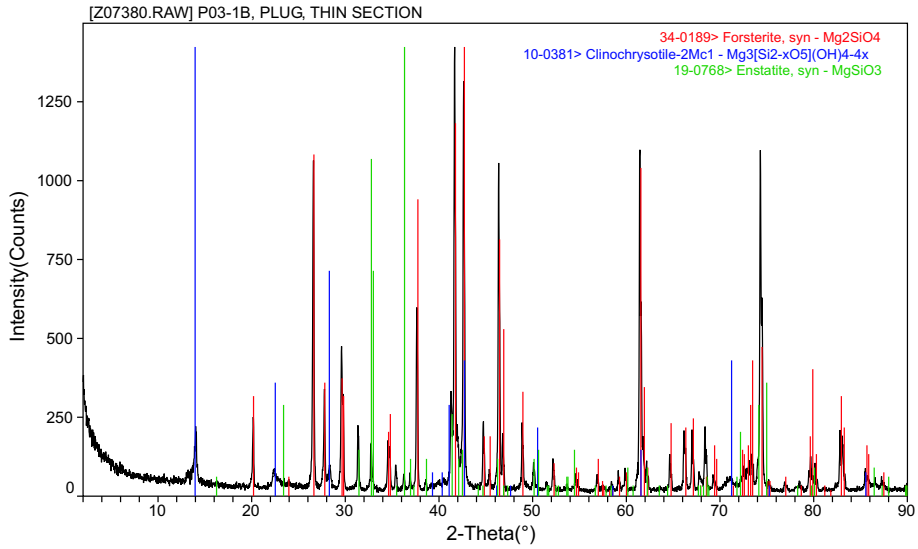

(b)

Figure C.1: X-ray diffraction from different orientations in sample P 03-1; Top: Parallel to the foliation. Bottom: Normal to the foliation.

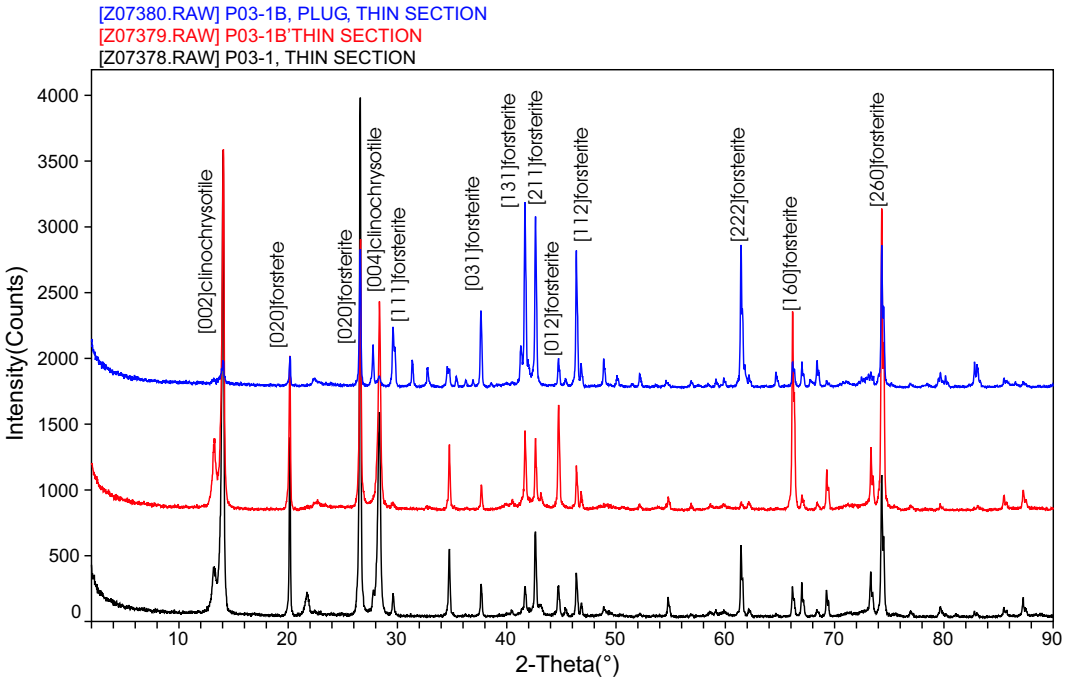

Figure C.2: Comparison by different orientations of P 03-1 X-ray diffraction.

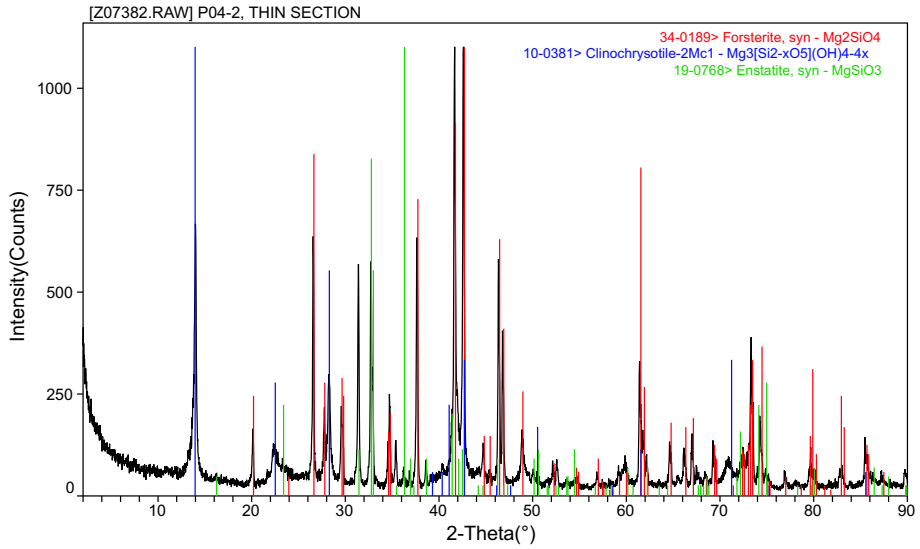

(a)

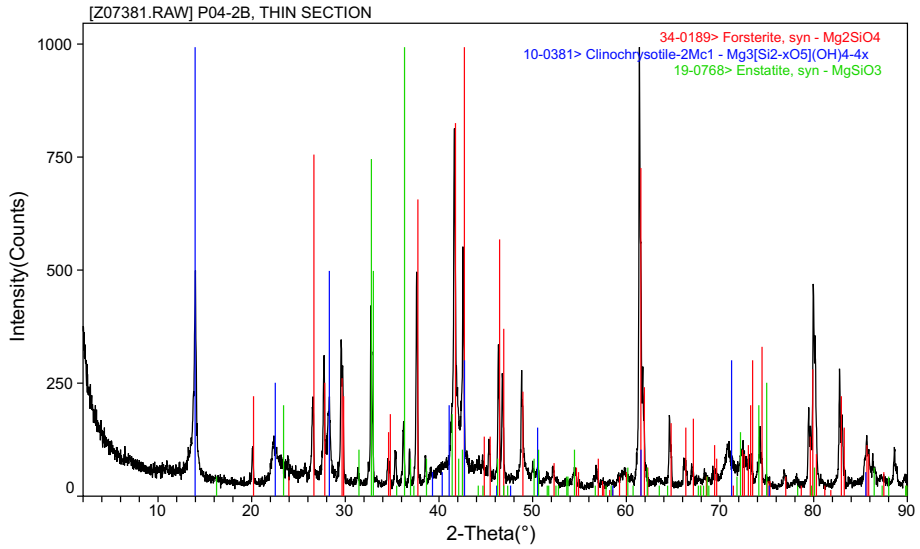

(b)

Figure C.3: X-ray diffraction from different orientations in sample P 04-2; Top: Parallel to the foliation. Bottom: Normal to the foliation.

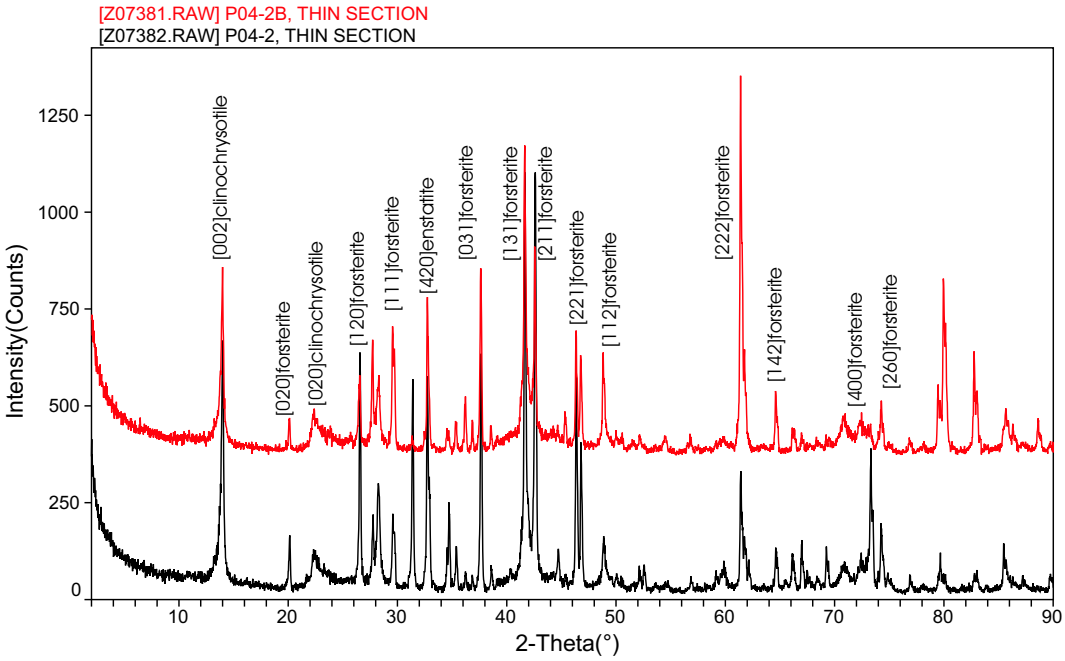

Figure C.4: Comparison by different orientations of P 04-2 X-ray diffraction.

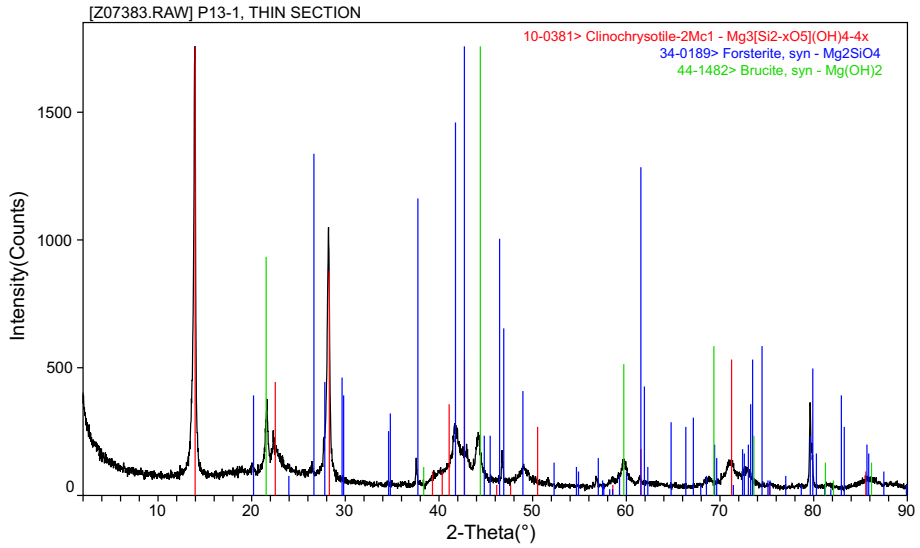

(a)

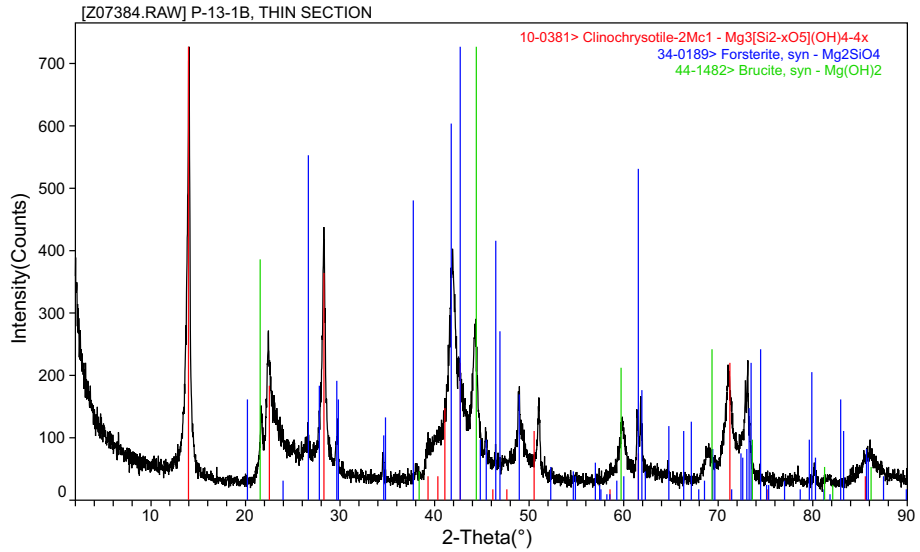

(b)

Figure C.5: X-ray diffraction from different orientations in sample P 13-1; Top: Parallel to the foliation. Bottom: Normal to the foliation.

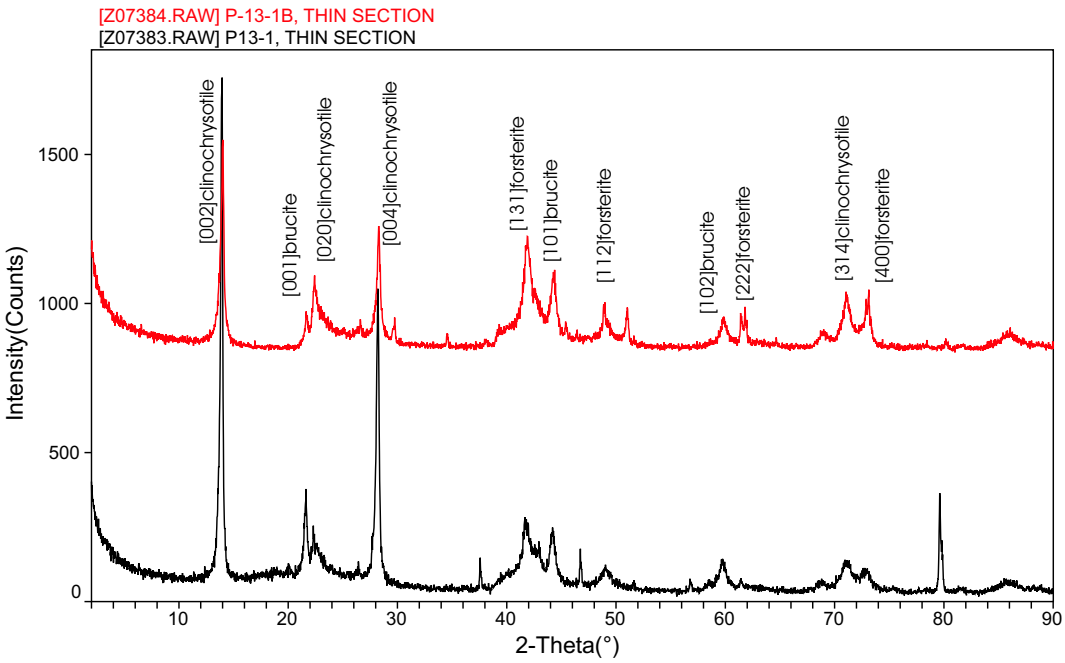

Figure C.6: Comparison by different orientations of P 13-1 X-ray diffraction.

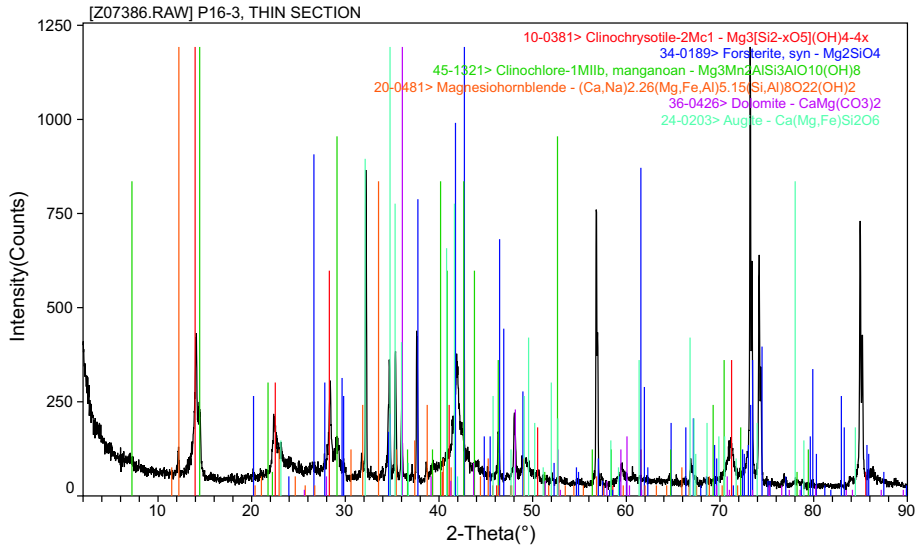

(a)

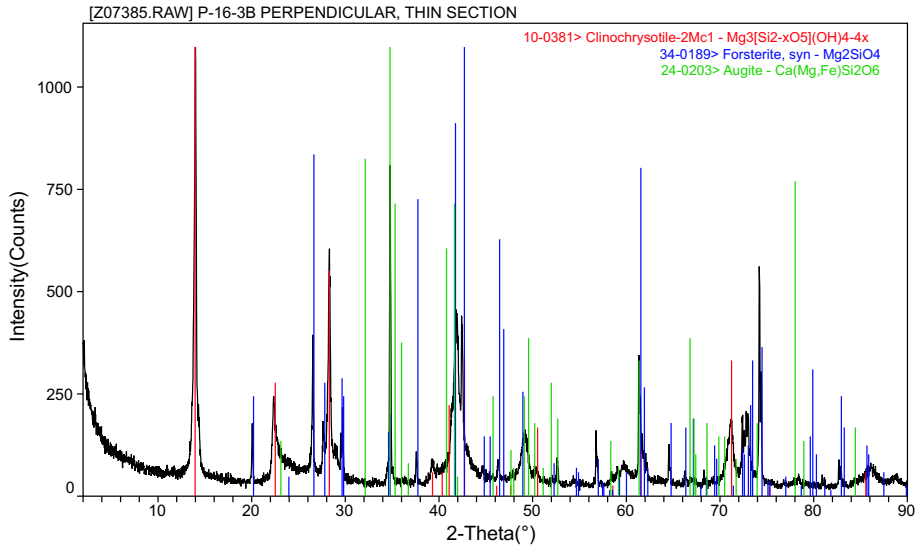

(b)

Figure C.7: X-ray diffraction from different orientations in sample P 16-3; Top: Parallel to the foliation. Bottom: Normal to the foliation.

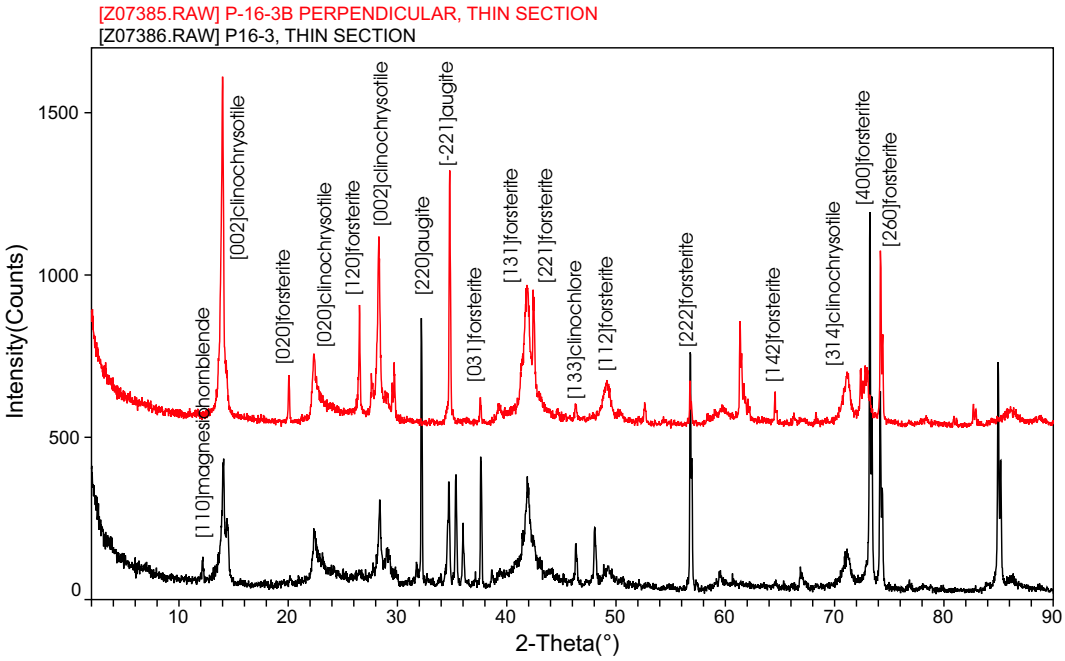

Figure C.8: Comparison by different orientations of P 16-3 X-ray diffraction.